MONASH University

Functional Nano-Metallic Electrodes for Applications in Electrocatalysis and Flexible Electronics

A thesis submitted for the degree of
Doctor of Philosophy

By

Yue Tang

Department of Chemical Engineering
Monash University
Australia

January 2014

ADDENDUM

1. p 99: add a new Table as Table 4.4, and the corresponding comments: Moreover, as shown in Table 4.4, the peak current densities normalized by EASA of AuNP-modified electrodes were higher than the ones of BGE, indicating better electrocatalytic performances towards both ORR and MOR.

Table 4.4 Current density of AuNP modified ITO electrodes and BGE towards MOR and ORR

	Peak Current Density ($mA \cdot cm^{-2}$) towards MOR	**Peak Current Density ($mA \cdot cm^{-2}$) towards ORR**
Au nanospheres (d = 20 nm)	5.63	-0.60
Au nanospheres (d = 45 nm)	3.52	-0.53
Au nanorods ($20 \times 20 \times 60\ nm^3$)	1.28	-0.41
BGE	0.04	-0.01

2. p 117: Add at the end of para 1:

"Meanwhile, we also calculated the porosity of the CuNW aerogel monoliths from their densities, the results indicated that the aerogels are highly porous, within the porosity ranging from 98.25% to 99.91%."

Declaration

I, Yue Tang, declare that this thesis contains no material which has been accepted for the award of any other degree or diploma in any university or equivalent institution, and that, to the best of my knowledge and belief, this thesis contains no material previously published or written by another person, except where due reference is made in the text of the thesis.

Yue Tang

15th, Jan. 2014

Acknowledgement

I would like to acknowledge the people in my life that contribute significantly towards me accomplishing my PhD. First of all I would like to thank my supervisor Associate Professor Wenlong Cheng for giving me the opportunity to work on this project and all the help and guidance. I would like to thank Khee Chaw Ng for teaching me the basics of the project, training me on optical characterizations, and helping me with my experiments. I want to thank Yi Chen for his help with my experiments and the corrections of some chapters of my thesis. Also thanks to all of my group members for various supports on my experiments.

I would like to thank Mr. Ling Qiu from the Department of Materials Engineering for his help with mechanical and electrical property characterizations of my samples. I would like to thank Dr. Kun Wang for her help with Fourier transform infrared spectroscopy experiments. Also thanks to Dr. Bin Su at Chinese Academy of Sciences for the measurements of contact angle and the corrections of some of my publications.

I would also like to thank Monash University for providing me a Monash Research Graduate Scholarship and an International Postgraduate Research Scholarship. Thanks to the Australia Research Council (ARC), for funding this project (DP120100170). The Melbourne Centre for Nanofabrication and Monash Center for Electron Microscopy is also acknowledged for the use of their facilities and the provision of scientific and technical assistance.

Last but not least I would like to my parents and friends for simply being the way you are. You are my favourite people in the world and my life without you makes no sense.

Abbreviations and Acronyms

1D, 2D, 3D	one-, two-, three-dimensional
AA	ascorbic acid
AFM	atomic force microscopy
AgNW(s)	silver nanowire(s)
APTMS	(3-aminopropyl)trimethoxysilane
AuNP(s)	gold nanoparticle(s)
AuNR(s)	gold nanorod(s)
AuNS(s)	gold nanosphere(s)
BGE	bare gold electrode
CNT(s)	carbon nanotubes
CPC	cetylpyridinium chloride
CTAB	cetyltrimethylammonium bromide
CuNW(s)	copper nanowire(s)
DNA	deoxyribonucleic acid
EDA	ethylenediamine
GCE	glassy carbon electrode
GR	guaranteed reagent
HDA	hexadecylamine
ITO	indium tin oxide
LBL	layer by layer
MOR	methanol oxidation reduction
MS	mercaptopropyltrimethoxysilane
NIR	near infrared
NP(s)	nanoparticle(s)
ORR	oxygen reduction reaction
PAH	poly(allylaminehydrochloride)
PDMS	poly(dimethylsiloxane)
PE	polyelectrolyte
PEI	poly(ethylenecimine)
PET	poly(ethylene terephthalate)
PS	polystyrene
PSS	poly(styrene sulfonate sodium salt)
Pt/C	fine particles of Pt supported on porous carbon materials
PtNP(s)	platinum nanoparticle(s)
PU	polyurethane
PVA	poly(vinyl alcohol)
PVP	polyvinylpyrrolidone
RF	resorcinol-formaldehyde

SD	standard deviation
SEM	scanning electron microscopy
SPEs	screen-printed electrodes
TEM	transmission electron microscopy
UV-O_3	UV-O_3 Ultraviolet-Ozone
UV-vis	ultraviolet-visible
VAF	vacuum-assisted flocculation
CV	cyclic voltammogram
PBS	phosphate buffered saline
EASA	electrochemically active surface aera

Abstract

The thesis focuses on low-cost bottom-up approach to design nanostructured electrode materials for novel applications in electrocatalysis and stretchable electronics. In particular, the work presented in this thesis were about (1) the fabrication of functional nanostructured electrodes with synthetic meta-atoms from the "artificial periodic tables" (Figure 1.3) using cost-effective "bottom-up" approach; (2) the size- and shape-dependent electrocatalytic properties of the as-fabricated electrodes; and (3) the applications of the as-fabricated electrodes in lightweight and stretchable electronics. The key novel features are summarized as follows:

A robust chemical-tethering approach was developed to immobilize AuNPs onto transparent indium tin oxide (ITO) glass electrode surface, and their size- and shape-dependent electrocatalysis towards methanol oxidation reaction (MOR) and oxygen reduction reaction (ORR) was systematically investigated. In particular, mono-dispersed 20 nm nanospheres (AuNS20s), 45 nm nanospheres (AuNS45s) and $20 \times 20 \times 63$ nm^3 nanorods (AuNRs) were synthesized and chemically tethered to ITO surface forming submonolayers without any aggregation. These nanoparticle-modified ITO electrodes exhibited strong electrocatalytic activities towards MOR and ORR but their mass activities were highly dependent on particle sizes and shapes. For particle with similar shapes, size determined the mass activities: smaller particle size led to greater catalytic current density per unit mass due its greater surface-to-volume ratio (AuNS20s > AuNS45s). For particles with comparable sizes, shapes or crystalline structures governed selectivity of electrocatalytic reactions: AuNS45 exhibited a higher mass current density in MOR than that for AuNRs due to its dominant (111) facets exposed; whereas AuNRs exhibited a higher mass current density in ORR due to its dominant (100) facets exposed.

A low-cost and simple yet efficient drop-casting method was developed to fabricate lightweight and mechanically flexible electrocatalytic electrodes from AuNRs and AuNS45s. Low cost, flexible, and highly porous tissue paper sheets were chosen as the substrates; AuNPs were packed closely on the surface, therefore the electrodes were highly conductive without any requirement of conductive substrates. Moreover, owing

to the hierarchical porous structure of paper fibers and the high volume-to-surface ratio of AuNPs, the modified electrode exhibited extremely large electrochemical active surface area (EASA). In comparison with conventional gold disk electrodes, the electrocatalytic activities of AuNP electrodes towards ORR and MOR were greatly improved. Furthermore, AuNP electrode are highly stable; AuNPs kept their well-defined shapes after 1000 cycles scanning in 0.1 M PBS (pH=7.2) or 500 cycles scanning in 0.1 M KOH with 3 M methanol. In addition, the universality of this approach was proved by extending the substrate to commercial available sponges.

The ultra-lightweight copper aerogel monoliths were synthesized from copper nanowires (CuNWs) for the first time through an environmentally friendly freeze-drying approach. Their mechanical and electrical properties were finely tunable simply by varying the densities of the aerogels. However, the poor mechanical strength of the aerogels limited their applications in flexible electronics. A trace amount of additive – polyvinyl alcohol (PVA) was found to substantially improve the mechanical strength of CuNWs aerogel monoliths while maintaining high conductivity (~ 0.83 $S \bullet cm^{-1}$) and ultra-low density (~10 $mg \bullet cm^{-3}$). The CuNW-PVA composite aerogels exhibited high durability at cyclic loads, enabling their applications as the elastic piezo-resistivity switch. More importantly, the CuNW-PVA aerogels could be embedded into PDMS matrix, leading to electrically conductive rubber ambers without the need of pre-wiring. The rubber ambers could be further manufactured into various one-dimensional (1D), 2D and 3D objects that were all conductive after shaping. We believe that our fabrication strategy represents a new low-cost route to manufacture under mild conditions flexible conductors with versatile shapes for versatile applications in flexible electronics.

Table of Contents

This page is intentionally blank

Chapter One

Introduction

Nanostructured materials with well-defined sizes and shapes play a critical role in recent development of nanotechnologies, especially in energy-related applications.[37] Owing to their high surface to volume ratio and tunable physical properties, metallic nanomaterials have been regarded as promising building blocks for functional electrodes. Over the past decades, research on the design of nano-metallic electrodes has been dramatically intensified mainly owing to two factors. On one hand, continuous progresses have been achieved on the synthesis of nano-sized metals with various morphologies;[38] on the other hand, development of nanotechnology has offered ample methods for the fabrication of nanomaterial-based electrodes.[39]

Currently, most efforts focus on constructing functional electrodes with minimum cost and optimum performance.[40] The investigations on shape/size dependent electrocatalytic performance of metallic nanomaterials allow researchers to achieve the highest efficiency via tailoring the structures of nanometals.[41] Moreover, motivated by natural materials, porous metallic aerogels have been produced with reduced metal utilization and been developed as conductive electrodes.[42] In addition, more economical and practical techniques, such as bottom-up assembly, are employed to fabricate nano-metallic electrodes.

The introduction includes the following contexts; (1) summary of conventional techniques for metallic electrode fabrication, (2) history of synthesizing metallic nanostructures, especially nano-sized gold and nanowire-like copper, (3) development on design and shape/size dependent electrocatalysis of nano-metallic electrodes, (4)

review of fabrication methods for metallic aerogels and their applications, and (5) the aim of this thesis.

1.1 Conventional Techniques for Metallic Electrode Fabrication

The word “electrode”, coined by the scientist Michael Faraday in the year of 1894, was originally used to describe a current conductor connecting non-conductive parts in a circuit. However, during the past century, the utilizations of electrodes have been significantly expanded into various fields, including energy transfer and storage,[37] sensors,[43] and therapeutic applications,[44] owing to the development of fabrication approaches. By far, customized metallic electrodes are generally produced via four main methodologies: polishing, annealing, coating, and printing.

1.1.1 Polishing

For every electrochemical application, clean and highly active electrode surface is a prerequisite. Therefore, precise and specific surface pretreatment procedures are indispensable before carrying out electrochemical reactions.[45] The most commonly applied technique is polishing, which are further divided into three major catalogs; manual, chemical, and electrochemical polishing. The manual polishing procedure consists of mechanically polishing the metallic electrode to get a mirror-like surface with alumina slurry and nylon/diamond pads. After polishing, the electrode is rinsed copiously to remove residual alumina particles.[45] In comparison with manual procedures, chemical polishing requires less labor efforts; to reduce the oxidative organic contaminants, electrodes are normally immersed in ethanol or acidic aqueous solutions.[46] To obtain a low current background as well as rapid electron transfer rates, electrochemical polishing is always carried out following the manual or chemical steps.[47] Generally, electrodes are cleaned by potential cycling in specific electrolyte solutions, resulting in a smoother surface.

1.1.2 Annealing

Metallic electrodes with single crystal surface have received extensive attentions, since they can provide accurate information of the correlation between interfacial structures and electrochemical activity. Preparation of metallic single crystal electrodes was stimulated by Clavilier et al.; in the year of 1980, they introduced flame annealing technique for preparing high-quality single crystal platinum electrodes.[48] Briefly, platinum wire is heated in the flame of a torch (hydrogen-oxygen) to melt (~1000 ℃) and then cooled with ultrapure water. Until 1987, flame annealing technique had been successfully applied to various metals, such as gold, silver, and rhodium.[49, 50] Vacuum annealing is also a commonly used technique for preparing single crystal electrodes.[51] Moreover, electrochemical characterizations are directly performed in an ultra-high vacuum chamber after electrode fabrication, which protected them from contaminations caused by *transfer*, contributing a better perception of structure-dependent electrochemical process. However, the applications of flaming and vacuum annealing techniques are mainly limited to novel metals. In the year of 2005, Voigtländer et al. extended the fabrication of single crystal electrodes into various metals, including copper, molybdenum, silver, palladium, and etc., by using a novel technique named electron beam annealing.[52] Usually, an electron beam generated by the heating of tungsten fuse is employed to accelerate the end of a metal wire, until the formation of a liquid bead. The solidification of the electrode surface is realized by reducing the power of the electron beam.[53] Nowadays, owing to the high local heating speed and convenient computer controlling, electron beam technique becomes an excellent tool in various applications, including welding, surface treatment, vapor deposition, and lithography.

1.1.3 Coating

The desire for energy utilizations as well as potable electronic devices spurs the research on the fabrication of two-dimensional (2D) electrodes. For instance, owing to the low processing budget and simple procedures, polymer solar cells are regarded as

unrivalled technique to resolve energy crisis.[4] However, the increasing demand for raw materials, especially indium, is the main challenging on the development of solar cells. Currently, scientists start to use carbon or metallic materials as the alternatives for film electrodes.[54] Accordingly, film-forming techniques, such as coating and printing, are developed or improved for the generation of highly efficient electrodes.

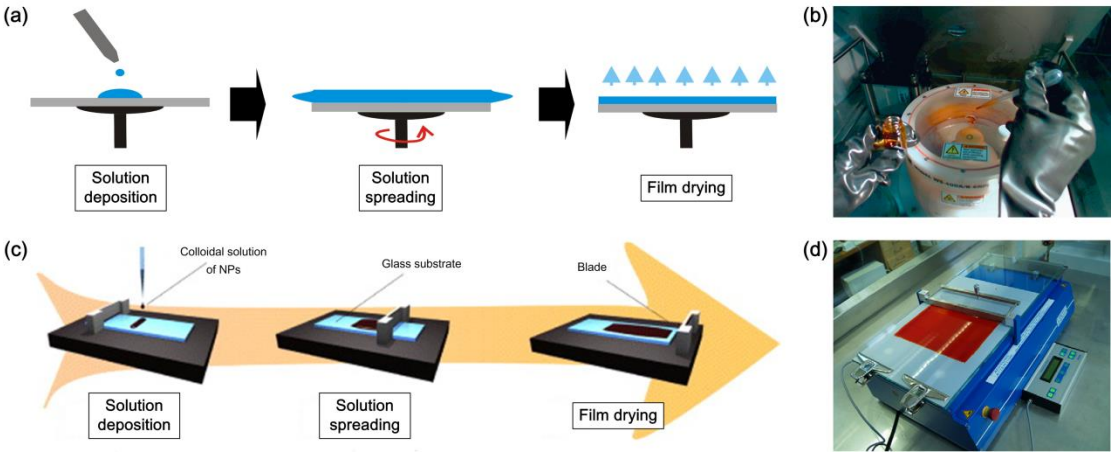

Figure 1.1 Coating processing for the fabrication of 2D electrodes. (a) Schematic illustration and (b) a photograph of typical spin coating operation in a glove box. (c) Schematic illustration and (d) a photograph of typical doctor blading operation. (© 2008 Elsevier B. V.)[4]

1.1.3.1. Spin Coating

Spin coating has been regarded as the most important technique for film-forming, since the operation processing is highly reproducible and the film formation is very homogenous. Typical spin coating operation involves three steps (Figure 1.1 (a)); firstly, a droplet of liquid is casted on the substrate, secondly, the substrate is accelerated under a chosen rotational speed, and finally, most of the liquid droplet is ejected under the rotation, leaving a thin film on the substrate. The thickness, morphology, and surface topography of the film are dependent on the rotational speed, viscosity of the liquid droplet, and diffusivity of the solutes. With the help of spin coating technique, gold film electrodes for analysis of mercury (II) is fabrication in the year of 1995.[55] Moreover, by associating thermal decomposition process with spin coating, patterned gold electrode was obtained in 2006.[56] Furthermore, based on layer-

by-layer spin coating, Schlicke et al. produced freestanding films of crosslinked gold particles in the year of 2011.[57] However, the applicability for the high volume production of spin coating is challenging, which still expects technical solutions.

1.1.3.2. Doctor Blading

Doctor blading is another promising technique for fabricating 2D electrodes with well-defined thickness. In comparison with spin coating, doctor blading technique allows researchers to produce larger film electrodes with less solution loss (down to ~5%). Generally, the technique works by placing a sharp blade at a fixed distance (typically 10 to 500 μm) from the substrate. (Figure 1.1 (d)) The operation is illustrated in Figure 1.1 (c). In the first step, the coating solution is placed in front of the blade. In the second step, the blade is moved linearly, producing a thin wet film after it. In the third step, the wet film is dried by evaporation under room temperature or proper heating. Similar to the processing of spin coating, the thickness of the wet film is decided by the concentration and viscosity of the solution; meanwhile, the final dry thickness also depends on surface tension of the coating liquid. By far, doctor blading technique has been successfully applied in the fabrication of electronics[58] and the assembly of metallic nanocrystal superlattices.[59] However, the slow speed of solvent evaporation brings in more influential factors on the thickness and surface topography of the film, which greatly reduces the repeatability of doctor blading technique.

1.1.4 Printing

Different from coating techniques, which transfers ink solution mainly by pouring, casting, and spraying; printing refers to a process by which a layer of ink solution is transferred from a stamp to a substrate by a reversing action.[4] Compared with coating techniques, recently developed printing methods, such as screen printing and ink jet printing, is more suitable for high-volume production.

1.1.4.1. Screen Printing

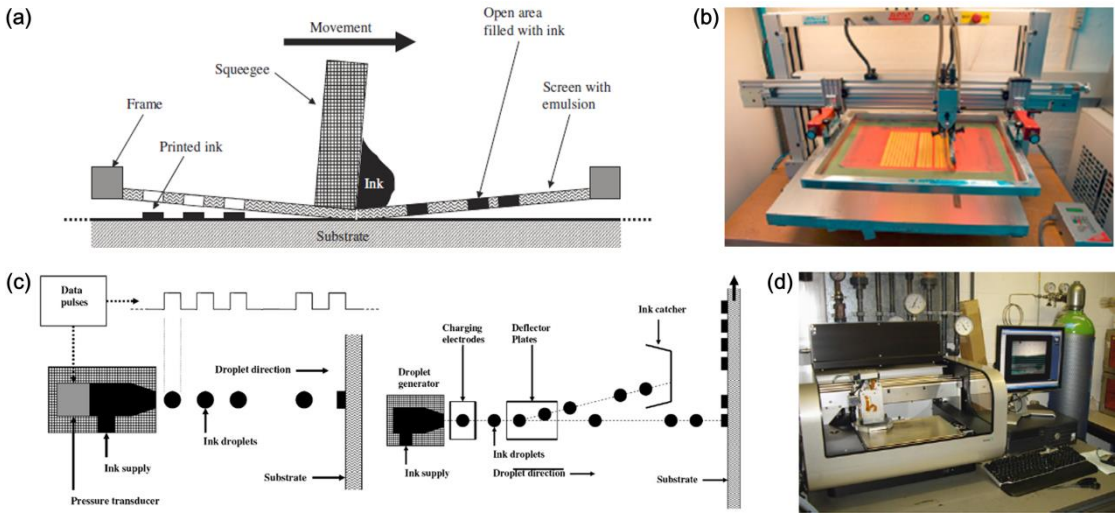

Figure 1.2 Printing processing for the fabrication of 2D electrodes. (a) Schematic illustration of screen printing process and (b) a photograph of a laboratory screen printer. (c) Schematic illustration of ink jet process and (d) a photograph of a laboratory ink jet printer. (© 2008 Elsevier B. V.)[4]

At the beginning of 20th century, screen printing became a versatile technique for the fabrication of 2D patterned films.[4] In comparison with the coating processing, there is almost no loss of ink solution during printing. The process of screen printing is illustrated in Figure 1.2 (a). According to the final pattern, a screen is designed, on which the open area will be filled with ink solution and the rest is impervious to the ink solution. After immersed in the ink, the screen is then brought into proximity of the substrate. By drawing a squeegee linearly across the screen, ink solution is pushed onto the substrate through the open aera. Currently, owing to the disposability, simplicity, and sensitivity, screen-printed electrodes (SPEs) act as the most appreciate electrochemical sensors for in situ analysis.[60] For instance, although with a higher cost, SPEs with gold paste have still received extensive attentions, since the strong Au-S bonds can generate interesting self-assembled monolayers.[61] By immobilizing a thiolated 25 base single stranded probe onto disposable screen-printed gold electrodes, Loaiza et al. fabricated DNA sensors.[62] Moreover, enzyme biosensors were also

produced by electrodepositing poly(3,4-ethylenedioxythiophene) onto a screen-printed gold electrode.

1.1.4.2. Ink jet Printing

In comparison with other fabrication techniques, ink jet printing is a relatively novel process, which is inspired by the typical low-cost ink jet printer for office.[4] The technique has the following advantages; first, the ceramic printing head, which is resistant to most organic solvent, allows ink formula with a wide range; second, ink jet print can produce patterns with high resolution, from 300 dpi to 1,200 dpi; and third, pattern design can be simply completed through computer, without the requirement of complex master. Figure 1.2 (c) shows the process of ink jet printing; a droplet of ink formula is mechanically compressed through a nozzle, and then it is accelerated towards the substrate by an electric field. By far, the manufactory of low-cost and large-area electronics via ink jet printing has been achieved from various metals, including gold, copper, and silver.[63, 64] Gamerith et al. fabricated silver and copper based electrode for organic field-effect transistor application; with thermal curing procedures between 125 ℃ to 400 ℃, the conductivity of the ink jet printed metallic electrodes were increased to the value of bulk metals.[65] However, ink jet printing always prefers electrostatically charged liquids with low viscosity, which slightly restricts the applications of this technique for high volume fabrication of electronics.

1.2 Synthesis of Metallic Nanoparticles

"Bottom-up" design is regarded as a promising approach to overcome the limitations of conventional electrode fabrication approaches, and high-yield production of metallic nanoparticles (NPs) with tailored shape and size is a critical prerequisite for bottom-up design. Generally, high-quality nano-sized metals with controllable morphology and tunable size are achieved through wet chemical synthesis techniques, in which the reaction conditions are deliberately designed to optimize the rational control of particle

growth. Due to continued progress in the synthesis of NPs with controlled morphologies over the last decades, structures such as nanorods, nanowires, nanoprisms, nanostars, etc. from a wide variety of materials have become common in scientific reviews.[38, 66] Representative progress in the synthesis of metallic NPs in terms of shape and dimensionality is highlighted in Figure 1.3.[12]

1.2.1 Gold Nanoparticles (AuNPs)

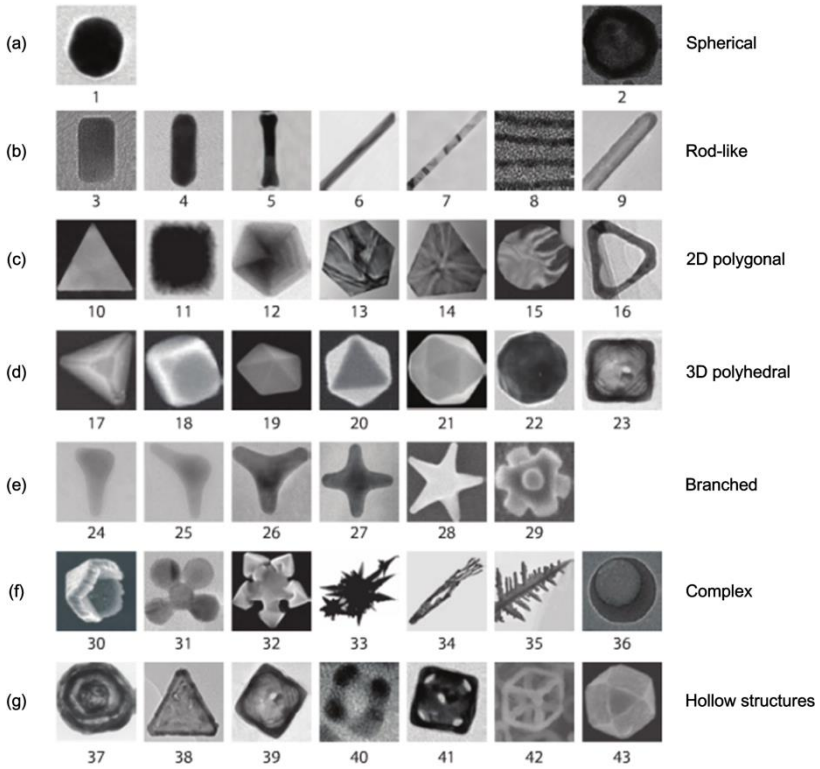

Figure 1.3 Wet-chemically synthesized metal nanostructures: a) spherical shapes (1-solid and 2-hollow nanospheres); b) rod-like shapes (3-nanobar, 4-nanorod, 5-nanobone, 6-nanobeam, 7-nanobelt, 8-nanowires and 9-hollow nanorod); c) 2D polygons (10-triangle, 11-square, 12-pentagon, 13-hexagon, 14-truncated triangle, 15-disc and 16-nanoring); d) 3D polyhedrons (17-tetrahedron, 18-cube, 19-decahedron, 20-octahedron, 21-icosahedron, 22-rhombicuboctahedron and 23-hollow nanocage); e) branched shapes (24-monopod, 25-bipod, 26-tripod, 27-tetrapod, 28-star-shaped and 29-octapod); f) NPs of various complexities (30-nanopyramid, 31-nanoclover, 32-nanosnowflake, 33-nanothorn, 34-nanotree, 35-dendrite and 36-nanocrescent); g) hollow polygonal and polyhedral NPs (37-spherical nanoshell, 38-porous triangles, 39-cubic nanoshell, 40-truncated octahedron, 41-nanocage, 42-nanoskeleton and 43-nanobox). (© 2011Nature Publishing Group)[12] See the original papers for scale bars and other information.

Although empirical methods for the synthesis of spherical gold colloids date back to the Roman empire and early Chinese dynasties,[67, 68] it is only in the past decades that significant progress has been achieved towards non-spherical nanostructures.[69] Indeed it is important to recognize that the synthesis of most shape controlled AuNPs relies on seed-mediated growth, which is normally a two-step process. In the first step, small seed particles of gold with the diameter between 1 and 5 nm are generated under conditions of high chemical supersaturating, which benefit rapid growth of all crystalline surface but contradict shape control. In the second step, with an altered reaction condition where a different reductant and more gold precursors are added, the seeds are grown into larger particles with specified morphologies. In this subsection, developments on the preparation of gold nanospheres, nanorods, nanoprisms, nanocubes, nanospikes, and nanocages via seed-mediated growth are briefly summarized (Figure 1.4).

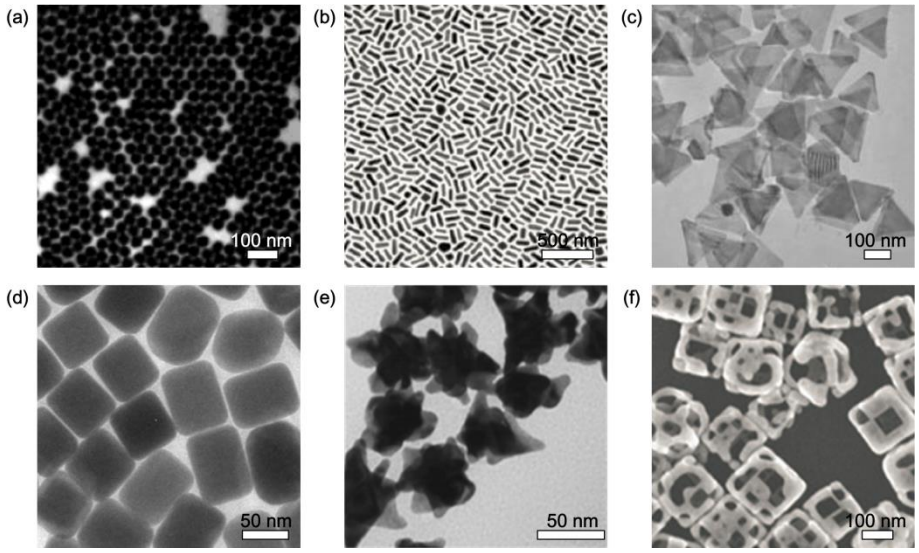

Figure 1.4 AuNPs synthesized seed-mediated growth. (a) AuNSs (© 2001 American Chemical Society),[1] (b) AuNRs (© 2011 American Chemical Society),[15] (c) gold nanoprisms (© 2006 WILEY-VCH Verlag GmbH & Co. KGaA),[25] (d) gold nanocubes (© 2009 American Chemical Society),[31] (e) gold nanospikes (© 2008 IOP Publishing Ltd),[34] and (f) gold nanocages (© 2004 American Chemical Society).[36]

1.2.1.1. Gold Nanospheres (AuNSs) with Adjustable Sizes

Gold spheres with the diameter between 1 nm and 20 nm have been reported in extensive scientific literatures; however, seldom method could produce nanostructures with a uniform size.[1] Generally, strong capping action of thiols, such as disulfides,[70] polymers with mercapto and cyano functional groups,[71] and dendrimers,[72] is recognized to be effective in producing small gold clusters (1-5 nm) with good monodispersity. However, any attempt to generate gold particles larger than 5 nm within one step leads to a wider size distribution (standard deviation (SD), ~25-100%).[73] Therefore, seed-mediated growth is regarded as a wise strategy to produce larger AuNPs (>5 nm) within uniform size, since it can precisely control the process of nucleation and growth. In the year of 2001, Jana et al. reported the synthesis of AuNSs within the size range from 5 nm to 40 nm with a narrow size distribution (SD, ~10-15%) by using 3.5 nm gold particles as seeds (Figure 1.4 (a)).[1] The authors claimed that step by step particle growth was more effective to avoid secondary nucleation than one-step growth approaches.

1.2.1.2. Gold Nanorods (AuNRs)

AuNRs have perhaps attracted the most attentions among all of the AuNPs with anisotropic morphologies, owing to their optical properties and applications.[67, 74, 75] Initially, AuNRs were synthesized via electrochemical methods; by using porous alumina or polycarbonate membrane as templates and cetyltrimethylammonium bromide (CTAB) as surfactants, shape and size control over the rod-like gold nanostructures was achieved.[76-78] The widespread recognition of the excellent properties of AuNRs was spurred by the development of the convenient three-step seed-mediated growth from 1999 to 2001 (Figure 1.4 (b)).[75] AuNRs with aspect ratios (length/diameter) between 8 and 20, and approximate dimensions of 150-1800 nm × 25 nm were generated through the simple wet chemistry method;[68] furthermore, the facile yet efficient seed-mediated growth also kick-started a surge of interest in the

fabrication of anisotropic metallic shapes.[79] Over the past decade, explosion of the researches on seed-mediated growth approaches now realizes the synthesis of a wide variety of AuNRs and allows the researchers to fully explore the application of their outstanding properties in biomedicine, sensing, electronics, and optics.[67-69, 80, 81]

1.2.1.3. Gold Nanoprisms

In the year of 2004, Sau et al. reported the synthesis of triangular shaped AuNPs through seed-mediated growth.[82] By deliberately adjusting the concentration of gold seeds, gold salts, CTAB, and ascorbic acid (AA), a number of structural architectures, from rod-, rectangle-, hexagon-, cube-, triangle-, and star-like AuNPs in high yield were produced under room temperature. However, the edge length of triangular AuNPs was not tunable, which limited their further optical, electrical, and catalytic applications. In the year of 2005, Millstone et al. reported the preparation of gold nanoprisms with an edge length of 144 ± 30 nm, and they first observed the in-plane quadrupole resonance mode of such structures.[83] One year later, the authors also realized the size control on gold nanoprisms; by using smaller nanoprisms as seeds, triangular shaped AuNPs within a size range from 100 nm to 300 nm could be produced (Figure 1.4 (c)).[25] However, it was pointed out the replicability of gold nanostructures was highly dependent on the surfactant (CTAB), including surfactant concentration, counterion, alkane chain length, and even chemical manufacturer.[65, 84, 85] In addition, synthetic additives such as halide ions were also major factors in directing crystal growth.[66, 86, 87] In the year of 2008, by starting with pure CTAB and deliberately adjusted iodide concentration, the authors finally achieved a reproducibly approach to synthesize gold nanoprisms.[65]

1.2.1.4. Gold Nanocubes

The synthesis of gold nanocubes via seed-mediated growth was realized in 2004, Sau et al. produced cubic AuNPs with the edge length of 66 nm at a yield of 80%.[82] Based on their work, in the year of 2007, Sheng et al. produced gold nanocubes with the average edge sizes ranging from 53 nm to 105 nm, by gradually varying the addition amounts

of gold seeds.[88] However, over the past decade, most efforts have been focused on the synthesis of octahedral and cubic AuNPs bounded by mixed crystalline surfaces, such as {111} and {100} facets,[89, 90] which weakened the conclusions on crystalline structure-dependent optical, electrical, or catalytic properties of AuNPs.[91] To obtain a more reliable consequential conclusion, Wang et al. developed a versatile seed-mediated growth method for selectively synthesizing single-crystalline cubic AuNPs (Figure 1.4 (d)) in 2009.[31] The authors attributed the single-crystalline structure to the cetylpyridinium chloride (CPC) capped gold seeds. Moreover, the shape formation of the AuNPs was also found to be dependent on some important parameters, such as surfactants, growth kinetics, and adsorbents.

1.2.1.5. Gold Nanospikes

In comparison with other morphologies, AuNPs with highly asymmetric branched structures are more difficult to synthesize and reproduce.[92] However, owing to their extremely high surface-to-volume ratio, which might allow researchers to optimize the surface properties at a minimum overall cost, a number of synthetic procedures were developed during the past decade.[93] In the year of 2003, Chen and co-workers reported the synthesis of branched AuNPs via seed-mediated growth method.[94] However, the yield was not high enough for practical applications. One year later, Hao et al. enhanced the yield of tripod AuNPs to 90%.[92] In 2006, branched AuNPs with more than four pods were first generated by Nehl et al., with a yield at only 14%.[95] From the year of 2008, synthesis protocols of gold nanospikes have been greatly improved;[23, 96, 97] gold nanostars with high tip coverage, yield close to 100%, narrow size distribution, and tunable sizes can be prepared via a simple two-step seed-mediated growth approach (Figure 1.4 (e)).[34]

1.2.1.6. Gold Nanocages

Hollow NPs cannot be prepared via seed-mediated growth, which only produces solid structures.[98] By far, three alternative techniques have been developed to produce metallic nanostructures with cavities and pores in their walls. The first one is template-

mediated method introduced by Caruso et al., however, complicated post-treatments limit the usefulness of this technique.[99] The second one is based on the common metallurgical Kirkendall effect which involves nonequilibrium mutual diffusion of counter atoms through a reaction interface.[100] The third and the most versatile technique is galvanic replacement approach, where atoms in a template nanostructure, normally produced by seed-mediated growth, are galvanic oxidized by ions of other metal in solution.[98, 101] Gold nanocages were the first hollow metallic NP prepared by this technique.[101] By mixing gold ions with a hot solution of silver nanocubes, gold nanocages with empty inside and porous surface were produced (Figure 1.4 (f)).[36] Furthermore, Xia's group modified the procedures of galvanic replacement technique and extended it to metallic nanocages of platinum, palladium, and bimetallic NPs.[102, 103]

1.2.2 Copper Nanowires (CuNWs)

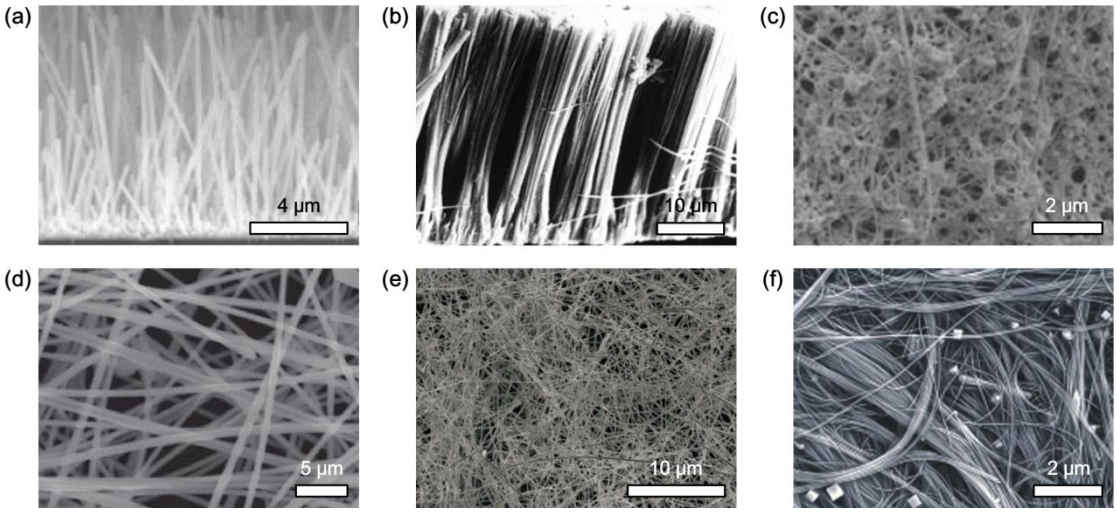

Figure 1.5 CuNWs fabricated through different approaches. (a) vapor deposition (© 2008 WILEY-VCH Verlag GmbH & Co. KGaA),[3] (b) electrochemical deposition (© 2002 IOP Publishing Ltd),[17] (c) template processing (© 2003 WILEY-VCH Verlag GmbH & Co. KGaA),[24] (d) hydrothermal method (© 2010 American Chemical Society),[29] (e) chemical reduction approach (© 2005 American Chemical Society),[32] and (f) chemical reduction approach with hexadecylamine (HDA) as a capping ligand (©2011 WILEY-VCH Verlag GmbH & Co. KGaA).[35]

One-dimensional (1D) nanomaterials, especially metallic nanowires with high aspect ratios, have attracted great attentions owing to their potential applications, such as

interconnects in nanofabrication,[104] optoelectronics,[105] nanosensors,[21] nano-biotechnology,[67] and electron emitters.[106] Copper is perhaps the most frequently used metals due to its high electrical conductivity and low cost.[107] For future bottom-up assembly, fabrication of CuNWs in large quantity and good uniformity is raising significant demands. However, in comparison with silver and gold, synthesis of CuNWs is still in a rudimentary state.[108-110] In recent years, a number of synthetic strategies, including vapor deposition,[3] electrochemical deposition,[111] template processing,[24] hydrothermal methods,[29] and chemical reduction approach[35] have been developed (Figure 1.5). In this subsection, the evolution of these methods is briefly introduced.

1.2.2.1. Vapor Deposition

In the year of 2003, Liu et al. introduced a one-step procedure to generate CuNWs free of defects and uniform in diameter.[107] Under vacuum condition, copper vapor was generated and re-deposited at around 800 ℃, resulting in nanowires with up to 20 μm in length. One year later, Park and co-workers produced CuNWs under a relatively low temperature (250 ℃) via chemical vapor deposition.[112] The crystalline structures was greatly improved by Kim et al., in the year of 2008, CuNWs with well-defined five-twinned nanostructures were deposited at a temperature around 200-300 ℃ under 0.1-1.0 Torr by using argon as a carrier gas (Figure 1.5 (a)).[3] However, high cost and strict conditions of vapor deposition are still limiting the large-scale production of CuNWs for industrial applications.

1.2.2.2. Electrochemical Deposition

Electrochemical deposition, generally with the assistance of templates, is probably the most widely used technique for the fabrication of copper nanostructures.[29] This is possibly because the procedures are inexpensive, moreover, the morphology and crystalline structures of CuNWs are easily controllable.[17] Usually, in an electrochemical reaction, CuNWs are deposited in the pores of a template, such as etched ion-track membranes, aluminum oxide structures, and surface step-edges. For

instance, Gao et al. produced CuNWs with the a uniform size (~60 nm in diameter and ~30 μm in length) by depositing copper sulphate within the nanochannels of porous anodic alumina templates (Figure 1.5 (b)).[17] By using polycarbonate etched ion-tracked membranes as templates, Molares et al. fabricated single- and poly-crystalline CuNWs with a diameter down to 30 nm via electrochemical deposition.[113] However, such a multi-step technique is only applicable for producing very small amounts of nanowires, thus it cannot satisfy the large quantity requirement of bottom-up assembly.

1.2.2.3. Template Processing

Template processing, pioneered by Martin, has been proven very successful in synthesizing metallic nanowires.[114] Briefly, with the utilizing of templates, including polymer channels, alumina membranes, and zeolites, nanowires of copper, nickel, silver, gold, and palladium are grown in a chemical reaction.[24] For instance, in the year of 2003, Yen et al. produced high aspect ratio CuNWs encapsulated in poly(dimethylsiloxane) (PDMS) under mild conditions. The diameter was in the range of 20-80 nm and the length could reach 10 μm (Figure 1.5 (c)).[24] In addition to normal templates, deoxyribonucleic acid (DNA) is also utilized to direct the formation of nanowires. In 2003, Monson et al. reported the growth of copper nanowire-like structures on DNA attached surface.[115] However, template processing is not feasible for large-scale production, mainly owing to its low yield and complicated procedures.[107]

1.2.2.4. Hydrothermal Methods

Hydrothermal method is recognized as one of the simplest ways to produce metallic nanowires in a large scale.[29] In the year of 2003, for the first time, Liu et al. synthesized CuNWs via hydrothermal method.[116] By applying Cu(II)-glycerol complex with the presence of phosphite, nanowires with average diameters of 85 nm and lengths of several tens of micrometers were produced at 120 ℃.[116] In 2006, Zhang et al. developed a one-step hydrothermal method to prepare CuNWs by using ascorbic acid as reducing agent and polyvinylpyrrolidone (PVP) as capping agent.[117] With the same reducing agent, ultra-long CuNWs were produced in 2007.[118] In the year of 2010,

large-scale synthesis of single-crystalline ultra-long CuNWs was achieved by Mohl et al. (Figure 1.5 (d)).[29] In this work, Glucose and hexadecylamine (HDA) were firstly utilized as shape-directing agents in hydrothermal methods.

1.2.2.5. Chemical Reduction Approach

In the year of 2005, high-quality ultra-long CuNWs (90-120 nm in diameter, 40-50 μm in length) were synthesized by chemical reduction approach in aqueous solution for the first time (Figure 1.5 (e)).[32] In this work, copper precursors ($Cu(NO_3)_2$) are reduced by hydrazine with the existence of ethylenediamine (EDA) and highly concentrated sodium hydroxide (NaOH). The method is simple and versatile, however, CuNWs are difficult to separate, which limits the further investigation of their optical/electrical/thermal properties. In the year of 2011, this method was modified by Rathmell et al.; with the help of an ice bath and PVP coverage, long and thin CuNWs (with the diameter less than 60 nm and the length more than 20 μm) with an improved dispersion was fabricated. Moreover, flexible, transparent, and electrical conductive film was realized by uniformly coating these nanowires on an plastic substrate.[19] In the same year, HDA was utilized as the capping agents for CuNWs in chemical reduction approach.[35] Thanks to the good selectivity towards {100} facets of HDA, CuNWs with high purity and good uniformity were produced in a large scale (Figure 1.5 (f)).

1.3 Metallic Nanoparticle-Based Electrocatalytic Electrodes

Substantial research progress has been made in the past 20 years in the controlled synthesis of metallic NPs.[79] To date, a variety of high-quality particles with diverse shapes and sizes can be obtained via wet chemistry approach. The unique structural and functional features of these metallic NPs are being utilized for the development of advanced electrochemical catalysts for energy and environmental applications. In the first section of this part, various strategies of immobilizing NPs onto substrate surfaces

are described; in the second section, the current research activities in electrocatalysis of metallic nanoparticle-modified electrodes are summarized.

1.3.1 Design of Metallic Nanoparticle-Based Electrocatalytic Electrodes

Immobilization of the metallic NPs onto substrate surface is a critical step for the electrochemical applications. A successful modification might allow researchers to not only enhance the power of the resulted devices but also characterize the electrochemical properties of NPs accurately. The viable assembling approaches include drop casting (physical binding), chemical linking, and electrodeposition.

1.3.1.1. Drop Casting

Drop casting is probably the most straightforward particle-immobilization strategy available; therefore, it is commonly employed to characterize the electrocatalytic properties of newly synthesized metallic NPs.[14, 16, 22] Typically, the procedure is to simply apply a droplet of NP solutions onto a solid substrate surface and then followed by drying in air or inert gas. However, NPs are attached on the surface by physical interaction, which is too weak to keep them fixed on the substrate in an electrochemical reaction. Therefore, a layer of polymeric ionomers, such as Nafion, is generally applied to improve the stability of the modified electrodes.[22] Meanwhile, drop casting approach is also suffering from the lack of control on the dispersion of NPs, which might influences the accuracy of the conclusion on their electrocatalytic activity.

1.3.1.2. Chemical Linking

The bounding strength between substrate and metallic NPs can be enhanced by virtue of chemical linking, including covalent binding and electrostatic interaction.

For glass substrate surface, the first example of modifying metallic NPs via chemical binding showed up in 1996.[119] By immersing a clean indium tin oxide (ITO) glass slide in the ethanolic solution of (3-aminopropyl)trimethoxysilane (APTMS) for

approximately 20 min, APTMS/ITO electrode was obtained. Then, the electrode was further dipped in the solution of AuNPs for AuNPs/APTMS/ITO electrode. Moreover, additional particle binding was realized by immersing the electrode into AuNP solution repeatedly. Finally, highly conductive AuNP films with controllable thickness were comprised through layer by layer (LBL) assembly in aqueous solution without any redox chemistry, photochemistry, or heating.

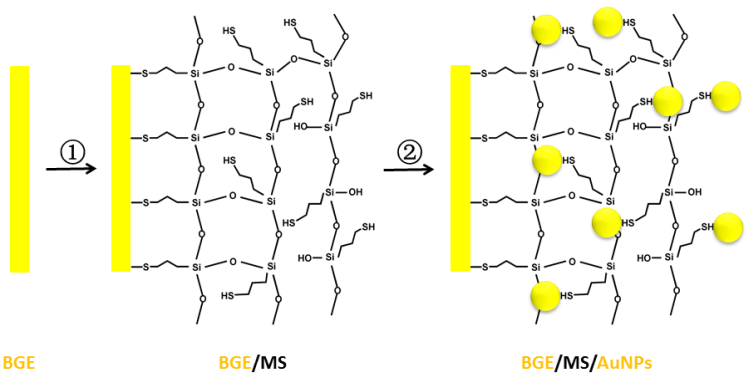

Scheme 1.1 Idealistic representation of self-assembly of thiol-terminated silica gel network and AuNPs on a BGE substrate via covalent binding. (© 2001 American Chemical Society)[2]

For metal electrodes such as gold or platinum, organosulfur compounds are ideal linkers between the NPs and electrode surface. For instance, in the year of 2000, Ikeda and co-workers reported a facile approach to immobilize AuNPs on the surface of bulk gold electrodes (BGEs) via covalent binding. The detailed procedures are presented in Scheme 1.1.[2] In the first step, a freshly polished BGE was immersed the prehydrolyzed methanolic solution of mercaptopropyltrimethoxysilane (MS) for a desired period. Since MS is a thiol-terminated molecule, it was assembled on the surface of BGEs via the Au-S interaction. In the second step, AuNPs were then self-assembled on the MS-modified electrodes by dipping the electrodes into AuNP solutions. The authors claimed that the BGE/MS/AuNP electrode was highly reproducible and stable, and the immobilization approach was universal for both metallic and semiconductor nanostructures. However, covalent binds between metallic NPs and substrate were restricted to certain classes of organics, owing to the high steric demand of covalent chemistry.

Electrostatic interaction is another alternative, since little steric requirement is required. The application of electrostatic binding for nanocomposite films can be dated back to 1997, when multilayers of polyelectrolytes (PEs) were fabricated by absorbing polyanions and polycations consecutively.[120] In the same year, Calvert and co-workers realized the layered nanocomposites of metallic NPs and PEs via electrostatic interaction.[11] The fabrication procedures are illustrated in Scheme 1.2. The first layer was positively charged poly(ethylenecimine) (PEI) film. After rinsing the PEI-modified electrode, convective depositions of poly(styrene sulfonate sodium salt) (PSS) and poly(allylaminehydrochloride) (PAH) were conducted. Since the uppermost layer of PAH was positive, negative charged citrate capped AuNPs were finally assembled. This methodology leads to a new strategy of constructing nanocomposites with controllable electrochemical properties. Currently, it has been regarded one of the most prevalent approaches for modifying metallic NPs on various electrode surfaces.[121]

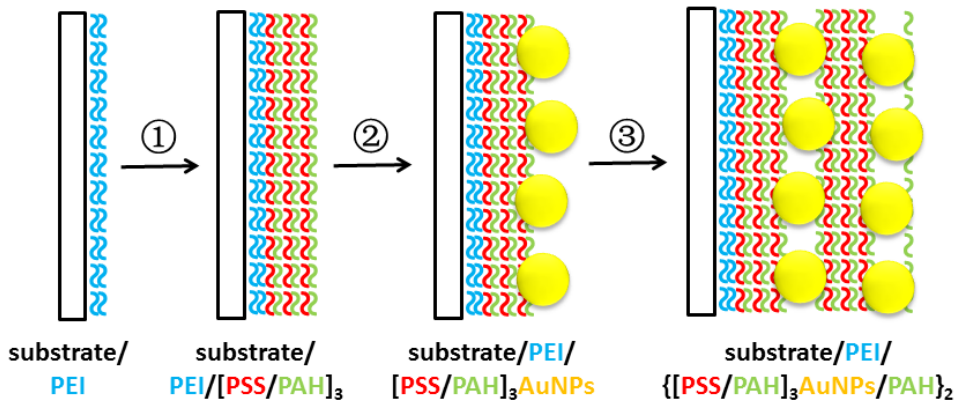

Scheme 1.2 Process for fabricating AuNP/PE multilayers on a substrate (silicon wafers or glass slides). The blue, red, and green colors represented PEI, PSS, and PAH, respectively. Note that this drawing is an oversimplification of the actual layer structure. (© 1997 WILEY-VCH Verlag GmbH & Co. KGaA)[11]

1.3.1.3. Electrochemical Deposition

Besides drop casting and chemical linking, electrochemical deposition is another useful method. By far, Au nanostructures in various morphologies have been obtained via this one-step process, such as rods[10] and spikes.[23] In the year of 2006, Tian et al. produced pyramidal, rod-like, and spherical Au nanostructures through electrochemical deposition (Figure 1.6 (a-c)).[10] In the first step, gold film with the thickness of 50 nm

was coated on a clean ITO glass slide. In the second step, by deliberately controlling the potential versus the reference electrode and the concentration of Au precursors, Au nanostructures with various morphologies were electrodeposited on the sputtered Au films in the aqueous solution of 0.1 M $HClO_4$.

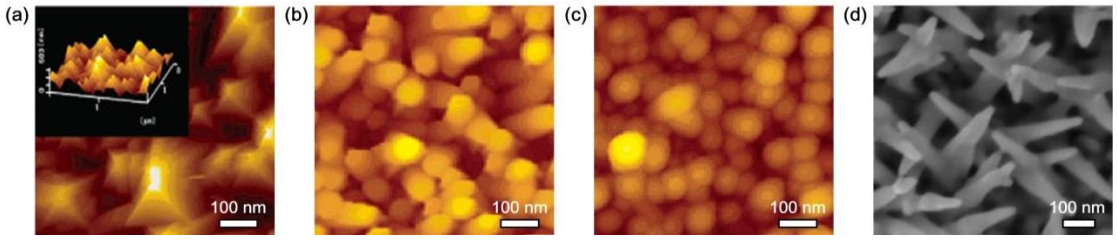

Figure 1.6 Au structures generated via electrochemical deposition. Atomic force microscopy (AFM) images of (a) pyramid-like, (b) rod-like, and (c) spherical AuNPs. (© 2006 American Chemical Society)[10] (d) A SEM image of Au micro-spikes. (© 2009 The Royal Society of Chemistry)[23]

AuNPs with dendrite morphology were difficult to achieve. Initially, organic surfactants[122] and templates with functionalization patterns[123] were employ to help. However, organic additives may influence the surface chemistry of the resultant material. Moreover, the preparation and post-treatment of templates are time-consuming. Thus an electrochemical route to construct branched gold nanostructures on "clean" surface without introducing any organic surfactant or template was urgently required. In the year of 2009, Bhargava and O'Mullane reported the electrochemical deposition of Au micro-spikes without the prior modification of the electrode surface (Figure 1.6 (d)).[23] Inorganic $Pb(CH_3COO)_2$ was employed as the directional growth agent.

1.3.2 Electrocatalytic Performance of Metallic Nanoparticle-Based Electrodes

Size- and shape-dependent metallic NPs may change the landscape of electrocatalysis for energy applications. In this part, representative examples in electrochemical applications of the metallic nanoparticle-based electrodes are highlighted.

1.3.2.1. Oxygen Reduction Reaction (ORR)

Extensive studies have been carried out to enhance the electrocatalytic efficiency towards ORR, since it is a critical step in the practical applications of energy-related fields, such as fuel-cells and batteries.[124] The electrocatalytic activities are greatly influenced by the surface structure of NPs, because most electrochemical reactions occur on the interface between NPs and solutions.

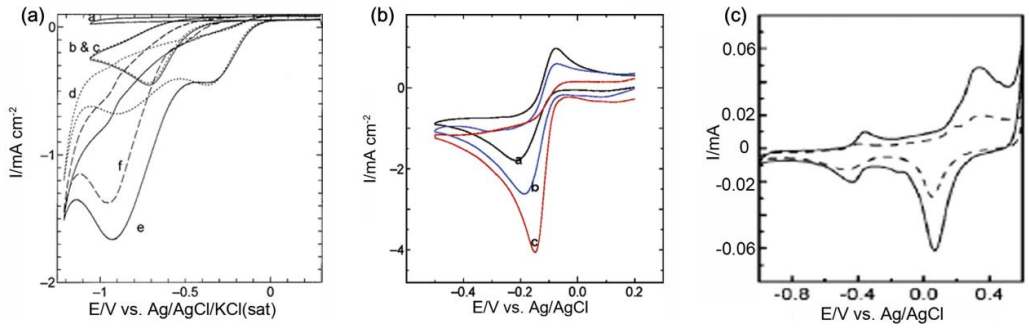

Figure 1.7 Electrocatalytic properties of AuNP-based electrodes towards ORR. (a) Cyclic voltammetry (CV) curves obtained towards ORR at (a-solid line) bare GCE and (b-dashed line) AuNP-deposited GCE in O_2-saturated 0.1 M PBS (pH=7.2). Potential scan rate: 100 mV/s. (© 2003 The Electrochemical Society)[13] (b) CV curves obtained at the electrodeposited (a-black line) pyramidal, (b-blue line) rod-like, and (c-red line) spherical gold nanostructures in O_2-saturated 0.5 M aqueous KOH. Potential scan rate: 50 mV/s. (© 2006 American Chemical Society)[10] (c) CV curves of (dashed) unmodified gold electrodes and (solid) Au nanospikes recorded at 50 mV/s in 1 M NaOH aqueous solution. (© 2009 The Royal Society of Chemistry)[23]

Crystalline structure-dependent electrochemical responses towards ORR of BGEs were extensively discussed in previous publications.[125, 126] From the beginning of the 21th century, attentions have been switched to nano-sized Au particles. In 2003, Ohsaka and co-workers investigated the electrocatalytic behaviors of AuNP-electrodeposited glassy carbon electrodes (GCEs) towards ORR. They claimed the electrocatalytic activity of 10 nm AuNP film was the same to that of a BGE (Figure 1.7 (a)), which was attributed to the large active surface area of AuNPs. In 2006, Tian et al. studied the shape-dependent electrocatalytic performance of pyramidal, rod-like, and spherical gold nanostructures produced by overpotential deposition (Figure 1.6 (a-c), respectively).[10]

They found out that pyramidal AuNPs with the highest coverage of (111) facets possessed the lowest oxygen reduction activity in comparison with other nanostructures (Figure 1.7 (b)). Thus they claimed that AuNPs terminated by (100) and (110) surfaces were more electrocatalytically active than those with (111) facets. In 2009, O'Mullane and Bhargava compared the electrocatalytic efficiency towards ORR of Au nanospikes (Figure 1.6 (d)) to the one of BGEs. Notably, a significant enhancement in current density and a negative shift in onset potential were observed, which was caused by the existence of high electrocatalytic activity of gold (311) and (111) facets in gold nanospikes. (Figure 1.7 (c))

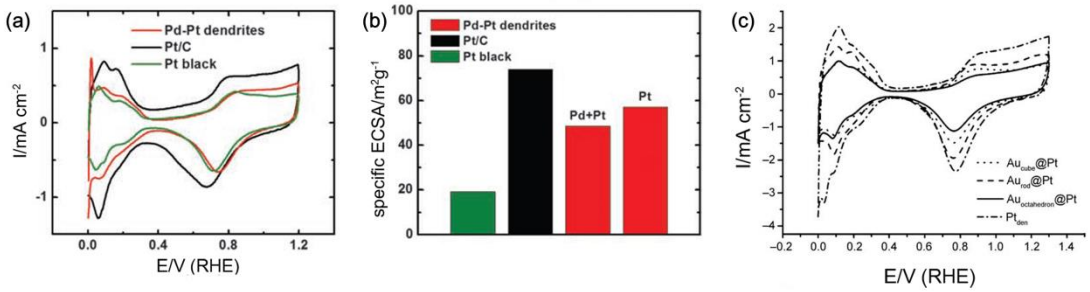

Figure 1.8 (a and b) A Comparison of electrocatalytic properties among Pd-Pt nanodendrites, Pt/C catalyst, and Pt black. (a) CV curves recorded at room temperature in an Ar-purged 0.1 M $HClO_4$ solution with a sweep rate of 50 mV/s. (b) Specific ECSAs for the Pd-Pt nanodendrites, Pt/C catalyst, and Pt black. (© 2009 American Association for the Advancement of Science)[14] (c) CV curves of the $Au_{octahedron}$@Pt, Au_{rod}@Pt, Au_{cube}@Pt, and Pt_{den} in 0.1 M $HClO_4$ at a scan rate of 50 mV/s. (© 2010 WILEY-VCH Verlag GmbH & Co. KGaA)[16]

Platinum is currently considered as the most efficient metallic electrocatalyst towards oxygen reactions in polymer electrolyte membrane fuel cells, however, monometallic platinum nanoparticle (PtNP)-based electrodes often suffer from poisoning.[40] To overcome this barrier, Xia's group synthesized bimetallic Pd@Pt nanodendrites in the year of 2009.[14] The bimetallic NPs possessed the highest electrocatalytic activity towards ORR, when compared with the efficiency of two commercial Pt based catalysts; fine particles of Pt supported on porous carbon materials (Pt/C) and Pt black (Figure 1.8 (a)). Moreover, the results from electrochemically active surface area (ECSA) calculation indicated that the highly branched nanostructures offered a reasonably high surface area despite their relatively large overall particle size (Figure 1.8 (b)).

Han and co-workers brought the synthesis of Pt-based bimetallic NPs into a new stage. In the year of 2010, branched Au@Pt nanodendrites with various core morphologies including rods, cubes, and octahedron were produced.[16] The core shape-dependent electrocatalytic activities towards ORR are presented in Figure 1.8; $Au_{octahedron}$@Pt NPs exhibited the highest catalytic efficiency, possibly owing to its (111)-orientation-rich Pt surface. Notably, the electrocatalytic behaviors towards ORR of branched Au@Pt nanodendrites were very stable; the current density remained at the same level even after 3,000 cycles of electrochemical scanning.

1.3.2.2. Methanol Oxidation Reaction (MOR)

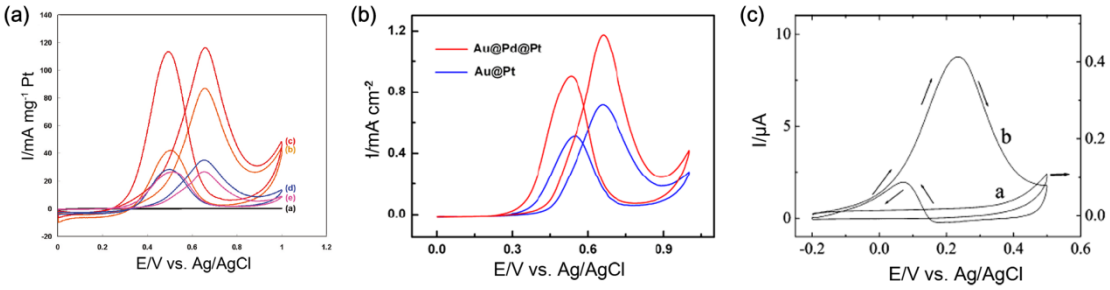

Figure 1.9 Electrocatalytic properties towards MOR of metallic NPs. (a) Pt-mass-normalized CV curves displaying the catalyzed oxidation of methanol, using (a-black) AuNPs, (b-d) Au@Pt NPs, and (e-purple) dendritic PtNPs. The Au@Pt NPs were prepared with different Pt/Au molar ratios at (b-orange) 0.33 (c-red) 1.0, and (d-blue) 2.0. (© 2010 American Chemical Society)[7] (b) CV curves towards MOR catalyzed by (red) Au@Pd@Pt NPs and (blue) Au@Pt NPs, respectively, in 0.5 M H_2SO_4 with 1 M methanol. Scan rate: 10 mV/s. (© 2010 American Chemical Society)[22] (c) CV curves for the oxidation of methanol (0.25 mM) at (a) APTMS and (b) APTMS/flower-like AuNPs modified electrodes in 0.1 M KOH. Scan rate: 10 mV/s. (© 2007 American Chemical Society)[27]

Methanol oxidation reaction (MOR) is a crucial anodic reaction in direct methanol fuel cells.[127] Currently, metallic NPs are regarded as promising candidates for commercial MOR catalysts, since they can provide high ECSA with a low cost. As shown in Figure 1.9 (a), branched Au@Pt nanostructures with the Pt/Au molar ratios at 0.5 and 1.0 exhibited superior catalytic activity; in comparison of monometallic Pt nanodendrites, a much higher current density was observed, which was decided by the ECSA. To enhance the electrocatalytically-effective areas, in 2010, Liang Wang and Yusuke

Yamauchi synthesized branched Au@Pd@Pt NPs via one-pot synthesis.[22] As shown in Fig. 8 B, the three layered branched nanostructures showed higher electrocatalytic activity towards methanol oxidation as compared to the bimetallic Au@Pt NPs owing to its higher level of electrocatalytic active areas. In 2007, flower-like Au NPs were also employed as electrocatalyst for oxidization of methanol (Fig. 8 C).

1.4 Metallic Aerogels as Electrical Conductors

Besides the electrocatalytic performances, excellent electrical properties of metallic nanostructures have also attracted great concerns. Metallic aerogels are recently developed materials with ultimate properties of metals.[42] They combine the merits from both bulk metals (such as excellent electrical conductivity and catalytic activity) and nanomaterials (such as ultralow density and high surface area). Therefore, the introduction of metallic aerogels might realize extensive technological possibilities, such as battery-like supercapacitors,[128] high power-density batteries,[129] as well as lightweight structures. In this part, fabrication approaches and potential applications of metallic aerogels or metallic NPs based composite aerogels are briefly summarized.

1.4.1 Fabrication Approaches for Metallic Aerogels

Unlike highly porous structures from other substances, including silica,[130] metal oxides,[131] carbon materials,[132] and organic polymers,[133] metallic aerogel is difficult to achieve, since most conventional techniques, such as chemical vapor deposition and atomic layer deposition, could not generate 3D large-scale continuous metals. To face this challenge, several approaches were developed, including templating, dealloying, sol-gel, nanosmelting, and combustion.

1.4.1.1. Templating Approach

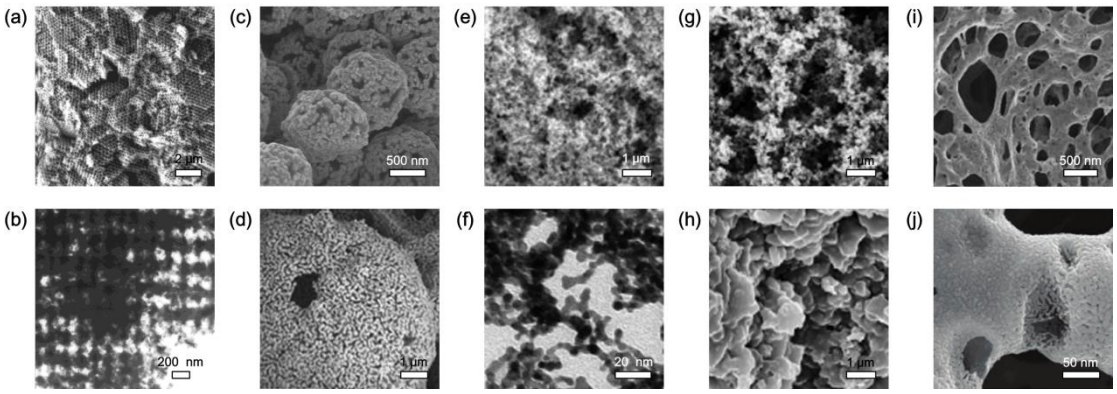

Figure 1.10 Metallic monoliths aerogels fabricated via various approaches. (a) SEM and (b) TEM images of Ni foams produced by templating approach. (© 1999 WILEY-VCH Verlag GmbH & Co. KGaA)[5] (c) SEM images of gold NPs deposited on PS and (d) gold shell after dealloying. (© 2007 American Chemical Society)[18] (e) SEM and (f) TEM images of Pt aerogel from sol-gel approach. (© 1999 WILEY-VCH Verlag GmbH & Co. KGaA)[26] (g and h) SEM images of Fe aerogels generated via nanosmelting. (© 2009 The Royal Society of Chemistry)[30] (i and j) SEM images of Fe nanofoams from combustion synthesis. (© 2006 American Chemical Society)[33]

Templating approach is a seemingly straightforward technique for metallic monolith aerogels.[42] The overall process involves depositing continuous metals on the surface of porous templates, normally colloidal silica particles[134] or polystyrene (PS) spheres.[5] For instance, in the year of 1999, Jiang et al. demonstrated the fabrication of metallic nanofoams from Ni, Cu, Au, Pt, and Au by utilizing thiol-functionalized colloidal silica spheres as a template.[134] In this approach, AuNPs were first deposited on the template through electroless deposition technique, which followed by the deposition for a wide range of metals. Free-standing metallic thin films with uniform pore size and high surface area were produced. In the same year, Yan et al. reported a similar technique for producing porous Ni films by using ordered PS spheres as a template.[5] The pore size of Ni aerogels was in the range of 200 to 500 nm, and the surface area was from 590 to 1,760 m^2mol^{-1} (Figure 1.10 (a) and (b)). Templating approach can produce metallic structures with regular and ordered porosity, which exhibit promising potentials in optical applications. However, the approach is only limited to the

generation of 2D thin films and the post-treatment is undesirable in large-scale production.

1.4.1.2. Dealloying Approach

Dealloying is a variant of templating approach, which is used to produce metallic aerogels with disordered porosity.[135-137] In this approach, an alloy of target metal and one or more kinds of relatively more reactive metals is prepared. (Generally, the alloy consists of silver and gold or copper and gold.) Then, the less-noble metals are selectively removed via electrochemical or acid etching, leaving behind a porous framework of the target metal. For instance, Nyce et al. fabricated nanoporous Au monolith shells with the diameter of 9.6 mm and the thickness of 200 nm via dealloying approach.[18] In the first step, an alloy of gold (15 atom%) and silver (85 atom%) was deposited on micro-sized PS spheres. In the second step, PS spheres were pyrolyzed away at 400 ℃ under the protection of inert atmosphere. In the final step, the alloy was etched by concentrated nitric acid aqueous solution, leaving a hierarchically nanoporous gold foam (Figure 1.10 (c) and (d)). In comparison with templating technique, dealloying approach solves the precursor diffusion problem; however, the thickness of the monolith is generally less than 1 mm, which restricts the nanofoams to thin films. In addition, dealloying approach is only effective for a handful of metals.

1.4.1.3. Sol-Gel Approach

Sol-gel technique has been proven as a powerful pathway to produce metallic NPs, however, it is surprisingly difficult to fabricate metallic gels for supercritical or freeze drying directly through sol-gel approach. A synthetic pathway for aerogels from surfactant-stabilized metal chalcogenides was first demonstrated by Brock et al. by oxidative removal of the surfactant groups.[138] By using the same method, Tappan et al. evaluated the potential of sol-gel approach for the production of metallic aerogels.[42] AuNPs with solubility in water up to 30 % were chosen as the model system. After 48 hours following the addition of H_2O_2 (30 wt%), gold aerogels in terms of orange precipitation was obtained. In the year of 2009, Bigall et al. synthesized hydrogels and

aerogels from noble metal NPs (Pt, Au/Ag alloy, and Pt/Ag alloy) via sol-gel approach.[26] The gel formation was realized by adding ethanol or H_2O_2 into highly concentrated metallic NP solution. Pt aerogels with different morphologies were obtained after ligand removal (Figure 1.10 (e) and (f)), however, gels from only secondary or tertiary particles were obtained for monometallic Au or Ag. All of the above examples suggest the possibility of controlled ligand removal for the producing metallic gel network; however, the stability of the metallic aerogels as well as the shape control in the process of sol-gel approach still require deliberate investigations.

1.4.1.4. Nanosmelting

Nanosmelting is one of the most effective techniques for producing metallic aerogels, which was introduced by Leventis et al. in the year of 2009.[30] The authors synthesized iron mesoporous aerogels with high specific surface areas (~ 5,300 to 16,800 m^2mol^{-1}) and low density (0.046 $g\,cm^{-3}$) via "nanosmelting" hybrid polymer/metal oxide aerogels (Figure 1.10 (g) and (h)). Briefly, hybrid network gels consisting of interpenetrating resorcinol-formaldehyde (RF) polymer and iron oxide were prepared via sol-gel process. Then, the hybrid gels were supercritically dried for hybrid aerogels. Finally, the aerogels were pyrolyzed at temperatures from 800 to 1,000 ℃ under the protection of Ar gas. At this stage, CO_2 was generated during the dehydration of RF network, which reduced the iron oxide frame into magnetic and electrically conductive metallic iron aerogels. In the same year, nanosmelting approach was extended to other metals, including Co, Ni, Cu, and Sn.[139] In comparison with other techniques listed above, the process of nanosmelting approach is the most direct; moreover, the resulted monolith aerogels can be scaled to dimensions in the centimeter range with any shape. However, for metals without a stable oxides network (such as Au, for example) and cannot be reduced by CO_2 (such as Ti or Zr), it is still unclear whether nanosmelting technique is feasible.

1.4.1.5. Combustion Synthesis

Up till now, combustion synthesis is recognized as one of the most direct and universal approaches for nanoporous metallic aerogels.[42] Generally, the process involves the decomposition of energetic substances into porous materials. Combustion synthesis techniques have been commonly utilized in fabricating foam structures from a wide range of materials, such as metal oxides, ceramics, and intermetallics.[140] In the year of 2008, Erri et al. reported the production of nickel and nickel/nickel oxide via combustion of nickel nitrates with glycine in air.[141] The pore size was between 100 μm to 1 mm, which exceeded the nanometer range, thus the nickel aerogels possessed a relatively low specific surface area (50 to 200 m^2mol^{-1}). Hunt et al. introduced a different combustion synthesis route for NiAl alloy foams.[142] In this process, fluorinated organic ligands covered Al particles were prepared and employed as gasifying agents. Then, they were combined with micron-sized Al particles and nanometer-sized Ni particles and the mixture was pressed into pellets. Finally, the pellets were laser ignited, leaving porous NiAl foam with a porosity from 10 % to 80 %. In the year of 2006, combustion synthesis was first proved to be feasible for the fabrication of nanoporous metallic aerogels by Tappan et al.[33] In this approach, metal bistetrazolamine complexes were chosen as the raw materials for the pellets. After ignition in inert gas, nanoporous iron aerogels with remarkably high specific surface area (2,000 to 11,400 m^2mol^{-1}) was achieved (Figure 1.10 (i) and (j)). Combustion synthesis is extendable to most metals, including Co, Ni, Cu, Ag, Au, Pd, Pt, and Ti.[42] Moreover, the fabrication of composite nanomaterials from metallic NPs and other inorganic/organic have also been demonstrated.[42] In addition, the shape, dimension, density, and porosity of the final products can be simply controlled through experimental conditions.

1.4.2 Electrical Applications of Metallic Nanoparticle-Based Composites

Research in metallic nanostructure-based electrodes is fuelled by diverse technological demands, since nanosized-matels possess high surface-to-volume ratios and excellent electrical properties. However, unlike conventional materials, such as conductive polymers[143] or carbon materials,[144] metallic NPs are neither mechanically flexible nor environmentally stable enough for practical applications including flexible displays and smart skins.[145] A promising solution is to fabricate metallic NP-polymer composites, which combines the flexibility of polymers and the electrical conductivity of metals. By far, several successful strategies have been developed for metallic NP-polymer composite conductors with potential applications in flexible transparent electrodes,[6, 19] stretchable conductors,[9, 21, 28] and 3D electrical conductive elastomers.

1.4.2.1. Flexible Transparent Electrodes

The emergence of potable electronics dramatically stimulates the researches on flexible transparent electrodes. Currently, the most critical challenge is the scarcity of indium resource, which is commonly regarded as an ideal choice for most transparent electrodes. Several alternatives were reported as the substitutes for ITO, such as carbon nanotubes (CNTs),[146] graphene,[147] and metal grids;[148] however, the light transmittance and electrical conductivity is still relatively low.

Random sliver nanowire (AgNW) networks were reported to show a similar optoelectronic behavior to ITO, which makes them promising candidates to replace ITO.[149, 150] However, the deposited AgNWs were always coarse and brittle, keeping the network from large-scale applications. In the year of 2010, Zeng et al. fabricated a flexible transparent electrode with low surface roughness and high mechanical strength by burying AgNWs in poly(vinyl alcohol) (PVA) matrix (Figure 1.11 (a-d)).[6] For a composite film with the AgNW deposition density at 32 mg m^{-2}, the optical transmission at 550 nm was 88.0% with the sheet resistance around 182 Ω. In addition,

for a AgNW-PVA film with the thickness of 130 nm, the sheet resistance only enhanced for 2-3 times after 250 cycles of bending.

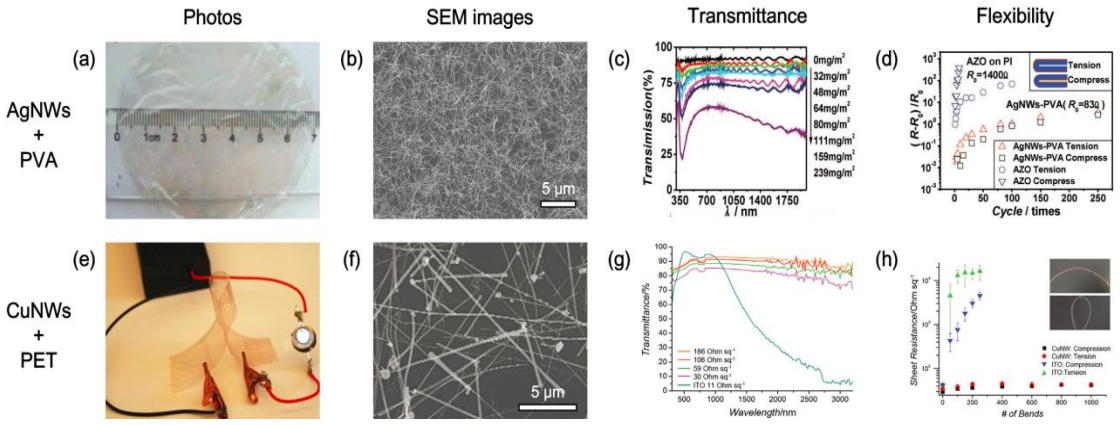

Figure 1.11 Transparent electrodes constructed from (a-d) AgNWs and (e-h) CuNWs. (a) A photograph, (b) an SEM image, and (c) UV-Vis-NIR transmission spectra of AgNW-PVA electrodes. (d) The increase in resistance after cycles of folding up. (© 2010 WILEY-VCH Verlag GmbH & Co. KGaA)[6] (a) A photograph, (b) an SEM image, and (c) UV-Vis-NIR transmission spectra of CuNW films. (d) Plot of sheet resistance versus number of bends for CuNW films (85% transparent) and ITO on PET. Inset shows the radius of curvature before (10 mm) and after bending (2.5 mm). (© 2011 WILEY-VCH Verlag GmbH & Co. KGaA)[19]

In comparison with silver, copper shows a similar conductivity; however, it only costs 1% of the price of silver.[19] Motivated by these advantages of copper, Rathmell et al. reported the production of CuNW film in 2011 (Figure 1.11 (e-h)).[19] In this work, long (length > 20 μm) and thin (diameter < 60 nm) CuNWs were synthesized and deposited on the surface of poly(ethylene terephthalate) (PET) substrate. With the help of plasma cleansing and thermal treatment, the sheet resistance of CuNW films was reduced to 25 Ω with a transmittance at 83%. Moreover, no obvious enhancement of resistance was observed even after 1,000 cycles of bending. However, owing to the poor dispersions of CuNWs, it was difficult to utilize conventional film forming technique, such as spray-coating, to fabrication large-scale CuNW films.

1.4.2.2. Stretchable Conductors

Rigid conductors can hardly meet the requirements of advanced technologies, such as flexible electronics, soft robotics, and cadiostimulating implants.[151-153] Therefore, a variety of materials have been explored as promising candidates for stretchable conductors, such as wavy thin metals,[154, 155] metal-coated net-shaped plastic films,[156] graphene films,[147] and CNT-based composites.[157-159] However, the above materials often exhibited limited performances, including low electrical conductivity, poor mechanical stretchability, and obvious resistance increase with applied strain. To solve this problem, an alternative which involved encapsulating metallic structures into neutral mechanical plane layouts was developed; meanwhile, this strategy requires expensive photolithography and vacuum deposition of metals.[151]

In the year of 2012, Xu et al. developed a simple yet economical route to fabricate stretchable conductors by embedding AgNWs in the surface layer of PDMS (Figure 1.12 (a-d)).[9] The electrical conductivity was around 8,130 S cm^{-1}, and it was reduced to 5,285 S cm^{-1} after several circles of stretching within the range of 0-50%. To further enhance the mechanical strength of AgNW-based stretchable conductors, polyurethane (PU) sponge was employed by Ge et al.[21] In this work, a binary network from AgNWs and PU sponge was designed and encapsulated in PDMS (Figure 1.12 (e-h)). The PUS-AgNW-PDMS conductors showed excellent electrical conductivity (exceeding 19.2 S cm^{-1}). Meanwhile, only slight variation in resistance (from 10.1 S cm^{-1} to 9.7 S cm^{-1}) was observed under bending and stretching.

In comparison with 1D metallic nanostructures, spherical NPs appeared as an unfavorable candidate for the fillings of composite stretchable conductors; however, they could provide greater matrix mobility. In the year of 2013, Kim et al. fabricated free-standing film conductors from AuNPs and PU by either LBL technique or vacuum-assisted flocculation (VAF) approach (Figure 1.12 (i-l)).[28] AuNP-PU films from LBL and VAF exhibited extremely high electrical conductivity (6,800 S cm^{-1} and 510 S cm^{-1}, respectively). Moreover, the maximum tensile strains were 16% and 75%,

respectively. This work also analyzed the dynamic self-organization of AuNPs under stress, and the authors further developed a modified percolation theory which excellently incorporated the self-assembly behavior of AuNPs with the experimental data.

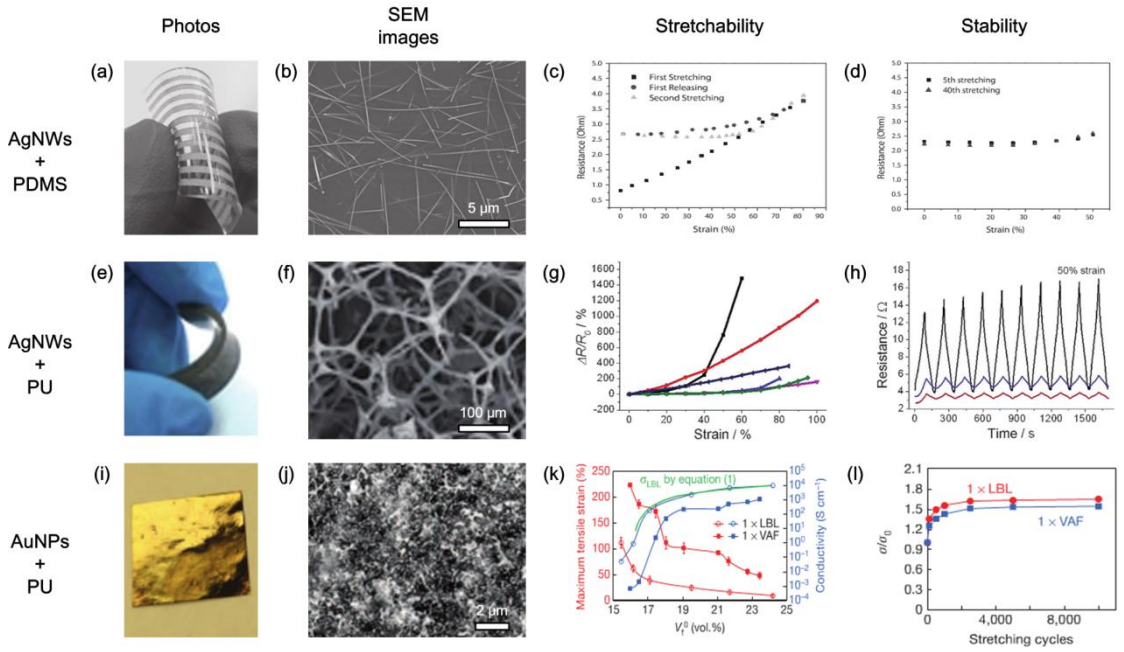

Figure 1.12 Stretchable conductors constructed from (a-d) AgNW/PDMS, (e-h) PU sponge-AgNW-PDMS, and (i-l) PU-AuNPs. (a) A photograph and (b) an SEM image of AgNW/PDNS conductors. (c) Resistance of a AgNW/PDMS conductor as a function of tensile strain. (d) Resistance as a function of tensile strains (0-50%) for the AgNW/PDMS stretchable conductos in the 5th and the 40th stretching cycles. (© 2012 WILEY-VCH Verlag GmbH & Co. KGaA)[9] (e) A photograph and (f) an SEM image of PU sponge-AgNW-PDMS conductor. (g) Variation of normalized resistance ($\Delta R/R_0$) as a function of tensile strain (up to 100 % in the first stretch) and (h) resistance responses on PU sponge-AgNW-PDMS and other materials. (See the original paper for more detailed information.) (© 2013 WILEY-VCH Verlag GmbH & Co. KGaA)[21] (i) A photograph and (j) an SEM image of a PU-AuNP film. (k) Dependent of strain and conductivity and (l) changes in conductivity of a PU-AuNP film. (See the original paper for more detailed information.) (© 2013 Macmillan Publishers Limited.)[28]

1.4.2.3. 3D Conductive Elastomers

Self-supported 3D elastic conductors also receive great attention in the development of future technology, owing to its high porosity, large specific area, low density, and excellent electrical and mechanical properties. By far, carbon materials, such as

CNTs[160] and graphene,[132] have been demonstrated as promising candidates for electrical conductive elastomers. Meanwhile, metallic nanostructures are also regarded as potential alternatives; besides the excellent conductivity, incorporation of metals might bring in more attractive characristics, including optical and catalytic performances.

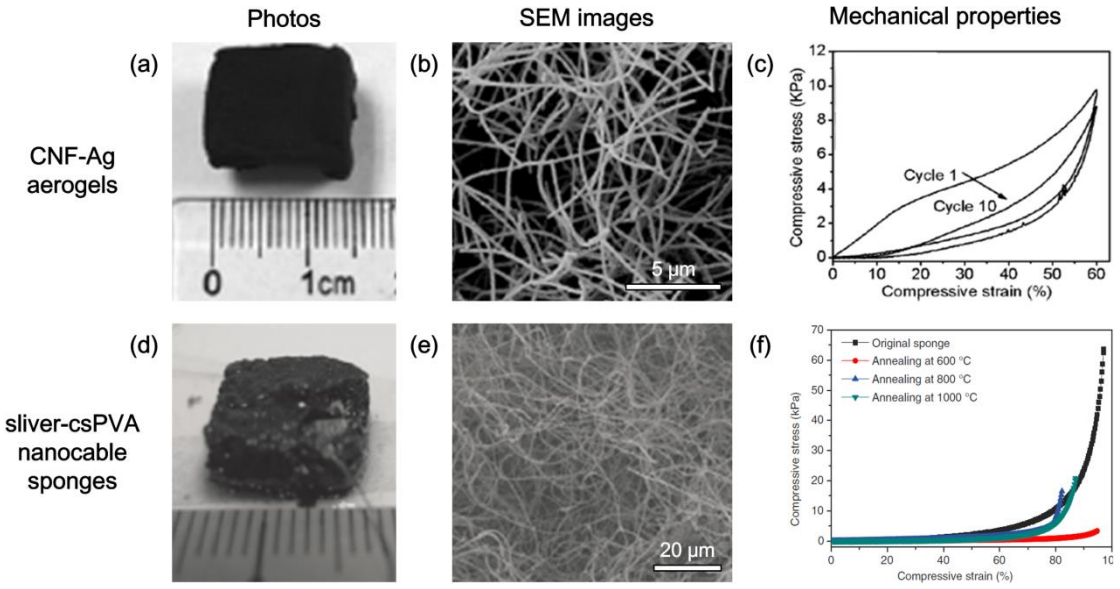

Figure 1.13 3D conductive elastomers constructed from (a-c) AgNPs and (d-f) AgNWs. (a) A photograph and (b) an SEM image of carbonaceous nanofibers-Ag aerogels. (c) Cyclic stress–strain curves of carbonaceous nanofibers-Ag aerogel at a set strain of 60%. (© 2012 WILEY-VCH Verlag GmbH & Co. KGaA)[8] (d) A photograph and (e) an SEM image of silver-carbon nanocable sponge-PDMS nanocomposite. (f) Compressive curves of original silver-csPVA nanocable sponge and sliver-carbon nanocable/CNT sponges prepared at different annealing temperatures. (© 2011 WILEY-VCH Verlag GmbH & Co. KGaA)[20]

Self-supported 3D elastic conductors also receive great attention in the development of future technology, owing to its high porosity, large specific area, low density, and excellent electrical and mechanical properties. By far, carbon materials, such as CNTs[160] and graphene,[132] have been demonstrated as promising candidates for electrical conductive elastomers. Meanwhile, metallic nanostructures are also regarded as potential alternatives; besides the excellent conductivity, incorporation of metals might bring in more attractive characristics, including optical and catalytic performances.

In the year of 2012, Liang et al. fabricated mechanically robust macroscopic scale (up to 12 L) carbonaceous nanofiber hydrogels and aerogels through template-directed hydrothermal carbonization process.[8] They further employed the aerogels as 3D scaffolds to produce carbonaceous nanofibers-AgNP aerogels via in situ reduction of $AgNO_3$ (Figure 1.13 (a-c)). The growth of AgNPs did not destroy the highly porous structures or reduce the mechanical strength; meanwhile, the electrical conductivity was greatly enhanced. AgNWs were also employed as templates to generate 3D sponge-like elastic conductors.[20] In 2011, Yao et al. constructed silver-crosslinked PVA hybrid networks via hydrothermal synthesis (Figure 1.13 (d-f)). After deliberately designed carbonization treatment, elastomeric conductors with high electrical conductivity, excellent durability at cyclic load, and great repeatability of resistance variation during deformation were obtained. Moreover, the electrical and mechanical behaviors were tunable according to the carbonization temperature and time.

However, to improve the mechanical strength without any negative influence on the electrical conductivity, most strategies for metallic NP-based elastic conductors involved high temperature treatment (> 600 ℃) under the protection of inert gas. The process undoubtedly adds the cost and complicates the operation. Therefore, low-cost, energy-saving, and environmentally friendly method is still under urgent demands.

1.5 Thesis Objectives

The objective of this thesis is to design novel functional nano-metallic electrodes using meta-atoms from the "artificial periodic table" (Figure 1.3) by low-cost "bottom-up" approach and further explore their applications in electrocatalysis and flexible electronics. AuNPs with different sizes and shapes are to be assembled into electrocatalytic electrodes, and CuNWs are to be developed into flexible electrodes. To reach the milestones, a number of challenges had to be overcome:

Synthesis of building blocks

All the building blocks are to be synthesized via wet chemical approaches, since it can generate well-defined metallic NPs under mild conditions. To obtain an accurate conclusion on the size/shape-dependent electrocatalytic analysis, highly stable AuNPs with spherical and rod-like morphologies are to be synthesized via seed-mediated method. Long and thin CuNWs in a large-scale are to be prepared via chemical reduction approaches as the building blocks for self-supported 3D aerogels.

Assembly of the building blocks into functional electrodes

To investigate the size-and shape-dependent electrocatalytic performance of AuNPs, a robust and stable fabrication strategy is to be developed, where the NPs have to be uniformly deposited on the substrate via chemical linking interactions. To improve the mechanical flexibility of the electrocatalytic electrodes, commercially available tissue papers are to be utilized as the substrates. AuNPs are to be packed closely on the surface via drop-casting methods, which will guarantee the conductivity of the electrodes. For CuNW-based flexible electronics, self-supported CuNW monoliths are to be fabricated via low-cost and eco-friendly freeze-casting approach, which will serve as the conductive network. The mechanical strength of the CuNW aerogels is to be improved by a trace amount of polymer additive, and further polymer embedding will also enhance the strength as well as prevent the CuNWs from oxidation.

Translation of the electrodes into devices

To develop CuNWs based electrodes into piezo-resistivity switches, the relation between compressive strains and electrical resistance is to be investigated systematically. Then, the aerogels are to be sandwiched between two conductive glass slides which are connected with a liquid emitting diode (LED) lamp. The variation of brightness of the lamp will tell the compressive forces on the CuNWs based electrodes.

1.6 References

1. Jana, N. R.; Gearheart, L.; Murphy, C. J., Seeding Growth for Size Control of 5−40 nm Diameter Gold Nanoparticles. *Langmuir* **2001**, *17*, 6782-6786.

2. Bharathi, S.; Nogami, M.; Ikeda, S., Novel Electrochemical Interfaces with a Tunable Kinetic Barrier by Self-Assembling Organically Modified Silica Gel and Gold Nanoparticles. *Langmuir* **2000**, *17*, 1-4.

3. Kim, C.; Gu, W.; Briceno, M.; Robertson, I. M.; Choi, H.; Kim, K., Copper Nanowires with a Five-Twinned Structure Grown by Chemical Vapor Deposition. *Adv. Mater.* **2008**, *20*, 1859-1863.

4. Krebs, F. C., Fabrication and processing of polymer solar cells: A review of printing and coating techniques. *Sol. Energy Mater. Sol. Cells* **2009**, *93*, 394-412.

5. Yan, H.; Blanford, C. F.; Holland, B. T.; Parent, M.; Smyrl, W. H.; Stein, A., A Chemical Synthesis of Periodic Macroporous NiO and Metallic Ni. *Adv. Mater.* **1999**, *11*, 1003-1006.

6. Zeng, X.-Y.; Zhang, Q.-K.; Yu, R.-M.; Lu, C.-Z., A New Transparent Conductor: Silver Nanowire Film Buried at the Surface of a Transparent Polymer. *Adv. Mater.* **2010**, *22*, 4484-4488.

7. Ataee-Esfahani, H.; Wang, L.; Nemoto, Y.; Yamauchi, Y., Synthesis of Bimetallic Au@Pt Nanoparticles with Au Core and Nanostructured Pt Shell toward Highly Active Electrocatalysts. *Chem. Mater.* **2010**, *22*, 6310-6318.

8. Liang, H.-W.; Guan, Q.-F.; Chen, L.-F.; Zhu, Z.; Zhang, W.-J.; Yu, S.-H., Macroscopic-Scale Template Synthesis of Robust Carbonaceous Nanofiber Hydrogels and Aerogels and Their Applications. *Angew. Chem. Int. Ed.* **2012**, *51*, 5101-5105.

9. Xu, F.; Zhu, Y., Highly conductive and stretchable silver nanowire conductors. *Adv. Mater.* **2012**, *24*, 5117-5122.

10. Tian, Y.; Liu, H. Q.; Zhao, G. H.; Tatsuma, T., Shape-controlled electrodeposition of gold nanostructures. *J. Phys. Chem. B* **2006**, *110*, 23478-23481.

11. Schmitt, J.; Decher, G.; Dressick, W. J.; Brandow, S. L.; Geer, R. E.; Shashidhar, R.; Calvert, J. M., Metal nanoparticle/polymer superlattice films: Fabrication and control of layer structure. *Adv. Mater.* **1997**, *9*, 61-65.

12. Tan, S.; Campolongo, M.; Luo, D.; Cheng, W., Building plasmonic nanostructures with DNA. *Nat. Nanotechnol.* **2011**, *6*, 268-276.

13. El-Deab, M. S.; Okajima, T.; Ohsaka, T., Electrochemical reduction of oxygen on gold nanoparticle-electrodeposited glassy carbon electrodes. *J. Electrochem. Soc.* **2003**, *150*, A851-A857.

14. Lim, B.; Jiang, M. J.; Camargo, P. H. C.; Cho, E. C.; Tao, J.; Lu, X. M.; Zhu, Y. M.; Xia, Y. A., Pd-Pt Bimetallic Nanodendrites with High Activity for Oxygen Reduction. *Science* **2009**, *324*, 1302-1305.

15. Ng, K. C.; Udagedara, I. B.; Rukhlenko, I. D.; Chen, Y.; Tang, Y.; Premaratne, M.; Cheng, W., Free-Standing Plasmonic-Nanorod Superlattice Sheets. *ACS Nano* **2011**, *6*, 925-934.

16. Kim, Y.; Hong, J. W.; Lee, Y. W.; Kim, M.; Kim, D.; Yun, W. S.; Han, S. W., Synthesis of AuPt Heteronanostructures with Enhanced Electrocatalytic Activity toward Oxygen Reduction. *Angew. Chem. Int. Ed.* **2010**, *49*, 10197-10201.

17. Gao, T.; Meng, G.; Wang, Y.; Sun, S.; Zhang, L., Electrochemical synthesis of copper nanowires. *J. Phys.: Condens. Matter* **2002**, *14*, 355-363.

18. Nyce, G. W.; Hayes, J. R.; Hamza, A. V.; Satcher, J. H., Synthesis and Characterization of Hierarchical Porous Gold Materials. *Chem. Mater.* **2007**, *19*, 344-346.

19. Rathmell, A. R.; Wiley, B. J., The Synthesis and Coating of Long, Thin Copper Nanowires to Make Flexible, Transparent Conducting Films on Plastic Substrates. *Adv. Mater.* **2011**, *23*, 4798-4803.

20. Yao, H.-B.; Huang, G.; Cui, C.-H.; Wang, X.-H.; Yu, S.-H., Macroscale Elastomeric Conductors Generated from Hydrothermally Synthesized Metal-Polymer Hybrid Nanocable Sponges. *Adv. Mater.* **2011**, *23*, 3643-3647.

21. Ge, J.; Yao, H.-B.; Wang, X.; Ye, Y.-D.; Wang, J.-L.; Wu, Z.-Y.; Liu, J.-W.; Fan, F.-J.; Gao, H.-L.; Zhang, C.-L., *et al.*, Stretchable Conductors Based on Silver Nanowires: Improved Performance through a Binary Network Design. *Angew. Chem. Int. Ed.* **2013**, *125*, 1698-1703.

22. Wang, L.; Yamauchi, Y., Autoprogrammed Synthesis of Triple-Layered Au@Pd@Pt Core-Shell Nanoparticles Consisting of a Au@Pd Bimetallic Core and Nanoporous Pt Shell. *J. Am. Chem. Soc.* **2010**, *132*, 13636-13638.

23. Plowman, B.; Ippolito, S. J.; Bansal, V.; Sabri, Y. M.; O'Mullane, A. P.; Bhargava, S. K., Gold nanospikes formed through a simple electrochemical route with high electrocatalytic and surface enhanced Raman scattering activity. *Chem. Commun.* **2009**, 5039-5041.

24. Yen, M. Y.; Chiu, C. W.; Hsia, C. H.; Chen, F. R.; Kai, J. J.; Lee, C. Y.; Chiu, H. T., Synthesis of Cable-Like Copper Nanowires. *Adv. Mater.* **2003**, *15*, 235-237.

25. Millstone, J. E.; Metraux, G. S.; Mirkin, C. A., Controlling the edge length of gold nanoprisms via a seed-mediated approach. *Adv. Funct. Mater.* **2006**, *16*, 1209-1214.

26. Bigall, N.; Herrmann, A.-K.; Vogel, M.; Rose, M.; Simon, P.; Carrillo-Cabrera, W.; Dorfs, D.; Kaskel, S.; Gaponik, N.; Eychmüller, A., Hydrogels and aerogels from noble metal nanoparticles. *Angew. Chem. Int. Ed.* **2009**, *48*, 9731-9734.

27. Jena, B. K.; Raj, C. R., Synthesis of Flower-like Gold Nanoparticles and Their Electrocatalytic Activity Towards the Oxidation of Methanol and the Reduction of Oxygen. *Langmuir* **2007**, *23*, 4064-4070.

28. Kim, Y.; Zhu, J.; Yeom, B.; Di Prima, M.; Su, X.; Kim, J.-G.; Yoo, S.; Uher, C.; Kotov, N., Stretchable nanoparticle conductors with self-organized conductive pathways. *Nature* **2013**, *500*, 59-63.

29. Mohl, M.; Pusztai, P.; Kukovecz, A.; Konya, Z.; Kukkola, J.; Kordas, K.; Vajtai, R.; Ajayan, P., Low-temperature large-scale synthesis and electrical testing of ultralong copper nanowires. *Langmuir* **2010**, *26*, 16496-16502.

30. Nicholas, L.; Naveen, C.; Chariklia, S.-L.; Arif, M., Smelting in the age of nano: iron aerogels. *J. Mater. Chem.* **2009**, *19*, 63-65.

31. Niu, W.; Zheng, S.; Wang, D.; Liu, X.; Li, H.; Han, S.; Chen, J.; Tang, Z.; Xu, G., Selective synthesis of single-crystalline rhombic dodecahedral, octahedral, and cubic gold nanocrystals. *J. Am. Chem. Soc.* **2009**, *131*, 697-703.

32. Chang, Y.; Lye, M. L.; Zeng, H. C., Large-Scale Synthesis of High-Quality Ultralong Copper Nanowires. *Langmuir* **2005**, *21*, 3746-3748.

33. Tappan, B.; Huynh, M.; Hiskey, M.; Chavez, D.; Luther, E.; Mang, J.; Son, S., Ultralow-density nanostructured metal foams: combustion synthesis, morphology, and composition. *J. Am. Chem. Soc.* **2006**, *128*, 6589-6594.

34. Kumar, P. S.; Pastoriza-Santos, I.; Rodriguez-Gonzalez, B.; Garcia de Abajo, F. J.; Liz-Marzan, L. M., High-yield synthesis and optical response of gold nanostars. *Nanotechnology* **2008**, *19*, 015606.

35. Jin, M.; He, G.; Zhang, H.; Zeng, J.; Xie, Z.; Xia, Y., Shape-controlled synthesis of copper nanocrystals in an aqueous solution with glucose as a reducing agent and hexadecylamine as a capping agent. *Angew. Chem. Int. Ed.* **2011**, *50*, 10560-10564.

36. Sun, Y.; Xia, Y., Mechanistic Study on the Replacement Reaction between Silver Nanostructures and Chloroauric Acid in Aqueous Medium. *J. Am. Chem. Soc.* **2004**, *126*, 3892-3901.

37. Zhang, Q.; Uchaker, E.; Candelaria, S.; Cao, G., Nanomaterials for energy conversion and storage. *Chem. Soc. Rev.* **2013**, *42*, 3127-3171.

38. Sau, T.; Rogach, A.; Jäckel, F.; Klar, T.; Feldmann, J., Properties and applications of colloidal nonspherical noble metal nanoparticles. *Adv. Mater.* **2010**, *22*, 1805-1825.

39. Joshi, R.; Schneider, J., Assembly of one dimensional inorganic nanostructures into functional 2D and 3D architectures. Synthesis, arrangement and functionality. *Chem. Soc. Rev.* **2012**, *41*, 5285-5312.

40. Chen, A.; Holt-Hindle, P., Platinum-based nanostructured materials: synthesis, properties, and applications. *Chem. Rev.* **2010**, *110*, 3767-3804.

41. Solla-Gullón, J.; Vidal-Iglesias, F. J.; Feliu, J. M., Shape dependent electrocatalysis. *Annu. Rep. Prog. Chem., Sect. C: Phys. Chem.* **2011**, *107*, 263-297.

42. Tappan, B.; Steiner, S.; Luther, E., Nanoporous metal foams. *Angew. Chem. Int. Ed.* **2010**, *49*, 4544-4565.

43. Wang, J., Nanomaterial-based electrochemical biosensors. *Analyst* **2005**, *130*, 421-426.

44. Arvizo, R.; Bhattacharyya, S.; Kudgus, R.; Giri, K.; Bhattacharya, R.; Mukherjee, P., Intrinsic therapeutic applications of noble metal nanoparticles: past, present and future. *Chem. Soc. Rev.* **2012**, *41*, 2943-2970.

45. Carvalhal, R. F.; Sanches Freire, R.; Kubota, L. T., Polycrystalline Gold Electrodes: A Comparative Study of Pretreatment Procedures Used for Cleaning and Thiol Self-Assembly Monolayer Formation. *Electroanalysis* **2005**, *17*, 1251-1259.

46. Yang, Z.; Gonzalez-Cortes, A.; Jourquin, G.; Viré, J.-C.; Kauffmann, J.-M.; Delplancke, J.-L., Analytical application of self assembled monolayers on gold

electrodes: critical importance of surface pretreatment. *Biosens. Bioelectron.* **1995**, *10*, 789-795.

47. Guo, L.-H.; Facci, J. S.; McLendon, G.; Mosher, R., Effect of Gold Topography and Surface Pretreatment on the Self-Assembly of Alkanethiol Monolayers. *Langmuir* **1994**, *10*, 4588-4593.

48. Clavilier, J.; Faure, R.; Guinet, G.; Durand, R., Preparation of monocrystalline Pt microelectrodes and electrochemical study of the plane surfaces cut in the direction of the {111} and {110} planes. *J. Electroanal. Chem.* **1979**, *107*, 205-209.

49. Hamelin, A.; Doubova, L.; Wagner, D.; Schirmer, H., A modification of the last step of surface preparation for gold and silver single crystal faces. *J. Electroanal. Chem.* **1987**, *220*, 155-160.

50. Hourani, M.; Wieckowski, A., Electrochemistry of the ordered Rh (111) electrode: Surface preparation and voltammetry in HClO4 Electrolyte. *J. Electroanal. Chem.* **1987**, *227*, 259-264.

51. Solomun, T., Initial stages of electrooxidation of Pd (100) surfaces in sulfuric acid solution: An XPS study. *J. Electroanal. Chem.* **1987**, *217*, 435-441.

52. Voigtländer, B.; Linke, U.; Stollwerk, H.; Brona, J., Preparation of bead metal single crystals by electron beam heating. *J. Vac. Sci. Technol., A* **2005**, *23*, 1535-1537.

53. Hara, M.; Linke, U.; Wandlowski, T., Preparation and electrochemical characterization of palladium single crystal electrodes in 0.1 M H2SO4 and HClO4: Part I. Low-index phases. *Electrochim. Acta* **2007**, *52*, 5733-5748.

54. Ellmer, K., Past achievements and future challenges in the development of optically transparent electrodes. *Nature Photon.* **2012**, *6*, 809-817.

55. Zen, J.-M.; Chung, M.-J., Square-wave voltammetric stripping analysis of mercury(II) at a poly(4-vinylpyridine)/gold film electrode. *Anal. Chem.* **1995**, *67*, 3571-3577.

56. Lee, M.-S.; Hong, S.-C.; Kim, D., Fabrication of patterned gold electrodes with spin-coated-and-fired Au(1 1 1) film by the soft lithography. *Appl. Surf. Sci.* **2006**, *252*, 5019-5025.

57. Hendrik, S.; Jan, H. S.; Martin, T.; Alexey, P.; Michael, I.; Horst, W.; Tobias, V., Freestanding films of crosslinked gold nanoparticles prepared via layer-by-layer spin-coating. *Nanotechnology* **2011**, *22*, 305303.

58. Rauch, T.; Boberl, M.; Tedde, S. F.; Furst, J.; Kovalenko, M. V.; Hesser, G.; Lemmer, U.; Heiss, W.; Hayden, O., Near-infrared imaging with quantum-dot-sensitized organic photodiodes. *Nature Photon.* **2009**, *3*, 332-336.

59. Bodnarchuk, M. I.; Kovalenko, M. V.; Pichler, S.; Fritz-Popovski, G.; Hesser, G.; Heiss, W., Large-Area Ordered Superlattices from Magnetic Wüstite/Cobalt Ferrite Core/Shell Nanocrystals by Doctor Blade Casting. *ACS Nano* **2009**, *4*, 423-431.

60. Li, M.; Li, Y.-T.; Li, D.-W.; Long, Y.-T., Recent developments and applications of screen-printed electrodes in environmental assays—A review. *Anal. Chim. Acta.* **2012**, *734*, 31-44.

61. Bain, C. D.; Troughton, E. B.; Tao, Y. T.; Evall, J.; Whitesides, G. M.; Nuzzo, R. G., Formation of monolayer films by the spontaneous assembly of organic thiols from solution onto gold. *J. Am. Chem. Soc.* **1989**, *111*, 321-335.

62. Loaiza, Ó. A.; Campuzano, S.; Pedrero, M.; Pingaron, J. M., Designs of Enterobacteriaceae Lac Z Gene DNA Gold Screen Printed Biosensors. *Electroanalysis* **2008**, *20*, 1397-1405.

63. Gamerith, S.; Klug, A.; Scheiber, H.; Scherf, U.; Moderegger, E.; List, E. J. W., Direct Ink-Jet Printing of Ag–Cu Nanoparticle and Ag-Precursor Based Electrodes for OFET Applications. *Adv. Funct. Mater.* **2007**, *17*, 3111-3118.

64. Kim, D.; Jeong, S.; Shin, H.; Xia, Y.; Moon, J., Heterogeneous Interfacial Properties of Ink-Jet-Printed Silver Nanoparticulate Electrode and Organic Semiconductor. *Adv. Mater.* **2008**, *20*, 3084-3089.

65. Millstone, J.; Wei, W.; Jones, M.; Yoo, H.; Mirkin, C., Iodide ions control seed-mediated growth of anisotropic gold nanoparticles. *Nano Lett.* **2008**, *8*, 2526-2529.

66. Samuel, E. L.; Nathan, D. B.; Leonardo, S.; Luis, M. L.-M.; Catherine, J. M., Anisotropic Noble Metal Nanocrystal Growth: The Role of Halides. *Chem. Mater.* **2013**.

67. Dreaden, E. C.; Alkilany, A. M.; Huang, X.; Murphy, C. J.; El-Sayed, M. A., The golden age: gold nanoparticles for biomedicine. *Chem. Soc. Rev.* **2012**, *41*, 2740-2779.

68. Eustis, S.; El-Sayed, M. A., Why gold nanoparticles are more precious than pretty gold: Noble metal surface plasmon resonance and its enhancement of the radiative and nonradiative properties of nanocrystals of different shapes. *Chem. Soc. Rev.* **2006**, *35*, 209-217.

69. Grzelczak, M.; Pérez-Juste, J.; Mulvaney, P.; Liz-Marzán, L., Shape control in gold nanoparticle synthesis. *Chem. Soc. Rev.* **2008**, *37*, 1783-1791.

70. Yonezawa, T.; Yasui, K.; Kimizuka, N., Controlled Formation of Smaller Gold Nanoparticles by the Use of Four-Chained Disulfide Stabilizer. *Langmuir* **2000**, *17*, 271-273.

71. Teranishi, T.; Kiyokawa, I.; Miyake, M., Synthesis of Monodisperse Gold Nanoparticles Using Linear Polymers as Protective Agents. *Adv. Mater.* **1998**, *10*, 596-599.

72. Zhao, M.; Sun, L.; Crooks, R. M., Preparation of Cu Nanoclusters within Dendrimer Templates. *J. Am. Chem. Soc.* **1998**, *120*, 4877-4878.

73. Hostetler, M. J.; Wingate, J. E.; Zhong, C.-J.; Harris, J. E.; Vachet, R. W.; Clark, M. R.; Londono, J. D.; Green, S. J.; Stokes, J. J.; Wignall, G. D., *et al.*, Alkanethiolate Gold Cluster Molecules with Core Diameters from 1.5 to 5.2 nm: Core and Monolayer Properties as a Function of Core Size. *Langmuir* **1998**, *14*, 17-30.

74. Jain, P. K.; Huang, X.; El-Sayed, I. H.; El-Sayed, M. A., Noble Metals on the Nanoscale: Optical and Photothermal Properties and Some Applications in Imaging, Sensing, Biology, and Medicine. *Acc. Chem. Res.* **2008**, *41*, 1578-1586.

75. Lohse, S. E.; Murphy, C. J., The Quest for Shape Control: A History of Gold Nanorod Synthesis. *Chem. Mater.* **2013**, *25*, 1250-1261.

76. Murphy, C. J.; Gole, A. M.; Hunyadi, S. E.; Orendorff, C. J., One-Dimensional Colloidal Gold and Silver Nanostructures. *Inorg. Chem.* **2006**, *45*, 7544-7554.

77. Burda, C.; Chen, X.; Narayanan, R.; El-Sayed, M. A., Chemistry and Properties of Nanocrystals of Different Shapes. *Chem. Rev.* **2005**, *105*, 1025-1102.

78. C. Hulteen, J.; Martin, C. R., A general template-based method for the preparation of nanomaterials. *J. Mater. Chem.* **1997**, *7*, 1075-1087.

79. Xia, Y.; Xiong, Y.; Lim, B.; Skrabalak, S., Shape-controlled synthesis of metal nanocrystals: simple chemistry meets complex physics? *Angew. Chem. Int. Ed.* **2009**, *48*, 60-103.

80. Shankar, S. S.; Rai, A.; Ankamwar, B.; Singh, A.; Ahmad, A.; Sastry, M., Biological synthesis of triangular gold nanoprisms. *Nature Mater.* **2004**, *3*, 482-488.

81. Tang, Y.; Ng, K. C.; Chen, Y.; Cheng, W., Lightweight, flexible, nanorod electrode with high electrocatalytic activity. *Electrochem. Commun.* **2013**, *27*, 120-123.

82. Sau, T. K.; Murphy, C. J., Room Temperature, High-Yield Synthesis of Multiple Shapes of Gold Nanoparticles in Aqueous Solution. *J. Am. Chem. Soc.* **2004**, *126*, 8648-8649.

83. Millstone, J. E.; Park, S.; Shuford, K. L.; Qin, L. D.; Schatz, G. C.; Mirkin, C. A., Observation of a quadrupole plasmon mode for a colloidal solution of gold nanoprisms. *J. Am. Chem. Soc.* **2005**, *127*, 5312-5313.

84. Gao, J.; Bender, C. M.; Murphy, C. J., Dependence of the Gold Nanorod Aspect Ratio on the Nature of the Directing Surfactant in Aqueous Solution. *Langmuir* **2003**, *19*, 9065-9070.

85. Smith, D. K.; Korgel, B. A., The Importance of the CTAB Surfactant on the Colloidal Seed-Mediated Synthesis of Gold Nanorods. *Langmuir* **2008**, *24*, 644-649.

86. Ha, T. H.; Koo, H.-J.; Chung, B. H., Shape-Controlled Syntheses of Gold Nanoprisms and Nanorods Influenced by Specific Adsorption of Halide Ions. *J. Phys. Chem. C* **2006**, *111*, 1123-1130.

87. Rai, A.; Singh, A.; Ahmad, A.; Sastry, M., Role of Halide Ions and Temperature on the Morphology of Biologically Synthesized Gold Nanotriangles. *Langmuir* **2005**, *22*, 736-741.

88. Sheng, J. J.; Li, J. F.; Yin, B. S.; Ren, B.; Tian, Z. Q., A preliminary study on surface-enhanced Raman scattering from Au and Au@Pd nanocubes for electrochemical applications. *Can. J. Anal. Sci. Spect.* **2007**, *52*, 178-185.

89. Kim, F.; Connor, S.; Song, H.; Kuykendall, T.; Yang, P., Platonic Gold Nanocrystals. *Angew. Chem. Int. Ed.* **2004**, *43*, 3673-3677.

90. Li, C.; Shuford, K. L.; Park, Q. H.; Cai, W.; Li, Y.; Lee, E. J.; Cho, S. O., High-Yield Synthesis of Single-Crystalline Gold Nano-octahedra. *Angew. Chem. Int. Ed.* **2007**, *46*, 3264-3268.

91. Wang, J.; Gong, J.; Xiong, Y.; Yang, J.; Gao, Y.; Liu, Y.; Lu, X.; Tang, Z., Shape-dependent electrocatalytic activity of monodispersed gold nanocrystals toward glucose oxidation. *Chem. Commun.* **2011**, *47*, 6894-6896.

92. Hao, E.; Bailey, R. C.; Schatz, G. C.; Hupp, J. T.; Li, S., Synthesis and Optical Properties of "Branched" Gold Nanocrystals. *Nano Lett.* **2004**, *4*, 327-330.

93. Liz-Marzán, L. M., Tailoring Surface Plasmons through the Morphology and Assembly of Metal Nanoparticles. *Langmuir* **2005**, *22*, 32-41.

94. Chen, S.; Wang, Z. L.; Ballato, J.; Foulger, S. H.; Carroll, D. L., Monopod, Bipod, Tripod, and Tetrapod Gold Nanocrystals. *J. Am. Chem. Soc.* **2003**, *125*, 16186-16187.

95. Nehl, C. L.; Liao, H.; Hafner, J. H., Optical Properties of Star-Shaped Gold Nanoparticles. *Nano Lett.* **2006**, *6*, 683-688.

96. Khoury, C. G.; Vo-Dinh, T., Gold Nanostars For Surface-Enhanced Raman Scattering: Synthesis, Characterization and Optimization. *J. Phys. Chem. C* **2008**, *112*, 18849-18859.

97. Liao, H. G.; Jiang, Y. X.; Zhou, Z. Y.; Chen, S. P.; Sun, S. G., Shape-Controlled Synthesis of Gold Nanoparticles in Deep Eutectic Solvents for Studies of Structure-Functionality Relationships in Electrocatalysis. *Angew. Chem. Int. Ed.* **2008**, *47*, 9100-9103.

98. Mahmoud, A. M.; Daniel, O. N.; Mostafa, A. E.-S., Hollow and Solid Metallic Nanoparticles in Sensing and in Nanocatalysis. *Chem. Mater.* **2013**. DOI: 10.1021/cm4020892.

99. Caruso, F.; Caruso, R. A.; Möhwald, H., Nanoengineering of Inorganic and Hybrid Hollow Spheres by Colloidal Templating. *Science* **1998**, *282*, 1111-1114.

100. Yin, Y.; Rioux, R. M.; Erdonmez, C. K.; Hughes, S.; Somorjai, G. A.; Alivisatos, A. P., Formation of Hollow Nanocrystals Through the Nanoscale Kirkendall Effect. *Science* **2004**, *304*, 711-714.

101. Sun, Y.; Xia, Y., Shape-controlled synthesis of gold and silver nanoparticles. (Reports). *Science* **2002**, *298*, 2176-2179.

102. Mahmoud, M. A.; Saira, F.; El-Sayed, M. A., Experimental Evidence For The Nanocage Effect In Catalysis With Hollow Nanoparticles. *Nano Lett.* **2010**, *10*, 3764-3769.

103. Mahmoud, M. A.; El-Sayed, M. A., Time Dependence and Signs of the Shift of the Surface Plasmon Resonance Frequency in Nanocages Elucidate the Nanocatalysis Mechanism in Hollow Nanoparticles. *Nano Lett.* **2011**, *11*, 946-953.

104. Wang, C.; Hwang, D.; Yu, Z.; Takei, K.; Park, J.; Chen, T.; Ma, B.; Javey, A., User-interactive electronic skin for instantaneous pressure visualization. *Nature Mater.* **2013**, *12*, 899-904.

105. Yang, C.; Gu, H.; Lin, W.; Yuen, M.; Wong, C.; Xiong, M.; Gao, B., Silver nanowires: from scalable synthesis to recyclable foldable electronics. *Adv. Mater.* **2011**, *23*, 3052-3056.

106. Jo, S. H.; Tu, Y.; Huang, Z. P.; Carnahan, D. L.; Huang, J. Y.; Wang, D. Z.; Ren, Z. F., Correlation of field emission and surface microstructure of vertically aligned carbon nanotubes. *Appl. Phys. Lett.* **2004**, *84*, 413-415.

107. Liu, Z.; Bando, Y., A Novel Method for Preparing Copper Nanorods and Nanowires. *Adv. Mater.* **2003**, *15*, 303-305.

108. Murphy, C. J.; Sau, T. K.; Gole, A.; Orendorff, C. J., Surfactant-Directed Synthesis and Optical Properties of One-Dimensional Plasmonic Metallic Nanostructures. *MRS Bull.* **2005**, *30*, 349-355.

109. Wiley, B.; Sun, Y.; Xia, Y., Synthesis of Silver Nanostructures with Controlled Shapes and Properties. *Acc. Chem. Res.* **2007**, *40*, 1067-1076.

110. Feng, H.; Yang, Y.; You, Y.; Li, G.; Guo, J.; Yu, T.; Shen, Z.; Wu, T.; Xing, B., Simple and rapid synthesis of ultrathin gold nanowires, their self-assembly and application in surface-enhanced Raman scattering. *Chem. Commun.* **2009**, 1984-1986.

111. Tian, M.; Wang, J.; Kurtz, J.; Mallouk, T. E.; Chan, M. H. W., Electrochemical Growth of Single-Crystal Metal Nanowires via a Two-Dimensional Nucleation and Growth Mechanism. *Nano Lett.* **2003**, *3*, 919-923.

112. Choi, H.; Park, S.-H., Seedless growth of free-standing copper nanowires by chemical vapor deposition. *J. Am. Chem. Soc.* **2004**, *126*, 6248-6249.

113. Toimil Molares, M. E.; Höhberger, E. M.; Schaeflein, C.; Blick, R. H.; Neumann, R.; Trautmann, C., Electrical characterization of electrochemically grown single copper nanowires. *Appl. Phys. Lett.* **2003**, *82*, 2139-2141.

114. Martin, C., Nanomaterials: a membrane-based synthetic approach. *Science* **1994**, *266*, 1961-1966.

115. Monson, C. F.; Woolley, A. T., DNA-Templated Construction of Copper Nanowires. *Nano Lett.* **2003**, *3*, 359-363.

116. Liu, Z.; Yang, Y.; Liang, J.; Hu, Z.; Li, S.; Peng, S.; Qian, Y., Synthesis of Copper Nanowires via a Complex-Surfactant-Assisted Hydrothermal Reduction Process. *J. Phys. Chem. B* **2003**, *107*, 12658-12661.

117. Zhang, X.; Zhang, D.; Ni, X.; Zheng, H., One-step preparation of copper nanorods with rectangular cross sections. *Solid State Commun.* **2006**, *139*, 412-414.

118. Wang, W.; Li, G.; Zhang, Z., A facile templateless, surfactantless hydrothermal route to ultralong copper submicron wires. *J. Cryst. Growth* **2007**, *299*, 158-164.

119. Feldheim, D. L.; Grabar, K. C.; Natan, M. J.; Mallouk, T. E., Electron transfer in self-assembled inorganic polyelectrolyte/metal nanoparticle heterostructures. *J. Am. Chem. Soc.* **1996**, *118*, 7640-7641.

120. Decher, G., Fuzzy nanoassemblies: Toward layered polymeric multicomposites. *Science* **1997**, *277*, 1232-1237.

121. Guo, S.; Wang, E., Synthesis and electrochemical applications of gold nanoparticles. *Anal. Chim. Acta.* **2007**, *598*, 181-192.

122. Glogowski, E.; Tangirala, R.; He, J. B.; Russell, T. P.; Emrick, T., Microcapsules of PEGylated gold nanoparticles prepared by fluid-fluid interfacial assembly. *Nano Lett* **2007**, *7*, 389-393.

123. Granot, E.; Katz, E.; Basnar, B.; Willner, I., Enhanced bioelectrocatalysis using Au-nanoparticle/polyaniline hybrid systems in thin films and microstructured rods assembled on electrodes. *Chem. Mater.* **2005**, *17*, 4600-4609.

124. Wang, Z.-L.; Xu, D.; Xu, J.-J.; Zhang, X.-B., Oxygen electrocatalysts in metal-air batteries: from aqueous to nonaqueous electrolytes. *Chem. Soc. Rev.* **2013**. DOI: 10.1039/C3CS60248F

125. Hamelin, A.; Martins, A. M., Cyclic voltammetry at gold single-crystal surfaces .2. Behaviour of high-index faces. *J. Electroanal. Chem.* **1996**, *407*, 13-21.

126. Hamelin, A., Cyclic voltammetry at gold single-crystal surfaces .1. Behaviour at low-index faces. *J. Electroanal. Chem.* **1996**, *407*, 1-11.

127. Rahim, M. A. A.; Hameed, R. M. A.; Khalil, M. W., The role of a bimetallic catalyst in enhancing the electro-catalytic activity towards methanol oxidation. *J. Power Sources* **2004**, *135*, 42-51.

128. Rolison, D. R.; Long, J. W.; Lytle, J. C.; Fischer, A. E.; Rhodes, C. P.; McEvoy, T. M.; Bourg, M. E.; Lubers, A. M., Multifunctional 3D nanoarchitectures for energy storage and conversion. *Chem. Soc. Rev.* **2009**, *38*, 226-252.

129. Kang, B.; Ceder, G., Battery materials for ultrafast charging and discharging. *Nature* **2009**, *458*, 190-193.

130. Tillotson, T. M.; Hrubesh, L. W., Transparent ultralow-density silica aerogels prepared by a two-step sol-gel process. *J. Non-Cryst. Solids* **1992**, *145*, 44-50.

131. Reibold, R. A.; Poco, J. F.; Baumann, T. F.; Simpson, R. L.; Satcher Jr, J. H., Synthesis and characterization of a low-density urania (UO3) aerogel. *J. Non-Cryst. Solids* **2003**, *319*, 241-246.

132. Qiu, L.; Liu, J. Z.; Chang, S. L. Y.; Wu, Y.; Li, D., Biomimetic superelastic graphene-based cellular monoliths. *Nat. Commun.* **2012**, *3*, 1241.

133. Pekala, R. W.; Alviso, C. T.; Kong, F. M.; Hulsey, S. S., Aerogels derived from multifunctional organic monomers. *J. Non-Cryst. Solids* **1992**, *145*, 90-98.

134. Jiang, P.; Cizeron, J.; Bertone, J. F.; Colvin, V. L., Preparation of Macroporous Metal Films from Colloidal Crystals. *J. Am. Chem. Soc.* **1999**, *121*, 7957-7958.

135. Erlebacher, J., An Atomistic Description of Dealloying: Porosity Evolution, the Critical Potential, and Rate-Limiting Behavior. *J. Electrochem. Soc.* **2004**, *151*, C614-C626.

136. Ding, Y.; Erlebacher, J., Nanoporous Metals with Controlled Multimodal Pore Size Distribution. *J. Am. Chem. Soc.* **2003**, *125*, 7772-7773.

137. Erlebacher, J.; Aziz, M. J.; Karma, A.; Dimitrov, N.; Sieradzki, K., Evolution of nanoporosity in dealloying. *Nature* **2001**, *410*, 450-453.

138. Mohanan, J. L.; Arachchige, I. U.; Brock, S. L., Porous semiconductor chalcogenide aerogels. *Science* **2005**, *307*, 397-400.

139. Leventis, N.; Chandrasekaran, N.; Sadekar, A.; Sotiriou-Leventis, C.; Lu, H., One-pot synthesis of interpenetrating inorganic/organic networks of CuO/resorcinol-formaldehyde aerogels: nanostructured energetic materials. *J. Am. Chem. Soc.* **2009**, *131*, 4576-4577.

140. Varma, A.; Rogachev, A. S.; Mukasyan, A. S.; Hwang, S., Combustion Synthesis of Advanced Materials: Principles and Applications. In *Advances in Chemical Engineering*, James, W., Ed. Academic Press: 1998; Vol. Volume 24, pp 79-226.

141. Erri, P.; Nader, J.; Varma, A., Controlling Combustion Wave Propagation for Transition Metal/Alloy/Cermet Foam Synthesis. *Adv. Mater.* **2008**, *20*, 1243-1245.

142. Emily, M. H.; Michelle, L. P.; Jouet, R. J., Combustion synthesis of metallic foams from nanocomposite reactants. *Intermetallics* **2006**, *14*, 620-629.

143. Argun, A. A.; Cirpan, A.; Reynolds, J. R., The First Truly All-Polymer Electrochromic Devices. *Adv. Mater.* **2003**, *15*, 1338-1341.

144. Hecht, D. S.; Hu, L.; Irvin, G., Emerging Transparent Electrodes Based on Thin Films of Carbon Nanotubes, Graphene, and Metallic Nanostructures. *Adv. Mater.* **2011**, *23*, 1482-1513.

145. Hammock, M. L.; Chortos, A.; Tee, B. C.; Tok, J. B.; Bao, Z., 25th Anniversary Article: The Evolution of Electronic Skin (E-Skin): A Brief History, Design

Considerations, and Recent Progress. *Adv. Mater.* **2013**. DOI: 10.1002/adma.201302240.

146. Jung, Y. C.; Shimamoto, D.; Muramatsu, H.; Kim, Y. A.; Hayashi, T.; Terrones, M.; Endo, M., Robust, Conducting, and Transparent Polymer Composites Using Surface-Modified and Individualized Double-Walled Carbon Nanotubes. *Adv. Mater.* **2008**, *20*, 4509-4512.

147. Kim, K.; Zhao, Y.; Jang, H.; Lee, S.; Kim, J.; Kim, K.; Ahn, J.-H.; Kim, P.; Choi, J.-Y.; Hong, B., Large-scale pattern growth of graphene films for stretchable transparent electrodes. *Nature* **2009**, *457*, 706-710.

148. Kang, M.-G.; Kim, M.-S.; Kim, J.; Guo, L. J., Organic Solar Cells Using Nanoimprinted Transparent Metal Electrodes. *Adv. Mater.* **2008**, *20*, 4408-4413.

149. De, S.; Higgins, T.; Lyons, P.; Doherty, E.; Nirmalraj, P.; Blau, W.; Boland, J.; Coleman, J., Silver Nanowire Networks as Flexible, Transparent, Conducting Films: Extremely High DC to Optical Conductivity Ratios. *ACS Nano* **2009**, *3*, 1767-1774.

150. Azulai, D.; Belenkova, T.; Gilon, H.; Barkay, Z.; Markovich, G., Transparent Metal Nanowire Thin Films Prepared in Mesostructured Templates. *Nano Lett.* **2009**, *9*, 4246-4249.

151. Rogers, J.; Someya, T.; Huang, Y., Materials and mechanics for stretchable electronics. *Science* **2010**, *327*, 1603-1607.

152. Fan, Z.; Ho, J. C.; Takahashi, T.; Yerushalmi, R.; Takei, K.; Ford, A. C.; Chueh, Y.-L.; Javey, A., Toward the Development of Printable Nanowire Electronics and Sensors. *Adv. Mater.* **2009**, *21*, 3730-3743.

153. Floreano, D.; Urzelai, J., Evolutionary robots with on-line self-organization and behavioral fitness. *Neural Networks* **2000**, *13*, 431-443.

154. Bowden, N.; Brittain, S.; Evans, A. G.; Hutchinson, J. W.; Whitesides, G. M., Spontaneous formation of ordered structures in thin films of metals supported on an elastomeric polymer. *Nature* **1998**, *393*, 146-149.

155. Gray, D. S.; Tien, J.; Chen, C. S., High-Conductivity Elastomeric Electronics. *Adv. Mater.* **2004**, *16*, 393-397.

156. Someya, T.; Kato, Y.; Sekitani, T.; Iba, S.; Noguchi, Y.; Murase, Y.; Kawaguchi, H.; Sakurai, T., Conformable, flexible, large-area networks of pressure and thermal sensors with organic transistor active matrixes. *Proc. Natl. Acad. Sci. U.S.A.* **2005**, *102*, 12321-12325.

157. Sekitani, T.; Noguchi, Y.; Hata, K.; Fukushima, T.; Aida, T.; Someya, T., A Rubberlike Stretchable Active Matrix Using Elastic Conductors. *Science* **2008**, *321*, 1468-1472.

158. Hu, L.; Yuan, W.; Brochu, P.; Gruner, G.; Pei, Q., Highly stretchable, conductive, and transparent nanotube thin films. *Appl. Phys. Lett.* **2009**, *94*, 161108.

159. Zhu, Y.; Xu, F., Buckling of Aligned Carbon Nanotubes as Stretchable Conductors: A New Manufacturing Strategy. *Adv. Mater.* **2012**, *24*, 1073-1077.

160. Yan, Y. H.; Eugene, M. T., Tailoring the Electrical Properties of Carbon Nanotube-Polymer Composites. *Adv. Funct. Mater.* **2010**, *20*, 4062-4068.

This page is intentionally blank

Chapter Two

Synthesis of Building Blocks

In this chapter, the synthetic protocols of building blocks are presented, along with the morphology (and optical) characterization.

2.1 Chemicals and Materials

All chemicals listed in Table 2.1 are used as received. Ultrapure water (18.2 MΩ cm), purified using a Barnstead NANOpure Water Purification System (received from K. I. Scientific Pty. Ltd., North Ryde, NSW, Australia), was used for all experiments. Silicon and silica-coated silicon wafers with <100> orientation were purchased from University Wafer (Boston, MA, USA). TEM grids were ordered from Ted Pella Inc. (Redding, CA, USA) Disposal cuvettes (1939) were obtained from Kartell Labware division (Australia).

Table 2.1 The Chemicals Used for Building Block Synthesis

Chemical Names and/or molecular formula	Purity	Supplier
Copper (II) nitrate pentahemihydrate ($Cu(NO_3)_2 \cdot 2.5H_2O$)	⩾98%	Sigma-Aldrich
Ethylenediamine (EDA)	BioXtra	Sigma-Aldrich
Gold (III) chloride trihydrate ($HAuCl_4$)	⩾99.9%	Sigma-Aldrich
Hexadecyltrimethylammonium bromide (CTAB)	⩾98%	Sigma-Aldrich
Hydrazine solution (N_2H_4)	35 wt.% in H_2O	Sigma-Aldrich
L-ascorbic acid (L-AA)	99%	Sigma-Aldrich
Polyvinylpyrrolidone (M_w=10,000) (PVP)	N/A	Sigma-Aldrich
Potassium iodide	99.5%	Merck
Silver nitrate ($AgNO_3$)	99.8-100.5%	Merck
Sodium borohydride ($NaBH_4$)	⩾98%	Sigma-Aldrich
Sodium citrate	⩾98%	Sigma-Aldrich
Sodium hydroxide (NaOH)	⩾99.5%	Merck

2.2 Instrumentals

2.2.1 General

An Eppendorf 5430 centrifuge (received from Eppendorf South Pacific Pty. Ltd., North Ryde, NSW, Australia) was used for centrifugation. Sonication cleaning was performed using a Branson B5500T-DTH sonic bath at frequency of 42 $\pm$ 2.5 kHz. A Julabo water bath (TW8) (obtained from John Morris Scientific Pty Ltd, Melbourne, Australia) was employed for gold nanorod (AuNR) growth. An IKA® RCT basic (from) was used for growing copper nanowires (CuNWs).

2.2.2. Ultraviolet-visible (UV-vis) Spectroscopy

Absorption spectra of gold nanoparticles (AuNPs) were recorded using an Agilent 8453 UV-Vis spectrophotometer in the range of 300-1100 nm. For liquid samples, the measurements were conducted in a 3 ml volume quartz cuvette with a 10 mm light path.

2.2.3. Transmission Electron Microscopy (TEM)

TEM images were taken by using a Philips CM20 electron microscope with a LaB6 gun working at 200 kV, located at Monash University Centre for Electronic Microscopy (MCEM). For TEM sample preparation, one drop of AuNP solution was placed on a carboncoated copper grid (Holey support films, 400 mesh copper grids) and left to dry at room temperature. The samples were then stored in a vacuum chamber.

2.2.4. Scanning Electron Microscopy (SEM)

Scanning electron microscope micrographs were taken using a field emission JEOL 7001F SEM, located at MCEM. The JEOL700F operates with a Schottky-type field emission gun (FEG) with a maximum electron probe of > 200 nA. Samples without metal sputter coating were directly adhered onto the sample holder using conductive carbon tape from ProSciTech. All SEM images were taken with 5 kV acceleration voltage in a vacuum less than 2×10^{-4} Pa, a working distance of 5 mm and the probe current set to the arbitrary number 8 (medium sized probe).

2.3 Building Block Synthesis

In this part, experimental protocols and purification procedures of metallic nanoparticle (NP) building blocks, including gold nanospheres with the diameter of 20 nm (AuNS20s), gold gold nanospheres with the diameter of 45 nm (AuNS45s), AuNRs, and CuNWs, were described.

2.3.1 Gold nanospheres

2.3.1.1. Gold Nanospheres with the Diameter of 20 nm (AuNS20s)

AuNS20s were synthesized via a multi-stepped seed-mediated growth approach.[1] In the first step, 0.6 mL ice-cold, freshly prepared 0.1 M $NaBH_4$ was quickly added into a 20 mL aqueous solution containing 2.5×10^{-4} M $HAuCl_4$ and 2.5×10^{-4} M sodium citrate. Right after the addition of $NaBH_4$, the solution color turned from light yellow to orange-red, indicating the generation of small-sized gold seeds. The gold seeds were further aged for 2-5 hours before use. At the same time, growth solution containing 2.5×10^{-4} M $HAuCl_4$ and 0.08 M CTAB was prepared. In the second step, 0.05 mL freshly prepared 0.1 M L-AA solution were gently dropped into 7.5 mL growth solution, which

changed the color from yellow to colorless, a signal showing the reduction of Au^{3+} to Au^{0}. Then, 2.5 mL gold seed solution was added into the colorless solution. Within 10 min of stirring at 800 rpm, AuNSs with a diameter of 5.5 ± 0.6 nm were produced. In the third step, 1.0 ml of the 5.5 nm AuNS solution was injected into the mixture of 9 mL growth solution and 0.05 mL 0.1 M L-AA solution; after 10 min of stirring at 800 rpm, AuNSs with the diameter of 8.0 ± 0.8 nm were produced. In the last step, 1.0 ml 8.0 nm AuNS solution was added into the combination of 9 mL growth solution and 0.05 mL 0.1 M L-AA solution, and AuNS20s were finally produced.

The purification of AuNS20s was completed by centrifugation for two rounds. In the first round, AuNS20 aqueous solution was centrifuged at 14,000 rpm for 10 min, and the precipitation was re-dispersed in ultrapure water. In the second round, the centrifugation speed was reduced to 12,000 rpm to keep AuNPs from aggregation. AuNS20s were ready for further electrode modification after re-dispersion.

2.3.1.2. Gold Nanospheres with the Diameter of 45 nm (AuNS45s)

AuNS45s were prepared from another multi-stepped seed-mediated growth approach.[2] The synthetical procedures were illustrated in Scheme 2.1.

In the first step, gold seeds which were identical to those used for preparing AuNS20s were synthesized (For details, please refer to *Part 1* of Section 2.3.1). Meanwhile, growth solution containing 3 mL 10 mM $HAuCl_4$, 108 mL 0.05 M CTAB solution with 50 μM KI, 0.6 mL 0.1 M L-AA, and 0.6 mL 0.1 M NaOH was prepared and then divided into three parts: 9.35 mL for growth solution 1 (GS1), 9.35 mL for growth solution 2 (GS2), and the left for growth solution 3 (GS3). In the second step, 1 mL seed solution was added into GS1 and followed by a gentle shaking for approximate 1.5 s, turning the color from colorless (growth solution) to violet (solution A). In the third step, 1 mL solution A was quickly injected into GS2, along with 1.5 seconds of strong shaking. A color change from colorless to pink indicated the generation of solution B. In the third step, all of the solution B was poured into GS3. The growth of AuNS45s

completed in 30 min under the stirring at 1,000 rpm, and the color of the final product was dark purple.

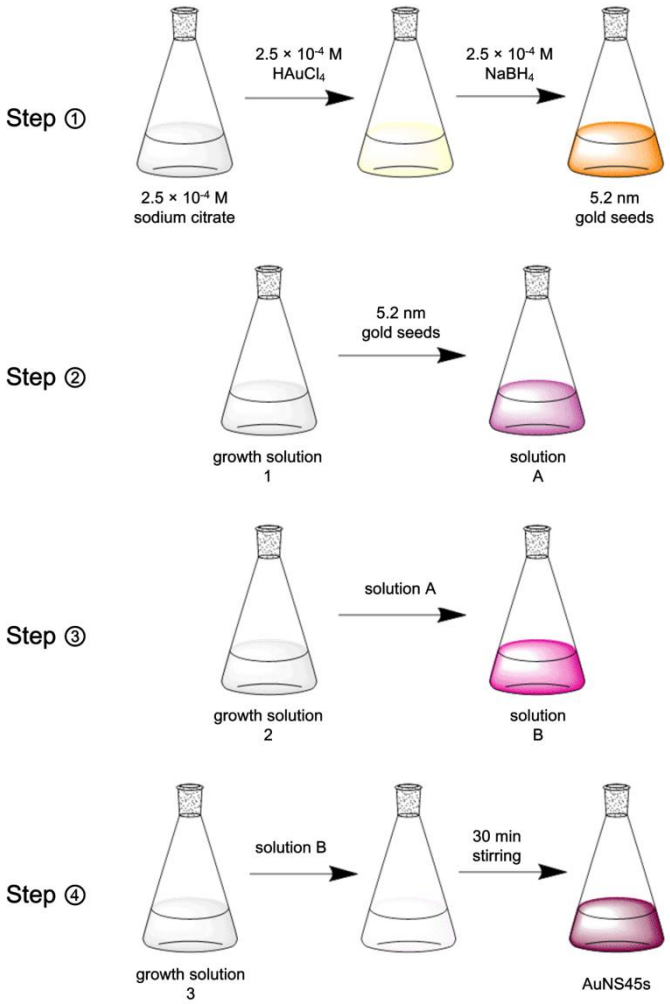

Scheme 2.1 Synthetical process of AuNS45s.

Since the final product consisted of both AuNS45s and gold nanoprisms with the edge around 100 nm, an overnight staying in 30 ℃ water bath was employed to precipitate larger particles. Then, the supernatant was purified by three times of centrifugation at the speed of 10,000 rpm for 10 min.

2.3.2 Gold nanorods (AuNRs)

AuNRs were synthesized by following previously reported seed-mediated growth method.[3] Firstly, gold seeds were synthesized by injecting 0.60 mL ice-cold 0.010 M $NaBH_4$ into the mixture of 5.0 mL 0.20 M CTAB and 5.0 mL of 0.50 mM $HAuCl_4$ solutions. After vigorous stirring for 2 min, seed solution with brown color was generated. The gold seeds needed to be aged at 25 ℃ for about 1 hour before use. Secondly, growth solution containing 200 μL 4.0 mM $AgNO_3$, 5.0 mL 0.20 M CTAB, 5.0 mL 1.0 mM $HAuCl_4$, and 70 μL 0.0788 M L-AA were prepared and stored in a 30 ℃ water bath to keep CTAB from re-crystallization. Finally, 12 μL of seed solution was quichly injected into the growth solution, after one slight inversion and 2 hours of growing in 30 ℃ water bath, AuNRs were obtained.

For electrode modification, AuNRs needed to be purified and concentrated by three rounds of centrifugation. In the first round, AuNRs were centrifuged at 12,000 for 12 mins. In the second round, to avoid the aggregation of AuNRs, the speed was reduced to 10,000. In the last round, a further reduction down to 9,000 was performed. After re-dispersed in ultrapure water, AuNRs were ready for electrode modification.

2.3.3. Copper nanowires (CuNWs)

NaOH (20 mL, 15 M), $Cu(NO_3)_2$ (1 mL, 0.1 M), EDA (0.15 mL), and N_2H_4 (0.025 mL, 35 wt% in water) were mixed in sequence in a 50 mL round bottom flask. Then, the flask was put in a paraffin oil bath and heated to 80 ˚C along with stirring at 200 rpm. After the color of the mixture turned from translucent light blue in transparent colorless, the solution was transferred into a 50 ml centrifuge tube immersed in an ice bath, and then 5 ml PVP (0.4 wt%) aqueous solution was dropped to the top of the reaction solution gently. After 1 hour of growing in the ice bath, CuNWs floated on the top of the reaction solution, forming a cake-like porous shape.

Before the purification by centrifugation, the CuNW-cake was scooped from the top of the reaction solution and re-dispersed in the aqueous washing solution (WS1)

containing N_2H_4 (3 wt%) and PVP (1 wt%). PVP was employed to improve the dispersion of CuNWs, and N_2H_4 (3 wt%) was utilized to keep CuNWs from oxidation. The mixture was centrifuged at 2,000 rpm for 5 minutes, and the precipitated CuNWs were then re-dispersed in new WS1 by strong shaking on a vortex at 3,000 rpm for 30 seconds. The purification process was repeated by three times to eliminate redundant reaction agents, such as NaOH and EDA. To remove the excess PVP, CuNW precipitations were further re-dispersed in the washing solution containing only N_2H_4 (3 wt%) (WS2) and centrifuged at 2,000 rpm for 5 minutes for three times. Finally, after three times of purification by ultrapure water via centrifugation at 2,000 rpm for 5 minutes, CuNW aqueous solution was ready to be used as building blocks.

2.4 Characterizations of Building Blocks

2.4.1 Gold Nanospheres

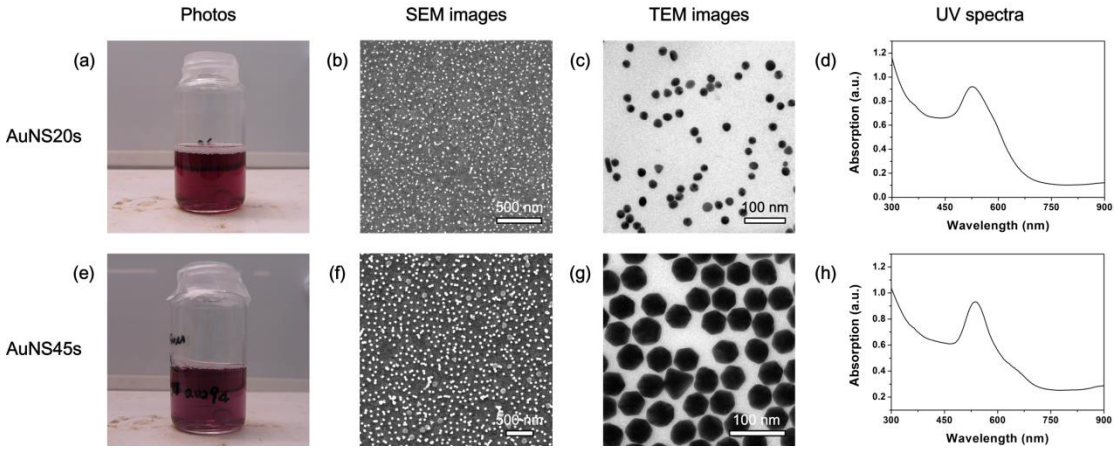

Figure 2.1 Morphology and optical characterizations of (a-d) AuNS20s and (e-h) AuNS45s. (a) A photo, (b) an SEM image, (c) an TEM image, and (d) UV spectrum of AuNS20s. (e) A photo, (f) an SEM image, (g) an TEM image, and (h) UV spectrum of AuNS45s.

The color of AuNS20s right after preparation is transparent purple, which indicates the good dispersion of the gold colloids (Figure 2.1 (a)). The SEM image shown in Figure

2.1 (b) proves the high yield and narrow size distribution of AuNS20s; most of the AuNPs exhibit a sphere-like shape with similar diameters, and few rod-like nanostructures exist. The mono-dispersion of AuNS20s benefits from the multi-stepped seed-mediated growth method, which effectively inhibits the secondary nucleation during the growth stage.[1] The TEM image (Figure 2.1 (c)) further confirms the uniform size distribution of AuNS20s; the diameter of these AuNPs are in a range of 20 ± 2.5 nm, with a standard deviation around 10%. The absorption peak position locates at around 528 nm, and a shoulder (~585 nm) is observed mainly caused by the existence of rod-like AuNPs (Figure 2.1 (d)).

In comparison with the color of AuNS20s, the one of AuNS45s is darker (Figure 2.1 (e)), which indicates a larger diameter. Moreover, both of the SEM image and TEM image (Figure 2.1 (f and g)) show that the size distribution of AuNS45s is narrow; only less than 10% of the AuNPs exhibit a plate-like shape. An obvious UV-absorption peak at 537 nm also confirms the mono-dispersion of AuNS45s (Figure 2.1 (f)). The small shoulder around 900 nm is in accordance with presence of the gold nanoplates.

2.4.2 Gold nanorods

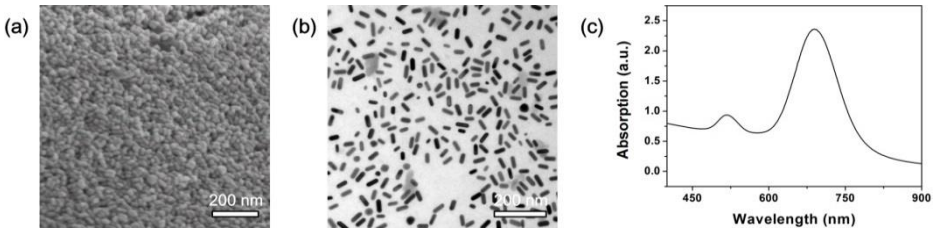

Figure 2.2 Morphology and optical characterizations of AuNRs. (a) An SEM image, (b) an TEM image, and (c) UV spectrum of AuNRs.

AuNRs with high yield and narrow size distribution are synthesized via seed-mediated growth method (Figure 2.2 (a)).[3] Notice the aspect ratio of AuNRs is highly dependent on the additional amount of $AgNO_3$, based on the TEM image (Figure 2.2 (b)), the AuNRs we synthesized possessed an average length at ~ 60 nm and an average diameter at ~ 23 nm, with an aspect ratio less than 3.0. The two absorption peaks in the UV spectrum indicates the transverse and longitudinal plasmon, respectively (Figure

2.2 (c)). No obvious shoulder is observed in the range from 500 to 550 nm, confirming that the presence of spherical AuNPs are neglectable.

2.4.3 Copper Nanowires (CuNWs)

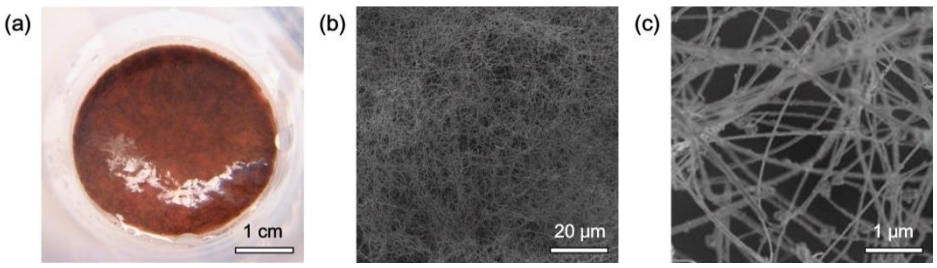

Figure 2.3 Morphology characterizations of CuNWs. (a) A photo, (b) a low resolution SEM image, and (c) a high resolution SEM image of CuNWs.

As shown in Figure 2.3 (a), CuNWs right after preparation exhibit reddish-brown color, which indicates that no obvious oxidation occurred during the growth.[4] The SEM image under a low magnification (Figure 2.3 (b)) show that the aspect ratio of CuNWs are very high; with the length more than 20 μm and the diameter less than 60 nm. From a high resolution SEM image (Figure 2.3 (c)), we observe that CuNWs are terminated by sphere-like structures, which implies that the wire-like structures are developed from spherical copper seeds.[5]

2.5 References

1. Jana, N. R.; Gearheart, L.; Murphy, C. J., Seeding Growth for Size Control of 5−40 nm Diameter Gold Nanoparticles. *Langmuir* **2001**, *17*, 6782-6786.

2. Millstone, J. E.; Park, S.; Shuford, K. L.; Qin, L. D.; Schatz, G. C.; Mirkin, C. A., Observation of a quadrupole plasmon mode for a colloidal solution of gold nanoprisms. *J. Am. Chem. Soc.* **2005**, *127*, 5312-5313.

3. Nikoobakht, B.; El-Sayed, M. A., Preparation and Growth Mechanism of Gold Nanorods (NRs) Using Seed-Mediated Growth Method. *Chem. Mater.* **2003**, *15*, 1957-1962.

4. Rathmell, A. R.; Wiley, B. J., The Synthesis and Coating of Long, Thin Copper Nanowires to Make Flexible, Transparent Conducting Films on Plastic Substrates. *Adv. Mater.* **2011**, *23*, 4798-4803.

5. Rathmell, A. R.; Bergin, S. M.; Hua, Y.-L.; Li, Z.-Y.; Wiley, B. J., The Growth Mechanism of Copper Nanowires and Their Properties in Flexible, Transparent Conducting Films. *Adv. Mater.* **2010**, *22*, 3558-3563.

This page is intentionally blank

Chapter Three

Electrode Design

In this chapter, the "bottom-up" fabrication procedures of electrocatalytic electrodes and electrical conductor were described.

3.1 Chemicals and Materials

Table 3.1 The Chemicals Used for Electrode Fabrication

Chemical Names and/or molecular formula	Purity	Supplier
(3-Aminopropyl)trimethoxysilane (APTMS)	97%	Sigma-Aldrich
Poly(sodium 4-styrenesulfonate) (M_w~70,000) (PSS)	N/A	Sigma-Aldrich
Methanol (CH_4O)	GR	Merck
Ethanol (C_2H_5OH)	GR	Merck
Acetone ($(CH_3)_2CO$)	GR	Merck
Sodium chloride (NaCl)	⩾99%	Sigma-Aldrich
Polyvinyl alcohol (Mw = 85,000~124,000) (PVA)	N/A	Sigma-Aldrich
SYLGARD® 184 Silicon Elastomer Curing Agent	N/A	Dow Corning
SYLGARD® 184 Silicon Elastomer Base	N/A	Dow Corning

All chemicals listed in Table 3.1 are used as received. Ultrapure water (18.2 MΩ cm), purified using a Barnstead NANOpure Water Purification System (received from K. I. Scientific Pty. Ltd., North Ryde, NSW, Australia), was used for all experiments. Indium tin oxide (ITO) coated glass slides with the resistance of 15-20 Ω/□ were purchased from Sigma-Aldrich. Clean tissue papers were obtained from Kimberly-Clark Worldwide, Inc. Dishwashing liquid (Palmolive®) was purchased from a Coles supermarket.

3.2 Instrumentals

3.2.1 Ultraviolet-Ozone (UV-O3) Cleansing

A UV-O_3 cleanser (Model: UV-1) purchased from SAMCO Inc. was used to eliminate the superfluous ligands attached on the surface of electrodes. The oxygen flow speed was limited to 0.5 L min^{-1}.

3.2.2. Freeze-Drying

CuNW-PVA aqueous solutions were frozen by a SANYO ultra-low temperature freezer at -80 ℃, and the freeze drying process was performed on a HETO PowerDry PL6000 Freeze Dryer under a pressure of 0.002 mbar.

3.3 Electrode Design

In comparison with conventional fabrication techniques for electrodes, such as polishing, coating, and printing (for details, please refer to Chapter One); "bottom-up"

design has the following benefits. (1) The structures of building blocks are finely controllable, providing a more precise way to regulate the properties of the assemblies. (2) The operation process can be completed with few requirements of complicated, high-cost, and delicate instruments. (3) The properties of the electrodes can also be designed by the choice of substrates, such as the weight, transparency, and flexibility.

3.3.1 Electrocatalytic Electrodes

In this section, electrocatalytic electrodes are fabricated via "bottom-up" assembly. The aim is to: (1) synthesize mechanically robust electrodes to investigate the size- and shape-dependent electrocatalytic activities of gold nanoparticles (AuNPs) and (2) develop a simple yet effective approach for lightweight and flexible AuNP electrode with high electrocatalytic activity.

3.3.1.1. Nanoparticle-Modified Electrode with Size- and Shape-Dependent Electrocatalytic Activities

Development of high-performance nanoparticle electrocatalysts plays a critical role in methanol and hydrogel fuel cells.[1] Particle size,[2] shape,[3, 4] composition and structures (including crystalline features, atomic steps, kinks, and ledges)[5-8] are key factors influencing the electrocatalytic performances. To further understand fundamental nature of catalysis by novel nanomaterials, such as Au, Pt, Pd, and Pt-based alloy nano-sized metals, research efforts have been directed to investigate the effects of their morphological[9-11] and structural[12] parameters on the catalytic performances.

Wet chemical synthesis is a cost-effective route to metal nanoparticles with adjustable size, shape, and crystalline structures,[13] therefore, emerging as a viable strategy to tailor electrocatalysis with high accuracy.[6, 14-17] A prerequisite step to integrate wet chemically-synthesized nanoparticles into an electrocatalytic system is to immobilize them onto a bulk conductive electrode surface.[14, 18-20] Physical deposition such as drop-casting[14] has proven to be a simple immobilization strategy for such purposes, which unfortunately often leads to inhomogeneous deposition with severe particle aggregation.

Consequently, nanoparticle surfaces are in principle only partially accessible to fuels in electrocatalytic reactions, therefore, lower efficacy in material usage.

Indeed, a sparser and uniform deposition can be achieved by a chemical modification strategy in which nanoparticles could be chemically tethered to electrode surface with reliable control over particle number densities.[21-25] In this part, we extend such a chemical modification method to immobilize pre-synthesized AuNPs onto transparent ITO electrode surfaces to form an aggregation-free submonolayer for the investigation of size- and shape-dependent electrocatalytic performances. The building blocks are mono-dispersed 20 nm gold nanospheres (AuNS20s), 45 nm nanospheres (AuNS45s), and $20 \times 20 \times 63$ nm^3 nanorods (Au NRs). To exclude the possible effects of surface-capping ligands on electrocatalytic activity, AuNPs are all protected by the same cationic surfactant-hexadecyltrimethylammonium bromide (CTAB).

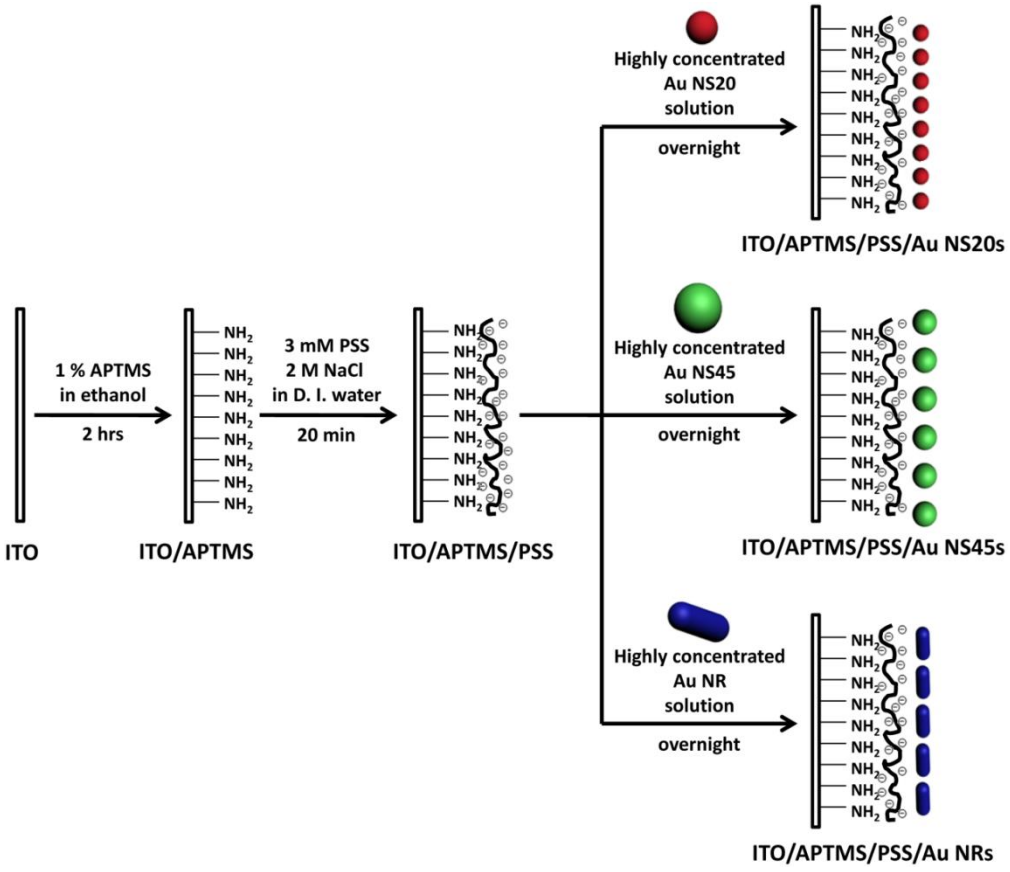

Scheme 3.1 The modification procedures of ITO/APTMS/PSS/AuNPs electrodes. In the first step, clean ITO slides are immersed in 1% APTMS ethanolic solution for 2 hours. In the second step, ITO/APTMS slides are left in the mixture of 3 mM PSS and 2 M NaCl aqueous solution for 20 min. In the last step, AuNS20s, AuNS45s, and AuNRs are modified on ITO/APTMS/PSS slides through overnight immersion.

The fabrication procedures are shown in Scheme 3.1. Before electrode modification, ITO slides are cleaned by sonication for 20 min in the following solvents in sequence: soapy water, deionized water, acetone, and methanol. Then, the ITO glass slides are dried by N_2 and left in a clean petri dish before use. In the first step of electrode fabrication, ITO electrodes are left in 1% APTMS ethanolic solution (V:V) for more than 12 hours, and positively charged amino groups are attached on the surface of the electrodes via hydrolysis. In the second step, ITO/APTMS slides are immersed in 3 mM PSS aqueous solution in the presence of 2 M NaCl. Through electrostatic interaction between the amino groups and negatively charged PSS, ITO/APTMS/PSS electrodes with negative charges exposed on the surface are obtained. In the third step, CTAB capped, positively charged AuNPs are modified on the surface of ITO/APTMS/PSS electrodes again with the help of electrostatic interaction. The ITO/APTMS/PSS electrodes are normally immersed in concentrated AuNP solutions overnight for a maximum attachment of the NPs. For reliable and stable electrochemical measuring results, the AuNPs modified electrodes are treated by UV-O_3 cleansing for 5 min to eliminate superfluous organic ligands and polymers.

3.3.1.2. Lightweight, Flexible, Nanoparticle Electrode with High Electrocatalytic Activity

To integrate gold nanoparticles into an electrocatalytical system, it is usually a prerequisite step to immobilize them onto a bulk conductive electrode surface. Typically, drop-casting[5] and chemical self-assembly[18, 19] were the viable immobilization strategies for such purposes. Both strategies are based on the "nanoparticles-on-conductor" design. The conductors are usually the rigid materials, such as glass carbon electrode, gold electrode or transparent ITO-coated glasses. In this part, we develop a simple yet efficient drop-casting strategy to fabricate high-performance electrocatalytical electrodes from gold nanorods without requirement of a bulk current conductor.

Briefly, clean tissue papers produced by Kimberly-Clark Worldwide, Inc. are cut into sheets with the dimensions of 0.40×2.5 cm^2. Then, 40 μL highly concentrated AuNP

aqueous solution is drop-casted on the tissue paper sheets. The concentrations for AuNR and AuNS45 solutions are 50 nM and 30 nM, respectively. After drop-casting process, the wet paper sheets are dried in 50 ℃ oven for 20 to 30 min to eliminate the water. Then, another 40 μL the highly concentrated AuNP aqueous solution is deposited on the paper sheets, following by the same drying process. The drop-casting and dry process is expected to be repeated for about 10 cycles, until the sheet resistance of the modified electrodes reaches approximately 20 Ω/□.

3.3.2 Electrical Conductors

In this section, copper nanowires (CuNWs) based metallic/composite aerogels are developed as electrical conductors step by step. Firstly, ultra-light and highly electrical conductive CuNW monolith aerogels are fabricated via an economical and environmental friendly freeze-casting approach. Secondly, poly(vinyl alcohol) (PVA) is employed as fillers to construct CuNW-PVA composite aerogels with a better mechanical strength. Thirdly, the composite aerogels are further infiltrated with poly(dimethylsiloxane) (PDMS) to achieve manufacturable electrical conductive rubbers.

3.3.2.1. Copper Nanowire Monolith Aerogels

Metal aerogels are highly-porous metals with porosity of no less than 50%, which can integrate unique properties (such as high electrical and thermal conductivity) of metals and unique properties (such as low density, high surface area) of aerogel into a single material system.[26] As such, metal aerogels are a new class of advanced materials with a wide range of potential applications in sensors,[27] fuel cells,[28] catalysis,[29] membranes,[30] supercapacitors,[31] and actuators.[32] However, unlike aerogels from non-metallic silica,[33] metal oxides,[34] polymers,[35] and carbon nanotubes,[36] it is nontrivial to produce metal aerogels due to the difficulty in generating wet gels of metals. Hence, fabrication methodologies of metal aerogels do not exist until very recently.[26]

Notably, the existing metal aerogel-fabricating approaches often require unconventional experimental conditions. For example, combustion method required high temperature and pressure, oxygen-/water-free environments;[37] microfabrication approach required expensive equipment;[38] dealloying required expensive sacrificial noble metals.[39] In addition, there were few reports on mechanical and electrical properties of ultralow-density metal aerogels due to the difficulties in scaling up with these approaches.[26]

In this part, we use a freeze-casting method, under mild conditions, to produce ultralow-density copper aerogel monoliths with well-defined shapes from one-dimensional (1D) building blocks-CuNWs. Although freeze-casting (or supercritical drying with similar procedures) has been utilized to generate porous materials from ceramics,[40] silica,[33] polymer-metal nanostructure composites,[41] carbon nanotubes,[42] and graphene,[43] it has not yet been used to produce large-scale metal aerogel monoliths

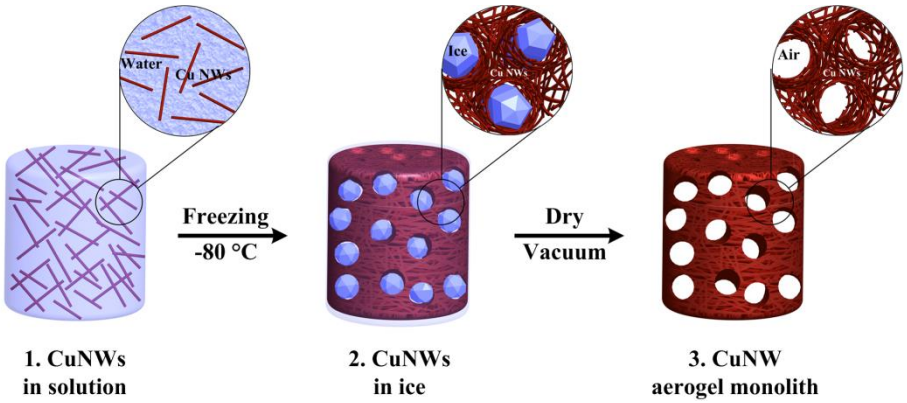

Scheme 3.2 Schematic illustration of fabricating CuNW monolith aerogels via freeze-casting approach.

The fabrication procedures are illustrated in Scheme 3.2. In the first step, highly concentrated CuNW aqueous solution is poured into a glass vial with a cylindrical shape (50 × 12 mm). In the second step, the CuNW solution is strongly shaken by a vortex device at a speed of 3,000 rpm and then left in a freezer with the temperature of -80 ℃ for at least 2 hours. This process leads to the formation of ice crystals, which acts as the templates for the production of highly porous structures. In the third step, the

frozen sample is freeze-dried at a sublimation temperature of -47.4 ℃ and a pressure of 0.002 mbar.

3.3.2.2. Copper Nanowire-PVA(-PDMS) Composites

Metallic aerogels, which combine the special characteristics of nano-sized metals and excellent properties of bulk materials, have exhibited distinctive properties, such as low relative density, high specific surface area, improved optical response, and size-effect-enhanced catalytic and magnetic activities.[26] Therefore, these porous metals are accepted as promising substitutes as the functional parts in an array of technological applications, including sensors,[27] fuel cells,[28] catalysis,[29] membranes,[30] supercapacitors,[31] and actuators.[32]

However, metallic aerogels were seldom reported to be applied as conductive elastomers,[38] a new class of materials which can maintain their excellent electrical stability and performance under different deformations, including bending,[44] stretching,[45] compressing,[41] and twisting.[46] Since the present synthetical approaches can only generate metallic aerogels either too brittle or too stiff.[26] To utilize the outstanding electrical conductivity of metallic aerogels in the functional part of an elastic conductor, the improvement of the mechanical flexibility is one of the most critical challenges.

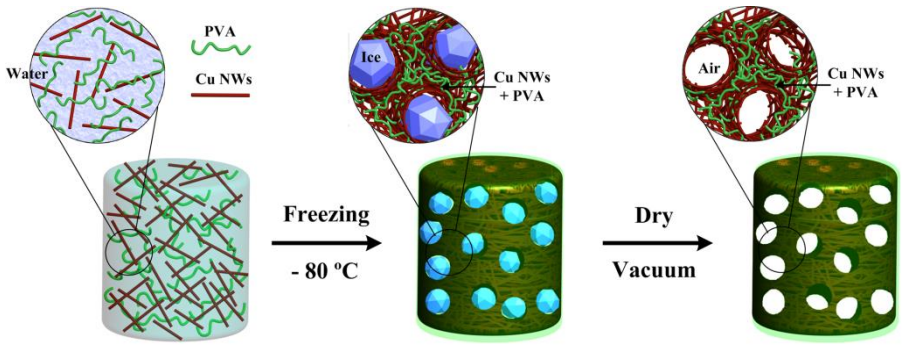

Scheme 3.3 Schematic illustration of fabricating CuNW-PVA composite aerogels via freeze-casting approach.

One of the existent strategies for metallic aerogels with elasticity was brought out by Schaedler et al.; nickel aerogels were fabricated via template-assisted approach, and they could recover to its original height after 50% compressive strain.[38] However, this approach involves complicated operation procedures, and the aerogels cannot be further manufactured into diverse morphologies for various applications.

In this part, we develop a simple yet efficient approach to produce CuNW based composite aerogels which successfully integrate the excellent electrical properties from metals and mechanical behaviors from polymers (PVA). Moreover, after PDMS encapsulation, the composite aerogels are developed as electrical conductive rubbers, which are manufacturable to satisfied various technological requirements.

The fabrication procedures of CuNW-PVA composite aerogels are described in Scheme 3.3. The process is similar to that for the preparation of CuNW monolith aerogels. In the first step, aqueous solutions containing the mixture of CuNWs and PVA are poured into a sample vial (50 × 12 mm) with cylindrical shapes. In the second step, the mixture is strongly shaken by a vortex device at a speed of 3,000 rpm and left in a freezer at -80 ℃ for 2 hours. In the third step, the frozen samples are freeze-dried at a sublimation temperature of -47.4 ℃ and a pressure of 0.002 mbar.

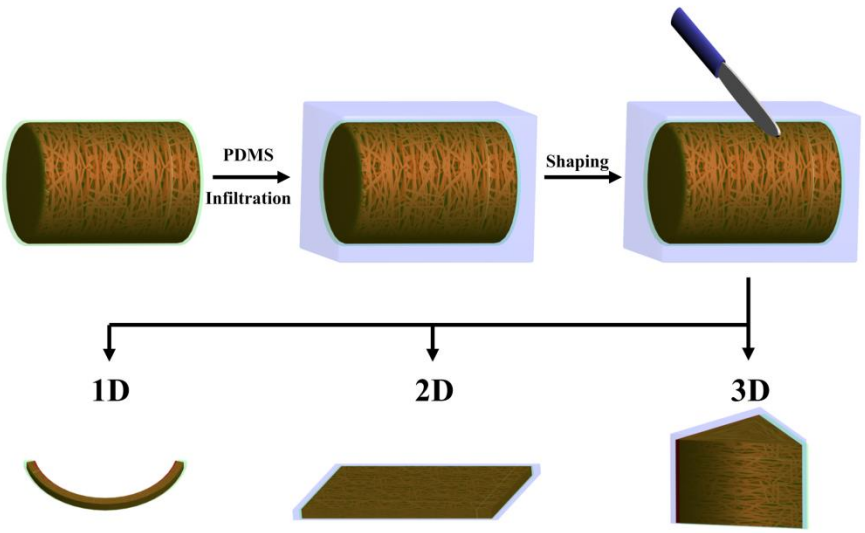

Scheme 3.4 Schematic illustration of fabricating manufacturable CuNW-PVA-PDMS composites as electrical conductive rubbers.

The fabrication process for manufacturable CuNW-PVA-PDMS composites is illustrated in Scheme 3.4. In the first step, PDMS is infiltrated into the CuNW-PVA composite aerogels. Briefly, pre-cured PDMS, the mixture of the "base" and the "curing agent" with a ratio of 10:1, is gently poured onto the as-prepared CuNW-PVA composite aerogels. Then, the composite aerogels in pre-cured PDMS is degassed in a desiccator for approximately 4 hours, until no gas bubbles are observed on the surface of the mixture. PDMS encapsulation is completed by leaving the mixture in an oven at 80 ℃ for 2 hours. In the second step, the CuNW-PVA-PDMS composites are cut into various 1D, 2D, and 3D morphologies with a blade.

3.4 Summary

In this chapter, various modification approaches via "bottom-up" assembly are described for the fabrication of electrocatalytic or electrical conductive electrodes.

For electrocatalytic applications, we aim to achieve low-cost and stable electrodes with high electrocatalytic activities. Moreover, we also focus on the investigations of the size- and shape-dependent electrocatalysis of AuNPs towards both methanol oxidation reaction and oxygen reduction reaction, two important reactions in fuel cells. In the first part, we fabricated AuNP modified ITO electrodes via electrocatalytic interactions. After the modification, AuNPs dispersed uniformly on the surface of the electrodes without any obvious aggregations or deformations. In the second part, we used light-weight, non-conductive, low-cost, and flexible tissue paper as the substrates, which greatly reduced the cost of the electrodes. AuNPs were drop-casted on the tissue paper, and the SEM images confirmed that AuNPs kept their well-defined shapes and no aggregation occurred.

For electrical conductive applications, we aim to develop advanced electrodes with low-cost and high performance. CuNWs are regarded as the ideal materials. In the first step, we developed an environmental friendly method to fabrication ultra-light weight CuNW monolith aerogel. In the second step, to improve the mechanical properties of

the monolith aerogels, a tiny amount of PVA was added during the preparation. In the third step, we further infiltrated PDMS into the CuNW-PVA composite aerogels for the achievement of manufacturable electrical conductive rubbers.

3.5 References

1. Qiao, Y.; Li, C. M., Nanostructured catalysts in fuel cells. *J. Mater. Chem.* **2011**, *21*, 4027-4036.
2. Debe, M. K., Electrocatalyst approaches and challenges for automotive fuel cells. *Nature* **2012**, *486*, 43-51.
3. Kinoshita, K., Particle Size Effects for Oxygen Reduction on Highly Dispersed Platinum in Acid Electrolytes. *J. Electrochem. Soc.* **1990**, *137*, 845-848.
4. Solla-Gullon, J.; Vidal-Iglesias, F. J.; Lopez-Cudero, A.; Garnier, E.; Feliu, J. M.; Aldaz, A., Shape-dependent electrocatalysis: methanol and formic acid electrooxidation on preferentially oriented Pt nanoparticles. *Phys. Chem. Chem. Phys.* **2008**, *10*, 3689-3698.
5. Lim, B.; Jiang, M. J.; Camargo, P. H. C.; Cho, E. C.; Tao, J.; Lu, X. M.; Zhu, Y. M.; Xia, Y. A., Pd-Pt Bimetallic Nanodendrites with High Activity for Oxygen Reduction. *Science* **2009**, *324*, 1302-1305.
6. Wang, J.; Gong, J.; Xiong, Y.; Yang, J.; Gao, Y.; Liu, Y.; Lu, X.; Tang, Z., Shape-dependent electrocatalytic activity of monodispersed gold nanocrystals toward glucose oxidation. *Chem. Commun.* **2011**, *47*, 6894-6896.
7. Erikson, H.; Jürmann, G.; Sarapuu, A.; Potter, R. J.; Tammeveski, K., Electroreduction of oxygen on carbon-supported gold catalysts. *Electrochim. Acta* **2009**, *54*, 7483-7489.
8. Yin, H.; Tang, H.; Wang, D.; Gao, Y.; Tang, Z., Facile Synthesis of Surfactant-Free Au Cluster/Graphene Hybrids for High-Performance Oxygen Reduction Reaction. *ACS Nano* **2012**, *6*, 8288-8297.
9. Chen, J.; Lim, B.; Lee, E. P.; Xia, Y., Shape-controlled synthesis of platinum nanocrystals for catalytic and electrocatalytic applications. *Nano Today* **2009**, *4*, 81-95.

10. Sánchez-Sánchez, C. M.; Solla-Gullón, J.; Vidal-Iglesias, F. J.; Aldaz, A.; Montiel, V.; Herrero, E., Imaging Structure Sensitive Catalysis on Different Shape-Controlled Platinum Nanoparticles. *J. Am. Chem. Soc.* **2010**, *132*, 5622-5624.

11. Nesselberger, M.; Ashton, S.; Meier, J. C.; Katsounaros, I.; Mayrhofer, K. J. J.; Arenz, M., The Particle Size Effect on the Oxygen Reduction Reaction Activity of Pt Catalysts: Influence of Electrolyte and Relation to Single Crystal Models. *J. Am. Chem. Soc.* **2011**, *133*, 17428-17433.

12. Huang, X.; Tang, S.; Zhang, H.; Zhou, Z.; Zheng, N., Controlled Formation of Concave Tetrahedral/Trigonal Bipyramidal Palladium Nanocrystals. *J. Am. Chem. Soc.* **2009**, *131*, 13916-13917.

13. Tan, S.; Campolongo, M.; Luo, D.; Cheng, W., Building plasmonic nanostructures with DNA. *Nat. Nanotechnol.* **2011**, *6*, 268-276.

14. Ataee-Esfahani, H.; Wang, L.; Yamauchi, Y., Block copolymer assisted synthesis of bimetallic colloids with Au core and nanodendritic Pt shell. *Chem. Commun.* **2010**, *46*, 3684-3686.

15. Yang, H., Platinum-Based Electrocatalysts with Core–Shell Nanostructures. *Angew. Chem. Int. Ed.* **2011**, *50*, 2674-2676.

16. Lim, B.; Xia, Y., Metal Nanocrystals with Highly Branched Morphologies. *Angew. Chem. Int. Ed.* **2011**, *50*, 76-85.

17. Koenigsmann, C.; Santulli, A. C.; Gong, K.; Vukmirovic, M. B.; Zhou, W.-p.; Sutter, E.; Wong, S. S.; Adzic, R. R., Enhanced Electrocatalytic Performance of Processed, Ultrathin, Supported Pd–Pt Core–Shell Nanowire Catalysts for the Oxygen Reduction Reaction. *J. Am. Chem. Soc.* **2011**, *133*, 9783-9795.

18. Ballarin, B.; Cassani, M. C.; Scavetta, E.; Tonelli, D., Self-assembled gold nanoparticles modified ITO electrodes: The monolayer binder molecule effect. *Electrochim. Acta* **2008**, *53*, 8034-8044.

19. Cheng, W.; Dong, S.; Wang, E., Site-Selective Self-assembly of MPA-Bridged CuHCF Multilayers on APTMS-Supported Gold Colloid Electrodes. *Chem. Mater.* **2003**, *15*, 2495-2501.

20. Grabar, K. C.; Smith, P. C.; Musick, M. D.; Davis, J. A.; Walter, D. G.; Jackson, M. A.; Guthrie, A. P.; Natan, M. J., Kinetic Control of Interparticle Spacing in Au Colloid-Based Surfaces: Rational Nanometer-Scale Architecture. *J. Am. Chem. Soc.* **1996**, *118*, 1148-1153.

21. Feldheim, D. L.; Grabar, K. C.; Natan, M. J.; Mallouk, T. E., Electron transfer in self-assembled inorganic polyelectrolyte/metal nanoparticle heterostructures. *J. Am. Chem. Soc.* **1996**, *118*, 7640-7641.

22. Cheng, W. L.; Dong, S. J.; Wang, E. K., Two- and three-dimensional Au nanoparticle/CoTMPyP self-assembled nanotructured materials: Film structure, tunable electrocatalytic activity, and plasmonic properties. *J. Phys. Chem. B* **2004**, *108*, 19146-19154.

23. Cheng, W. L.; Dong, S. J.; Wang, E. K., Iodine-induced gold-nanoparticle fusion/fragmentation/aggregation and iodine-linked nanostructured assemblies on a glass substrate. *Angew. Chem. Int. Ed.* **2003**, *42*, 449-452.

24. Cheng, W.; Dong, S.; Wang, E., Colloid Chemical Approach to Nanoelectrode Ensembles with Highly Controllable Active Area Fraction. *Anal. Chem.* **2002**, *74*, 3599-3604.

25. Cheng, W.; Dong, S.; Wang, E., Gold Nanoparticles as Fine Tuners of Electrochemical Properties of the Electrode/Solution Interface. *Langmuir* **2002**, *18*, 9947-9952.

26. Tappan, B.; Steiner, S.; Luther, E., Nanoporous metal foams. *Angew. Chem. Int. Ed.* **2010**, *49*, 4544-4565.

27. Gaponik, N.; Herrmann, A.-K.; Eychmüller, A., Colloidal Nanocrystal-Based Gels and Aerogels: Material Aspects and Application Perspectives. *J. Phys. Chem. Lett.* **2011**, *3*, 8-17.

28. Steele, B. C. H.; Heinzel, A., Materials for fuel-cell technologies. *Nature* **2001**, *414*, 345-352.

29. Liu, W.; Herrmann, A.-K.; Geiger, D.; Borchardt, L.; Simon, F.; Kaskel, S.; Gaponik, N.; Eychmüller, A., High-Performance Electrocatalysis on Palladium Aerogels. *Angew. Chem. Int. Ed.* **2012**, *51*, 5743-5747.

30. Pérez Padilla, A.; Rodríguez, J. A.; Saitúa, H. A., Synthesis and water ultrafiltration properties of silver membrane supported on porous ceramics. *Desalination* **1997**, *114*, 203-208.

31. Chen, Y.; Ng, K. C.; Yan, W.; Tang, Y.; Cheng, W., Ultraflexible plasmonic nanocomposite aerogel. *R. Soc. Chem. Adv.* **2011**, *1*, 1265-1270.

32. Biener, J.; Wittstock, A.; Zepeda-Ruiz, L. A.; Biener, M. M.; Zielasek, V.; Kramer, D.; Viswanath, R. N.; Weissmuller, J.; Baumer, M.; Hamza, A. V., Surface-chemistry-driven actuation in nanoporous gold. *Nature Mater.* **2009**, *8*, 47-51.

33. Tillotson, T. M.; Hrubesh, L. W., Transparent ultralow-density silica aerogels prepared by a two-step sol-gel process. *J. Non-Cryst. Solids* **1992**, *145*, 44-50.

34. Leventis, N.; Chandrasekaran, N.; Sadekar, A.; Sotiriou-Leventis, C.; Lu, H., One-pot synthesis of interpenetrating inorganic/organic networks of CuO/resorcinol-formaldehyde aerogels: nanostructured energetic materials. *J. Am. Chem. Soc.* **2009**, *131*, 4576-4577.

35. Cooper, A. I., Polymer synthesis and processing using supercritical carbon dioxide. *J. Mater. Chem.* **2000**, *10*, 207-234.

36. Zou, J.; Liu, J.; Karakoti, A. S.; Kumar, A.; Joung, D.; Li, Q.; Khondaker, S. I.; Seal, S.; Zhai, L., Ultralight Multiwalled Carbon Nanotube Aerogel. *ACS Nano* **2010**, *4*, 7293-7302.

37. Tappan, B.; Huynh, M.; Hiskey, M.; Chavez, D.; Luther, E.; Mang, J.; Son, S., Ultralow-density nanostructured metal foams: combustion synthesis, morphology, and composition. *J. Am. Chem. Soc.* **2006**, *128*, 6589-6594.

38. Schaedler, T. A.; Jacobsen, A. J.; Torrents, A.; Sorensen, A. E.; Lian, J.; Greer, J. R.; Valdevit, L.; Carter, W. B., Ultralight Metallic Microlattices. *Science* **2011**, *334*, 962-965.

39. J.R. Hayes, A. M. H., J. Biener, A.V. Hamza and K. Sieradzki, Monolithic nanoporous copper by dealloying Mn–Cu. *J. Mater. Res.* **2006**, *21*, 2611-2616.

40. Deville, S., Freeze-Casting of Porous Ceramics: A Review of Current Achievements and Issues. *Adv. Eng. Mater.* **2008**, *10*, 155-169.

41. Liang, H.-W.; Guan, Q.-F.; Chen, L.-F.; Zhu, Z.; Zhang, W.-J.; Yu, S.-H., Macroscopic-Scale Template Synthesis of Robust Carbonaceous Nanofiber Hydrogels and Aerogels and Their Applications. *Angew. Chem. Int. Ed.* **2012**, *51*, 5101-5105.

42. Worsley, M. A.; Kucheyev, S. O.; Satcher, J. J. H.; Hamza, A. V.; Baumann, T. F., Mechanically robust and electrically conductive carbon nanotube foams. *Appl. Phys. Lett.* **2009**, *94*, 073115-3.

43. Qiu, L.; Liu, J. Z.; Chang, S. L. Y.; Wu, Y.; Li, D., Biomimetic superelastic graphene-based cellular monoliths. *Nat. Commun.* **2012**, *3*, 1241.

44. Ge, J.; Yao, H.-B.; Wang, X.; Ye, Y.-D.; Wang, J.-L.; Wu, Z.-Y.; Liu, J.-W.; Fan, F.-J.; Gao, H.-L.; Zhang, C.-L., *et al.*, Stretchable Conductors Based on Silver Nanowires: Improved Performance through a Binary Network Design. *Angew. Chem. Int. Ed.* **2013**, *125*, 1698-1703.

45. Xu, F.; Zhu, Y., Highly conductive and stretchable silver nanowire conductors. *Adv. Mater.* **2012**, *24*, 5117-5122.

46. Rogers, J.; Someya, T.; Huang, Y., Materials and mechanics for stretchable electronics. *Science* **2010**, *327*, 1603-1607.

This page is intentionally blank

Chapter Four

Applications of Electrocatalytic Electrode

In this chapter, the electrocatalytic applications of gold nanoparticle-based electrodes from "bottom-up" design were demonstrated and analyzed.

4.1 Chemicals and Materials

Table 4.1 The Chemicals Used for Electrocatalytic Characterizations

Chemical Names and/or molecular formula	Purity	Supplier
Sodium phosphate monobasic dehydrate ($NaH_2PO_4 \cdot 2H_2O$)	⩾99%	Sigma-Aldrich
Sodium phosphate dibasic dodecahydrate ($Na_2HPO_4 \cdot 12H_2O$)	⩾99%	Sigma-Aldrich
Potassium hydroxide (KOH)	⩾85%	Merck
Methanol (CH_4O)	GR	Merck
Sulfuric acid	GR	Merck
Potassium chloride (KCl)	⩾85%	Merck

All chemicals listed in Table 4.1 are used as received. Ultrapure water (18.2 MΩ cm), purified using a Barnstead NANOpure Water Purification System (received from K. I. Scientific Pty. Ltd., North Ryde, NSW, Australia), was used for all experiments. The electrodes used in the electrochemical measurement, including a gold disk working

electrode, a Ag/AgCl reference electrode (in 3.5 M KCl), and a Pt wire counter electrode were purchased from CH Instruments, Inc. (Austin, USA)

4.2 Instrumentals

4.2.1. Ultraviolet-visible (UV-vis) Spectroscopy

Absorption spectra of gold nanoparticles (AuNPs) modified indium tin oxide (ITO) electrodes were recorded using an Agilent 8453 UV-Vis spectrophotometer in the range of 300-1100 nm. The measurements were conducted by directly placing the modified electrodes in the front of the sample holder for liquid cells.

4.2.2. Scanning Electron Microscopy (SEM)

SEM images were taken using a field emission JEOL 7001F scanning electron microscope, located at MCEM. The JEOL700F operates with a Schottky-type field emission gun (FEG) with a maximum electron probe of > 200 nA. Samples without metal sputter coating were directly adhered onto the sample holder using conductive carbon tape from ProSciTech. All SEM images were taken with 5 kV acceleration voltage in a vacuum less than 2×10^{-4} Pa, a working distance of 5 mm and the probe current set to the arbitrary number 8 (medium sized probe).

4.2.3. Wide Angle X-Ray Diffraction (WXRD)

WXRD patterns were obtained at room temperature on a Philips PW1140/90 diffractometer with a CuKα radiation source (40 kV, 25 mA, $\lambda = 1.54$ Å). For liquid samples, the measurement was completed by dropping highly concentrated AuNP solution on a cell of a sample holder normally made by silicon or quartz and followed by drying. For solid samples, the electrodes were directly left on the sample holders.

Generally, the scan rate is 2Theta = 1 ^{o}·min^{-1} and the scan region was between 2Theta = 30 ^{o}and 110 ^{o}.

4.2.4. Electrochemical Scanning

Electrochemical measurements were performed in a conventional three-electrode cell by using a PARSTAT 2273 advanced electrochemical system (Princeton Applied Research). An Ag/AgCl electrode (in 3.5 M KCl) and a Pt wire were employed as reference electrode and counter electrode, respectively. AuNP modified electrodes and a gold disk electrode were used as working electrodes.

4.3 Nanoparticle-Modified Electrode with Size- and Shape-Dependent Electrocatalytic Activities

Size,[1] shape,[2] composition,[3] and crystalline structures[4] of noble metal nanoparticles are the key parameters in determining their electrocatalytic performances. Here in this section, we introduce a robust chemical-tethering approach to immobilize gold nanoparticles onto transparent indium tin oxide (ITO) modified glass electrode surface to systematically investigate their size- and shape-dependent electrocatalysis towards methanol oxidation reaction (MOR) and oxygen reduction reaction (ORR). Mono-dispersed 20 nm gold nanospheres (AuNS20s), 45 nm gold nanospheres (AuNS45s) and 20 × 20 × 63 nm^3 gold nanorods (AuNRs) are synthesized, which are then chemically tethered to ITO surface forming submonolayers without any aggregation. These AuNP-modified ITO electrodes exhibit strong electrocatalytic activities towards MOR and ORR, but their mass activities are highly dependent on particle sizes and shapes. For particles with similar shapes, size determines the mass activities: smaller particle size leads to greater catalytic current density per unit mass due its greater surface-to-volume ratio (AuNS20s > AuNS45s). For particles with comparable sizes, shapes or crystalline structures govern selectivity of electrocatalytic reactions: AuNS45s exhibit a higher mass current density in MOR than that for AuNRs due to its

dominant (111) facets exposed; whereas AuNRs exhibit a higher mass current density in ORR due to its dominant (100) facets exposed.

4.3.1 Electrode Characterizations

To avoid possible effects of the surface-capping ligands on catalytic activities, we synthesize AuNPs protected by the same surface-capping ligands, namely cetyltrimethylammonium bromide (CTAB). Using the seed-mediated approaches, CTAB-capped AuNS20s, AuNS45s and AuNRs were synthesized in large quantities (For details, please refer to Chapter Two.).

4.3.1.1. Crystalline Structure Characterizations

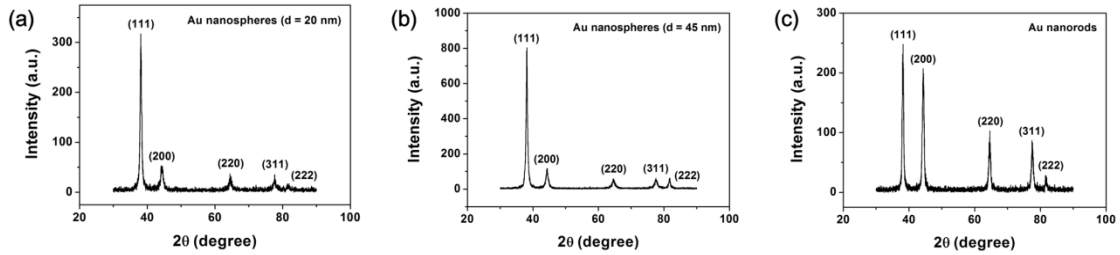

Figure 4.1 XRD patterns of (A) AuNS20s, (B) AuNS45s, and (C) AuNRs.

XRD was used to characterize the crystalline structures of the AuNPs. As shown in Figure 4.1, all the three types of NPs showed the pronounced Bragg peaks corresponding to the reflections from (111), (200), (220), (311), and (222) facets, clearly demonstrating a face-centered cubic (FCC) structure.[5] Nevertheless, relative peak intensities for these characteristic FCC planes exhibite a strong dependence on particle morphologies. The intensity ratios of (111) versus (200) planes for bulk gold, AuNS20, AuNS45 and AuNR are 3 (JCPDS), 5.89, 6.75, 1.20, respectively. This indicates that AuNS45 and AuNS20 have more dominant (111) planes than that for bulk gold; whereas, AuNRs have smallest fraction of (111) planes but with predominant (200) planes, in agreement with the previous report on the rod-shaped nanostructure.[6]

4.3.1.2. Morphology Characterizations

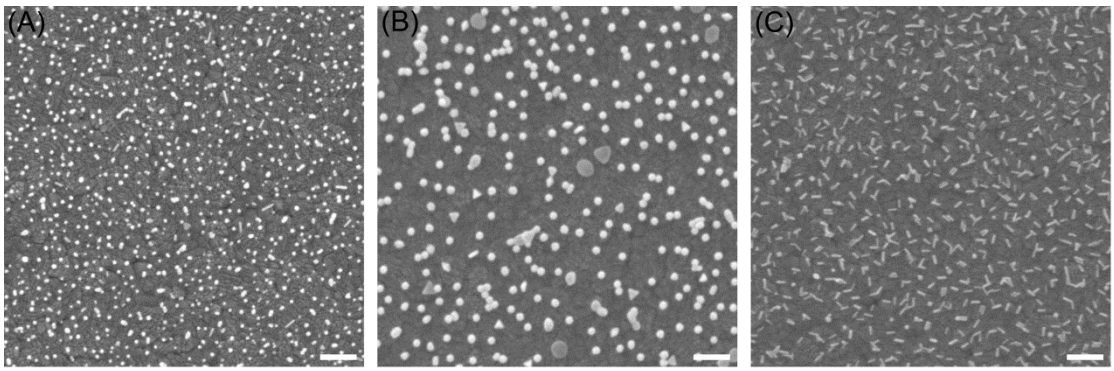

Figure 4.2 SEM images of (A) AuNS20s, (B) AuNS45s, and (C) AuNRs modified ITO electrodes. The scale bar is 200 nm.

The high conductivity of ITO electrodes enables direct morphological characterizations of AuNPs modified ITO electrodes without any additional sample processing steps by SEM. Figure 4.2 shows that AuNS20s, AuNS45s, and AuNRs are all distributed on ITO surface uniformly forming submonolayers; no evident particle aggregation or morphological transformation are observed during nanoparticle modifications or plasma treatment.

4.3.1.3. Optical Characterizations

The plasmonic properties of NP assemblies on ITO electrodes are presented in Figure 4.3. Notably, the main characteristic plasmonic peaks for AuNS20s (~527 nm), AuNS45s (~531 nm), and AuNRs (~511 nm and ~698 nm) remain before (Figure 4.3, solid lines) and after (Figure 4.3, dash lines and dot lines) their immobilization on ITO surface. Slight shifts in the characteristic peaks are observed, which might be caused by the changes of surrounding dielectric environments from water to ITO.[7, 8] There is no evident plasmonic coupling peaks observed, indicating the absence of particle aggregation in agreement with the above SEM results (Figure 4.2). Nevertheless, there are two additional shoulder peaks shown for AuNS45s. We speculate that a possible

reason is that impurities such as triangular and platelet-like particles have a stronger tendency to adsorb onto ITO than AuNS45s. Therefore, the two shoulder peaks might be due to the presence of larger fraction of impurity particles (Figure 4.3 (B)). In addition, the transverse plasmonic peak for AuNRs at ~511 nm appeared to be weaker than that in aqueous solution. This may be due to the fact that all AuNRs lied down on ITO surfaces perpendicular to incident light beam, lowering the possibility of excitation of transverse plasmonic modes. Further plasma treatment didn't lead to evident changes in plasmonic spectra (dash lines versus dot lines).

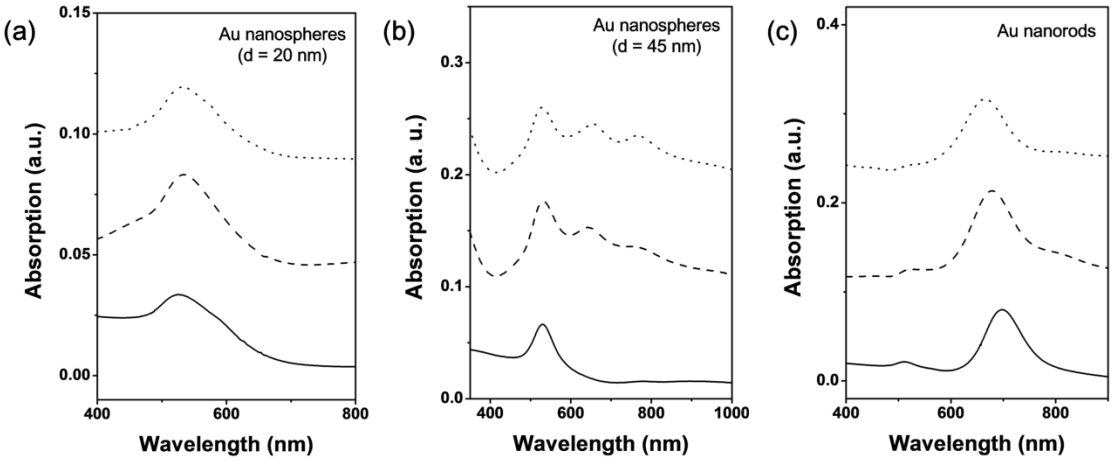

Figure 4.3 UV spectra of (A) AuNS20s, (B) AuNS45s, and (C) AuNRs dispersed in aqueous solution (solid line), after modified on ITO electrode (dash line), and after cleaned by UV-O_3 plasma (dot line).

4.3.1.4. Electrochemical Characterizations

The crystalline features of immobilized nanoparticle surfaces could be probed by electrochemical methods, such as cyclic voltammogram (CV). It has been known that CV curves for electrochemical oxidation of gold in concentrated acid solutions are characteristic of specific lattice structures, which can serve as the "finger print" of specific lattice planes.[9] In particular, formal potentials for (100) and (111) in 0.01 M aqueous H_2SO_4 were reported to be 1.3 V and 1.1 V (versus Ag/AgCl, saturated KCl), respectively.[5] For our NP-modified electrodes, the line shapes of CV curves in 0.5 M H_2SO_4 are different from AuNSs to AuNRs (Figure 4.4). For AuNS45s, a pronounced peak shows at around +1.4 V (versus Ag/AgCl, 3 M KCl), confirming the dominant

(111) facets exposed to acid solution in agreement with the XRD results (Figure 4.1 (b)). In the case of AuNRs, a clear oxidation peak shows at around 1.2 V (versus Ag/AgCl, 3 M KCl), suggesting the presence of dominant (100) facets on NR surfaces in consistence with the XRD results (Figure 4.1 (c)). As for AuNS20s, there are no characteristic CV peaks from either (111) or (100) planes. Apparently, this is against the XRD characterization (Figure 4.1 (a)) which indicates the dominance of (111) planes. However, it has to be noted that X-ray could penetrate through planes, whereas, electrochemical oxidation reactions only occurred on surfaces. It appears that CV results demonstrated that AuNS20s contain balanced (100) and (111) facets on surfaces.

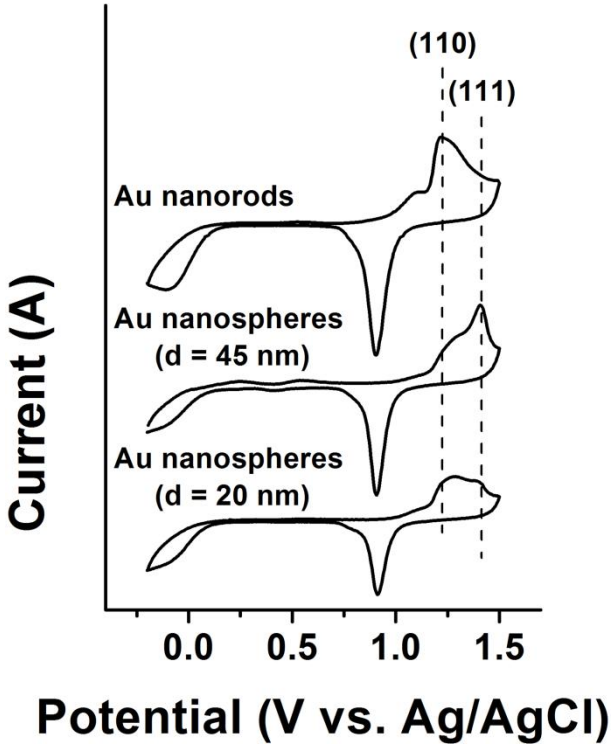

Figure 4.4 Normalized CV curves of AuNS20s, AuNS45s, and AuNRs modified ITO electrodes electrochemically scanned in 0.5 M H_2SO_4.

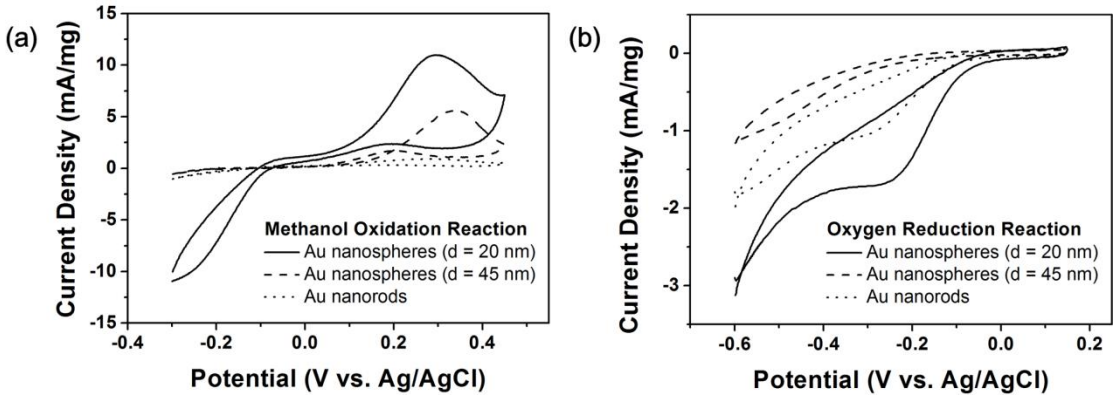

Figure 4.5 CV curves of AuNS20s (solid line), AuNS45s (dash line), and AuNRs (dot line) modified ITO electrodes electrochemically scanned in (a) 0.1 M KOH with 10 M methanol and (b) 0.1 M PBS (pH=7.2). The scan rate is 50 mV s^{-1}.

4.3.2 Electrocatalytic Behaviors

All nanoparticle-modified ITO electrodes exhibited high electrocatalytic activities towards MOR in alkaline media as well as ORR in phosphate buffered saline (PBS) buffer (Figure 4.5). Nevertheless, the catalytic mass activities were dependent on particle sizes and shapes (Tables 4.2 and 4.3).

Table 4.2 Current density of AuNP modified ITO electrodes towards MOR

	Au nanospheres (d = 20 nm)	**Au nanospheres (d = 45 nm)**	**Au nanorods ($20 \times 20 \times 60$ nm^3)**
Number Density of Au Nanoparticles (cm^{-2})	$(1.54 \pm 0.01) \times 10^{10}$	$(1.09 \pm 0.06) \times 10^{9}$	$(1.30 \pm 0.06) \times 10^{10}$
Surface-to-Volume Ratio (nm^{-1})	0.300	0.133	0.279
Mass Coverage ($mg\ cm^{-2}$)	1.25×10^{-3}	1.00×10^{-3}	4.50×10^{-3}
Peak Current Density ($mA\ mg^{-1}$)	11.00	5.59	0.91

Table 4.3 Current density of AuNP modified ITO electrodes towards ORR

	Au nanospheres (d = 20 nm)	Au nanospheres (d = 45 nm)	Au nanorods ($20 \times 20 \times 60$ nm^3)
Number Density of Au Nanoparticles (cm^{-2})	$(2.55 \pm 0.02) \times 10^{10}$	$(8.86 \pm 0.12) \times 10^{9}$	$(1.62 \pm 0.10) \times 10^{10}$
Surface-to-Volume Ratio (nm^{-1})	0.300	0.133	0.279
Mass Coverage (mg cm^{-2})	2.06×10^{-3}	8.16×10^{-3}	5.60×10^{-3}
Peak Current Density (mA mg^{-1})	-1.63	-0.87	-1.00

Moreover, as shown in Table 4.4, the peak current densities normalized by EASA of AuNP-modified electrodes were higher than the ones of BGE, indicating better electrocatalytic performances towards both ORR and MOR.

Table 4.4 Current density of AuNP modified ITO electrodes and BGE towards MOR and ORR

	Peak Current Density (mA cm^{-2}) towards MOR	Peak Current Density (mA cm^{-2}) towards ORR
Au nanospheres (d = 20 nm)	5.63	-0.60
Au nanospheres (d = 45 nm)	3.52	-0.53
Au nanorods ($20 \times 20 \times 60$ nm^3)	1.28	-0.41
BGE	0.04	-0.01

4.3.2.1. Size-Dependent Electrocatalytic Activities

We first examine size effects by comparing the mass activities of AuNS20s and AuNS45s as they are both sphere-like shapes with similar crystalline structures. As for MOR, AuNS20s give a mass activity 11 mA mg^{-1}; whereas AuNS45s give a mass activity of 5.59 mA mg^{-1}. As for ORR, AuNS20s give a mass activity of -1.63 mA mg^{-1}; whereas NS45s give a mass activity of -0.87 mA mg^{-1}. Clearly, these results demonstrate that AuNS20s exhibit better electrocatalytic activities than AuNS45s for

both MOR and ORR. Therefore, we conclude that nanoparticles with smaller size provide higher mass activity.

4.3.2.2. Shape-Dependent Electrocatalytic Activities

Next we examine shape effects by comparing mass activities of AuNS45s and AuNRs as they have comparable dimensions. For MOR (Table 4.2), AuNS45s give a mass current density of 5.59 mA mg^{-1}, which is about 6 times of that for AuNRs (only 0.91 mA mg^{-1}). However, for ORR (Table 4.3), AuNS45s exhibit a mass current density of -0.87 mA mg^{-1}, smaller than that for AuNRs (-1.00 mA mg^{-1}). Electrocatalytic selectivity of AuNS45s and AuNRs towards MOR and ORR could origin from their crystalline structures. It is known that MOR and ORR discriminate crystalline planes:[10] MOR is generally favored on (111) facets and ORR is favored on (100) facets.[5] Hence, (111) facet-dominant AuNS45s exhibit higher MOR yet lower ORR activity than (100) facet-dominant AuNRs.

4.3.2.3. Size- and Shape-Dependent Electrocatalytic Activities

Among different NPs the overall catalytic mass current densities are a combined effect of size and shapes. For MOR, both AuNS20s and AuNS45s are dominated by (111) facets, therefore their mass current densities are greater than AuNRs; whereas AuNS20s have greater surface area than AuNS45s, therefore exhibit greater electrocatalytic activities. This is proved by our experimental results that the order of mass activities is: AuNS20s > AuNS45s > AuNRs (Table 4.2). In contrast, the order of mass catalytic current densities in ORR is AuNS20s > AuNRs > AuNS45s (Table 4.3). The second part of this inequality could be well explained by the shape argument as described above. The first part of the inequality reflects the combined size and shape effects. Although AuNS20s have a smaller fraction of (100) facets exposed than that for AuNRs, they have greater surface areas. Overall, size effect overweighs shape effect, resulting in greater mass activity of AuNS20s than AuNRs.

4.3.2.4. Stability during Electrocatalytic Reactions

We also investigated the stability of the AuNPs modified electrodes during electrocatalytic reactions. After 50 cycles of MOR reactions in 0.1 M KOH, both AuNS20s and AuNS45s aggregate on ITO surfaces (Figure 4.6 (a and b)). The aggregation might be caused by the presence of (111) facets which were active in MOR. This argument is supported by the control experiments with (100)-dominant AuNRs. There are no observable NR aggregates forming after MOR reactions (Figure 4.6 (c)). In contrast, all three types of NP-modified electrodes are virtually indefinitely stable during ORR reactions. No aggregation was observed for AuNS20s, AuNS45s or AuNRs (Figure 4.6 (d-f)).

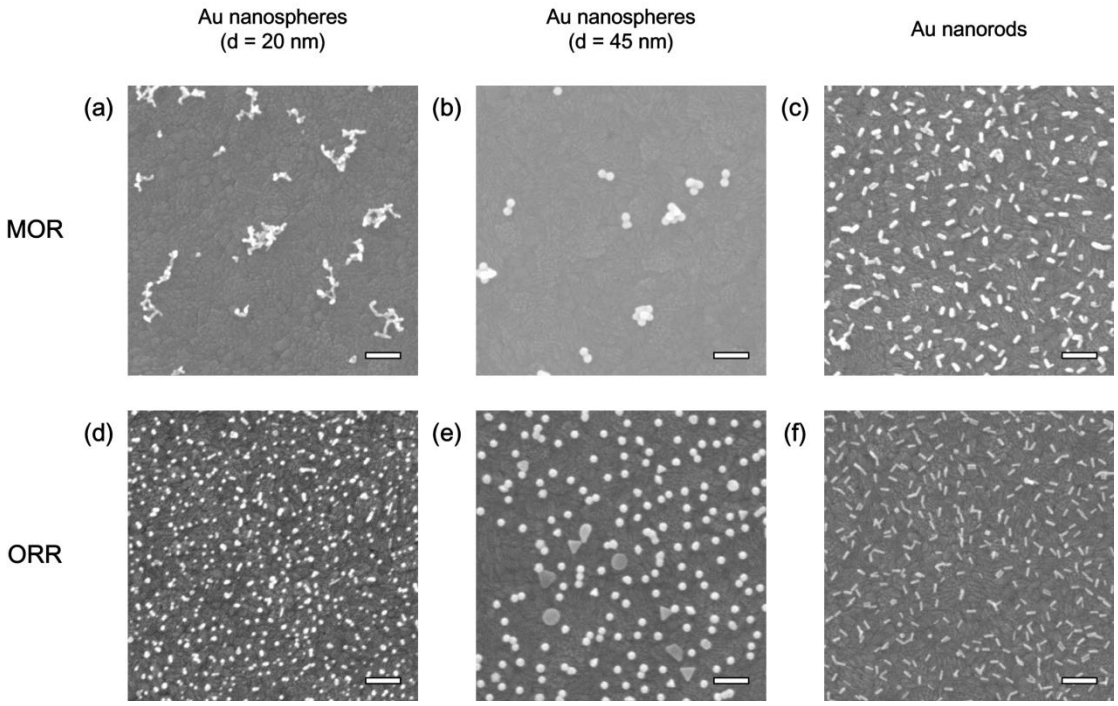

Figure 4.6 SEM images of (a and d) AuNS20s, (b and e) AuNS45s, and (c and f) AuNRs modified ITO electrodes after electrochemical scanning in (a-c) 0.1 M KOH with methanol at various concentrations for 50 cycles and in (d-f) 0.1 M PBS (pH=7.2) for 10 cycles. The scale bar is 200 nm.

4.4 Lightweight, Flexible, Nanoparticle Electrode with High

Electrocatalytic Activity

In this section, we introduce a simple yet effective drop-casting method to fabricate lightweight and mechanically flexible electrodes from AuNPs, including AuNRs and AuNS45s. The AuNP electrodes possess extremely high electroactive areas, which lead to greatly enhanced electrocatalysis towards ORR and MOR when compared to conventional gold disk electrodes. Moreover, the electrocatalytic stability of Au NRs modified electrodes towards ORR and MOR was outstanding; AuNRs keep their well-defined shapes after 1000 cycles scanning in 0.1 M PBS (pH=7.2) buffer solution or 500 cycles scanning in 0.1 M KOH with 3 M methanol.

4.4.1 Electrode Characterizations

4.4.1.1. Crystalline Structure and Morphology Characterizations

The flexible AuNP electrodes are fabricated via drying-mediated self-assembly of nanorods on tissue papers. Firstly, AuNPs are synthesized through the typical seed-mediated methods[11] and characterized by TEM and, UV-vis spectrophotometer, (For details of AuNP synthesis, please refer to Chapter Two.) and XRD analysis (Figure 4.7 (a and d)). Then, the AuNP stock solutions are drop-casted onto a 0.40×2.5 cm^2 tissue paper, which uniformly wetted the entire tissue paper by strong capillary forces.[12] This is followed by drying at 50 ℃ for 20 min. A repeated drop-casting and drying step leads to a dark-yellow paper (Figure 4.7 (b and d)) with a sheet resistance of ~20 Ω/□.

AuNPs are closely-packed but maintaining their well-defined shapes without any observable fusion (Figure 4.7 (e and f)). In some domains, AuNRs are vertically aligned. Unlike our previous free-standing monolayered nanorod superlattices,[13] in this study NRs are three-dimensionally (3D) distributed throughout the paper matrix. Such a 3D close packed assembly is uniform throughout the entire paper sheet, contributing to the high conductivity observed.

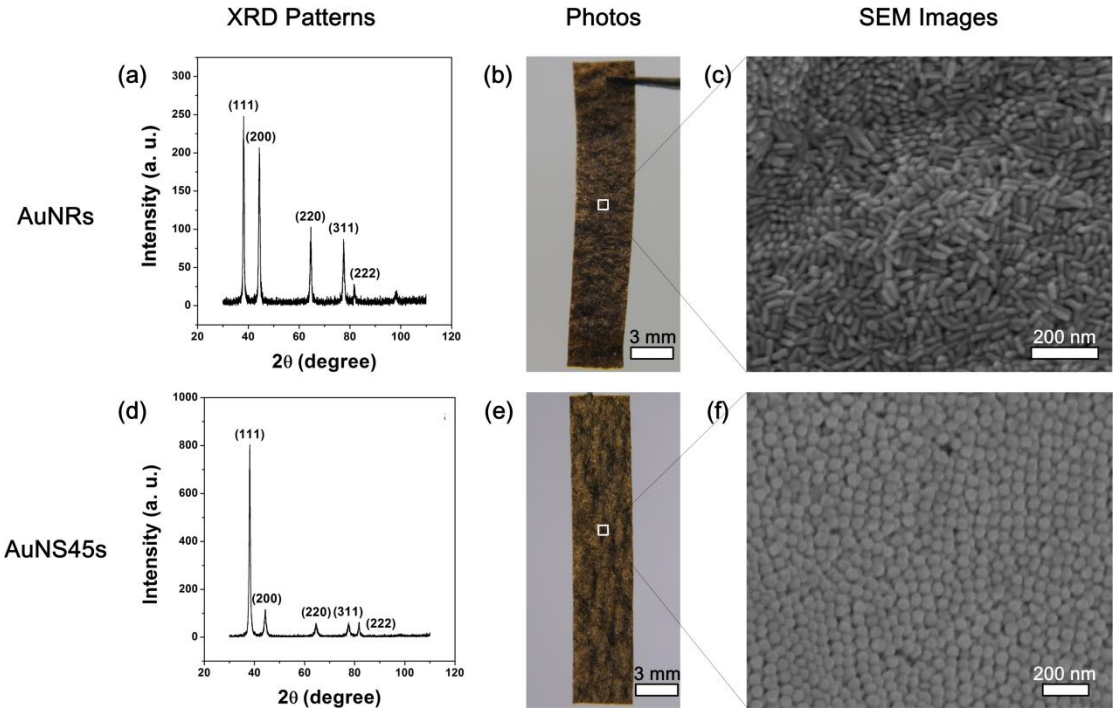

Figure 4.7 (a and d) XRD patterns, (b and e) photographic images, and (c and f) SEM micrographs of typical (a-c) AuNR electrodes and typical (d-f) AuNS45 electrodes.

4.4.1.2. Electrical Characterizations

Despite the high conductivity, the usage of gold in a typical 0.40 × 2.5 cm^2 tissue paper was only about 0.3 mg, contributing to only 7.5% of the overall electrode weight in order to achieve a resistance of around 20 Ω/□. According to current gold market price (52.21 USD g^{-1}, from http://goldprice.org/), the cost of 0.40 × 2.5 cm^2 nanorod electrode was only 0.16 US dollars.

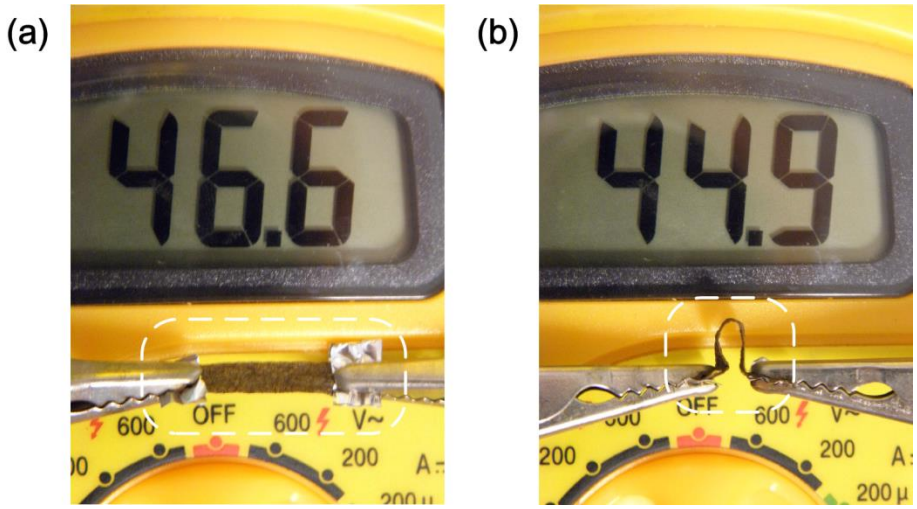

Figure 4.8 Slight conductivity changes of the AuNR electrode before (a) and after (b) bending for 180 º.

AuNRs do not affect the mechanical robustness and flexibility of tissue papers. The repeated bending from -180 º to 180 º does not break the nanorods electrodes. Remarkably, their conductivity is almost unaffected by repeated bending tests. In a typical experiment, we monitor the linear resistance changes by a multi-meter during the bending of the nanorod electrode (Figure 4.8 (a and b)). It is observed that the electrical resistance in bending state is 44.9 Ω, corresponding to 3.6% reduction of the resistance in stretching state (46.6 Ω). The slight reduction in resistance may be due to stress-induced closer packing of NRs in the bending sites. We repeat the bending process for over 100 times and observe that the overall reduction in electrical resistance was less than 5%. These experimental results show that AuNRs are strongly adhered to fibrils in tissue papers during the bending tests. Moreover, our fabrication method is general, and AuNS45 electrode was realized and shown in Figure 4.7 (e and f).

4.4.2 Electrocatalytic Behaviors

4.4.2.1. Electrochemically Active Surface Area (EASA)

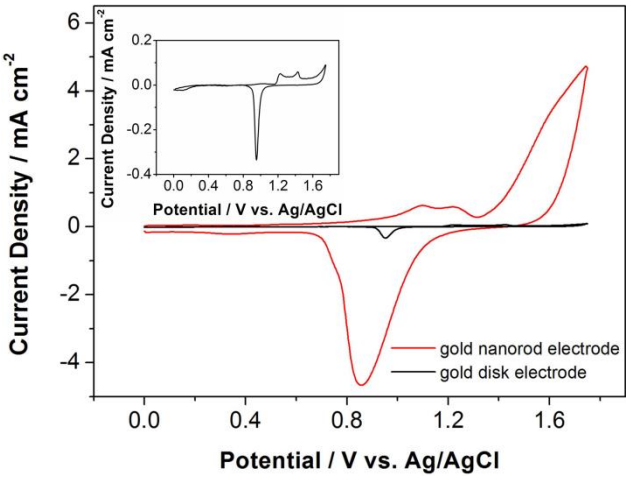

Figure 4.9 Significantly high electroactive area of AuNR electrode. Red line: CV of a typical AuNR electrode; black line: CV of a typical gold disk electrode. Inset: magnified view of the CV for the gold disk electrode. The electrochemical experiments are carried out in 0.5 M H_2SO_4 at a scan rate of 20 mV s^{-1}.

The AuNP electrodes possess extremely high surface-to-volume ratios, exhibiting much greater electrochemically active surface area (EASA) than conventional gold disk electrodes. The EASA of gold electrodes could be estimated by carrying out CV scanning in a potential window of 0 - 1.70 V versus Ag/AgCl (in 3.5 M KCl) in 0.5 M H_2SO_4 aqueous solution. The charges associated with reduction of the oxide monolayer on the gold surfaces could be used to estimate the EASA by the following equation (Equation 4.1):[4]

$$\text{EASA} = \frac{Q}{Q^*} \qquad \text{(Equation 4.1)}$$

Where Q is the charge required during the formation of gold oxide monolayer on gold surfaces, and Q^* is the calibration factor. A value of 390 $\mu C \cdot cm^{-2}$ is usually taken for Q^*. The typical CV curves for nanorods electrodes and conventional gold disk electrodes are shown in Figure 4.9. By integrating the reduction peak in red line, we obtained a Faraday charge of 0.017 C. This corresponds to an EASA of 43.7 cm^2,

which is 60 times of the geometric scanning area (0.72 cm^2). In contrast, the EASA of the gold disk electrode was only about 2 times of its geometric scanning area.

4.4.2.2. Electrocatalytic Activity towards Oxygen Reduction Reaction

Furthermore, we investigated electrocatalytic activities of AuNP electrodes towards ORR. As for ORR in PBS buffer, there are generally two consecutive steps in electron transfer reactions as follows:[14]

$O_2 + 2H^+ + 2e^- = H_2O_2$ (Equation 4.2)

$H_2O_2 + 2H^+ + 2e^- = 2H_2O$ (Equation 4.3)

Corresponding to the above two reactions, a peak at -0.05 V and a shoulder around -0.27 V are observed (Figure 4.10 (a), black curve), respectively. We further confirm the two-step four-electron transfer electrocatalytic reactions by adding H_2O_2 into the electrolyte solutions. After adding H_2O_2 into the PBS solution (Figure 4.10 (a), red line), the peak current at -0.27 V increases significantly; while the catalytic current at -0.05 V only increases slightly. This confirms that the catalytic reaction at -0.27 V is due to the reduction of H_2O_2 into H_2O. In contrast, only a single peak is observed at -0.27 V in N_2-purged PBS solution containing 0.45 mM H_2O_2 (Figure 4.10 (a), blue line). The absence of shoulder peak at -0.05 V proves diminishing of reduction from O_2 into H_2O_2. In addition, we compare the electrocatalytic activity of the AuNR electrode with that of the conventional gold disk electrode (Figure 4.10 (b)). Under the identical conditions, the electrocatalytic current density for ORR reactions on the AuNR electrodes is about 30 times of that for gold disk electrodes.

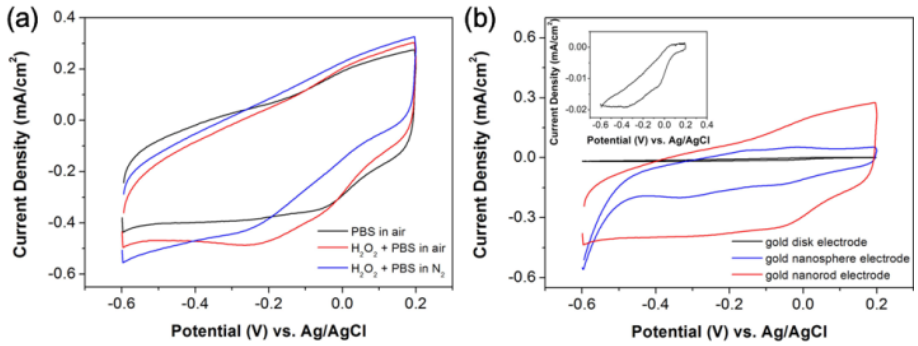

Figure 4.10 (a) CVs of the AuNR electrode in air-saturated 0.1 M PBS (black curve), in air-saturated 0.1 M PBS and in the presence of H_2O_2 (red curve), in N_2-purged 0.1 M PBS (pH=7.2) and in presence of H_2O_2 (blue curve). The scan rate was 50 mV s^{-1}. (b) CVs of AuNR electrode (red curve), AuNS45 electrode (blue curve), and gold disk electrode (black curve) in air-saturated 0.1 M PBS solution (pH=7.2) at a scan rate of 50 mV s^{-1}. The inset is a magnified view of the CV curve for gold disk electrode.

4.4.2.3. Electrocatalytic Activity towards Methanol Oxidation Reaction

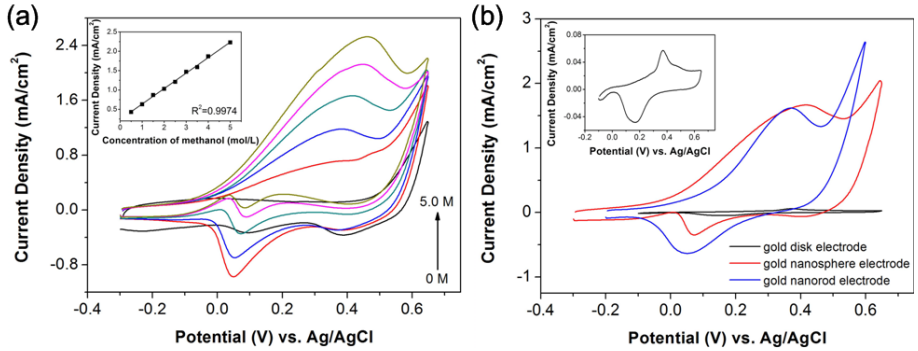

Figure 4.11 (a) Electrocatalysis of a typical AuNR electrode in 0.1 M KOH with methanol at difference concentrations. The scan rate was 50 mV s^{-1}. The inset is a plot of current density versus methanol concentration in 0.1 M KOH. The methanol concentrations are 0, 0.5, 1, 1.5, 2, 2.5, 3, 3.5, 4, 4.5, and 5 M. (b) CVs of AuNR electrode (red curve), AuNS45 electrode (blue curve), and gold disk electrode (Black black Curvecurve) in 3 M methanol in 0.1 M KOH at a scan rate of 50 mV s^{-1}. The inset is a magnified view of the CV curve for gold disk electrode.

We also investigated electrocatalytic activities of AuNP electrodes towards MOR. Figure 4.11 (a) shows the representative CV curves for MOR in 0.1 M KOH. The characteristic anodic peak at around 0.42 V is mainly due to the oxidation of methanol, whereas the cathodic peak at around 0.05 V is mainly due to the reduction of $AuO/OH^{\delta-}_{ads}$ formed during positive voltage scanning.[10, 15, 16] With the increase in methanol concentration, the anodic peak current density enhances significantly, whereas the cathodic peak current density decreases. The electrocatalytic current density is linearly

proportional to the methanol concentration (Figure 4.11 (a), inset). This phenomenon was also observed previously on other types of gold nanostructures.[16] Note that both OH^- chemically-absorbed on AuNRs, and OH^- in electrolyte solution could be involved in methanol oxidation reaction. With the increase of methanol concentration, the reaction with OH^- from solution becomes dominant but with less $Au\text{-}OH^{\delta-}_{ads}$ involved, therefore, leading to the decrease of cathodic peak current.[10, 15] In addition, the anodic peak shifts as methanol concentrations increased. We speculate that methanol may swollen paper matrix, leading to the increase of gaps between AuNRs. Consequently, methanol oxidation occurs at higher potential under higher methanol concentrations. We further compare the electrocatalytic activity of the AuNR electrodes with that of conventional gold disk electrodes (Figure 4.11 (b)). Under the identical conditions, the electrocatalytic current density for MOR reactions on the AuNR electrodes is about 30 times of that for gold disk electrodes

4.4.2.4. Mechanism of the High Electrocatalytic Activities

We investigate the mechanism of high-performance electrocatalysis towards ORR and MOR. It is known that electrocatalytic activities depend on crystalline structures of catalyst. X-ray diffraction results (Figure 4.7 (a)) show that fractions of facets of AuNR electrodes are similar to that for bulk polycrystalline gold electrodes. This indicates that AuNR electrodes have similar electrocatalytic selectivity towards ORR and MOR; therefore, the observed electrocatalytic enhancements are mainly an area effect. This is also reflected in the large capacitive currents shown in Figure 4.10, which is a consequence of the linear diffusion conditions prevailing.

4.4.2.5. Crystalline Structure Dependent Electrocatalysis

Unlike bulk gold or AuNR electrodes, AuNS45 electrodes are with dominant (111) facets (Figure 4.7 (d)), and they exhibit different electrocatalytic selectivity towards MOR and ORR. Typically, our experimental results show that EASA of AuNS45 electrodes were about 25 times of that for bulk gold; the current density of MOR on AuNS45 electrodes was about 29 times of that for bulk gold (Figure 4.11 (b)); whereas,

the current density of ORR on AuNS45 electrodes is only about 11 times of that for bulk gold (Figure 4.11 (b)). Despite the discriminative enhancement for ORR and MOR on the AuNS45 electrode, AuNR electrodes exhibit greater current densities for both reactions due to the greater EASA.

4.4.2.6. Stability during Electrocatalytic Reactions

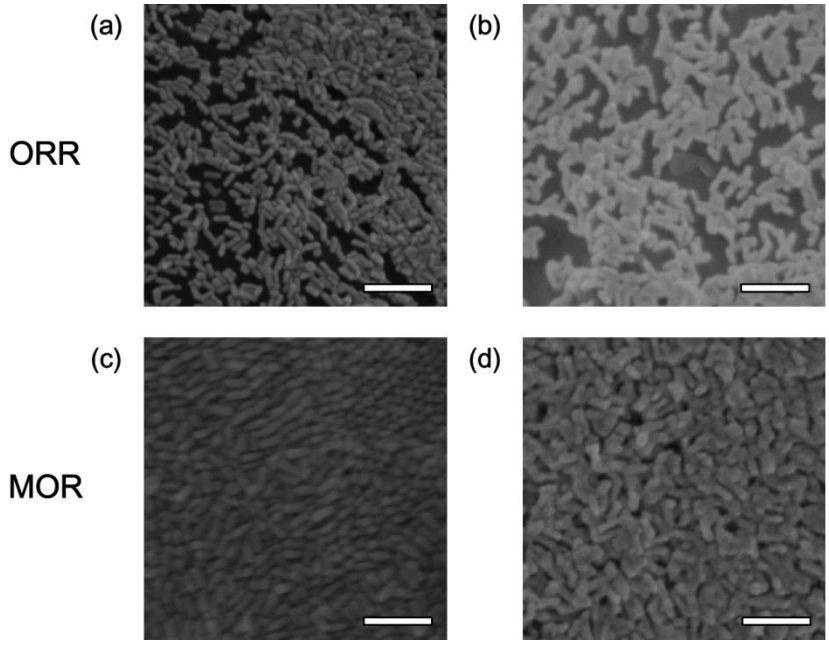

Figure 4.12 SEM images of AuNR electrode (a) before and (b) after electrochemical scanning towards ORR in 0.1 M PBS (pH=7.2) for 1,000 cycles as well as (c) before and (d) after electrochemical scanning towards MOR in 0.1 M KOH with 3 M methanol for 500 cycles.

AuNR electrodes are highly stable. There is no observable change in conductivity after storing the electrodes under the ambient conditions for six months. In addition, electrocatalytic reactions do not lead to evident changes in structures of AuNR electrodes. There are no AuNRs coming off from tissue papers during electrochemical scanning under various acid and basic conditions. We examine the morphology of AuNR electrodes before and after ORR in 0.1 M PBS (pH=7.2). As shown in Figure 4.12 (a and b), after 1,000 cycles of potential scanning, most of the AuNRs keep their well-defined shapes. As for MOR, after 500 cycles of potential scanning in the mixture solution of 0.1 M KOH and 3 M methanol, there are no evident changes in surface

structures Figure 4.12 (d). This demonstrates the excellent stability of the AuNPs modified paper electrodes in electrocatalytic reactions.

4.4.3 Universality of the Approach

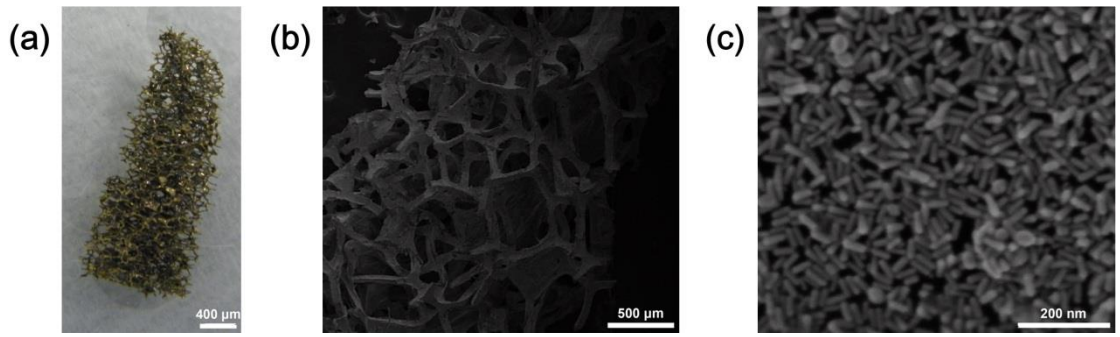

Figure 4.13 (a) A photograph of AuNRs modified sponge. (b and c) SEM images of AuNRs modified sponge under (b) low magnification and (c) high magnification.

The modification procedures are also suitable for other substrates, such as commercially available sponges. The hierarchical macroporous nature makes the sponges a strong absorbing media. Moreover, in comparison with tissue paper substrate, the pore sizes are more uniform and the junctions between single fibers are less, which provides AuNRs with a better environment for their continuous coating. After only 5 cycles of modification, the sheet resistance of AuNRs modified sponge reaches to 5 Ω/□; a result caused by the close connection among the conductive AuNRs. SEM images further confirm the uniform modification of well-defined AuNRs on sponge (Figure 4.13). Interestingly, after the modification, the skeleton of the sponge still maintains a hierarchical macroporous nature to allow the access of electrolyte solution. Therefore we predict that AuNRs modified sponge would show a much better electrocatalytic performance as compared with the paper electrodes, and relative experiments are currently under investigation.

4.5 Summary

In this chapter, the electrocatalytic applications of AuNPs modified electrodes from "bottom-up" assembly method are demonstrated and analyzed.

In the first section, we focus on the size- and shape-dependent electrocatalytic behaviors of AuNPs. To avoid the side-effects from the ligands, all of the AuNPs (AuNS20s, AuNS45s, and AuNRs) are covered by the same surfactant-positively charged CTAB. Moreover, for an accurate electrochemically measured resulted, we also develop a strategy to immobilize AuNPs robustly on the surface of ITO electrodes via electrostatic interactions. The results show that the electrocatalytic performances of AuNPs are influenced by both particle sizes and shapes. For AuNPs with similar size, the shapes or crystalline structures govern the selectivity of the electrocatalytic activity: AuNS45s show a higher mass current density in MOR than AuNRs do, since the AuNSs are dominantly covered by (111) facets; whereas AuNRs exhibit a higher mass current density in the electrocatalysis towards ORR owing to its dominant (100) facet coverage. For AuNPs with similar shapes, the mass current densities are highly dependent on the particle sizes; smaller particle sizes leads to higher electrocatalytic activities, owing to the greater surface-to-volume ratio.

In the second section, we fabricate light-weight and flexible AuNP electrodes via a simple drop-casting method. The substrate used is non-conductive, light-weight, low-cost and flexible tissue papers. Instead of chemical linking, in this work, only physical attachment is employed to tether AuNPs onto tissue paper fibers. The resulted electrodes are highly conductive and stable; therefore, we can demonstrate their electrocatalytic applications towards both ORR and MOR. Owing to the highly porous structures of tissue papers, AuNP electrodes possess an extremely high EASA, 60 times of their geometric areas. Moreover, the AuNP electrodes also present higher electrocatalytic activity in comparison with the conventional gold disk electrodes. In addition, we also proved the universality of this approach by using sponges as the substrates.

4.6 References

1. Kinoshita, K., Particle Size Effects for Oxygen Reduction on Highly Dispersed Platinum in Acid Electrolytes. *J. Electrochem. Soc.* **1990**, *137*, 845-848.

2. Solla-Gullon, J.; Vidal-Iglesias, F. J.; Lopez-Cudero, A.; Garnier, E.; Feliu, J. M.; Aldaz, A., Shape-dependent electrocatalysis: methanol and formic acid electrooxidation on preferentially oriented Pt nanoparticles. *Phys. Chem. Chem. Phys.* **2008**, *10*, 3689-3698.

3. Lim, B.; Jiang, M. J.; Camargo, P. H. C.; Cho, E. C.; Tao, J.; Lu, X. M.; Zhu, Y. M.; Xia, Y. A., Pd-Pt Bimetallic Nanodendrites with High Activity for Oxygen Reduction. *Science* **2009**, *324*, 1302-1305.

4. Wang, J.; Gong, J.; Xiong, Y.; Yang, J.; Gao, Y.; Liu, Y.; Lu, X.; Tang, Z., Shape-dependent electrocatalytic activity of monodispersed gold nanocrystals toward glucose oxidation. *Chem. Commun.* **2011**, *47*, 6894-6896.

5. Tian, Y.; Liu, H. Q.; Zhao, G. H.; Tatsuma, T., Shape-controlled electrodeposition of gold nanostructures. *J. Phys. Chem. B* **2006**, *110*, 23478-23481.

6. Orendorff, C. J.; Murphy, C. J., Quantitation of Metal Content in the Silver-Assisted Growth of Gold Nanorods. *J. Phys. Chem. B* **2006**, *110*, 3990-3994.

7. Liz-Marzan, L. M., Tailoring surface plasmons through the morphology and assembly of metal nanoparticles. *Langmuir* **2006**, *22*, 32-41.

8. Underwood, S.; Mulvaney, P., Effect of the Solution Refractive Index on the Color of Gold Colloids. *Langmuir* **1994**, *10*, 3427-3430.

9. Hamelin, A., Cyclic voltammetry at gold single-crystal surfaces .1. Behaviour at low-index faces. *J. Electroanal. Chem.* **1996**, *407*, 1-11.

10. Jena, B. K.; Raj, C. R., Synthesis of Flower-like Gold Nanoparticles and Their Electrocatalytic Activity Towards the Oxidation of Methanol and the Reduction of Oxygen. *Langmuir* **2007**, *23*, 4064-4070.

11. Nikoobakht, B.; El-Sayed, M. A., Preparation and Growth Mechanism of Gold Nanorods (NRs) Using Seed-Mediated Growth Method. *Chem. Mater.* **2003**, *15*, 1957-1962.

12. Roberts, J. C., *Paper Chemistry*. Springer: NY, 1996.

13. Ng, K. C.; Udagedara, I. B.; Rukhlenko, I. D.; Chen, Y.; Tang, Y.; Premaratne, M.; Cheng, W., Free-Standing Plasmonic-Nanorod Superlattice Sheets. *ACS Nano* **2011**, *6*, 925-934.

14. El-Deab, M. S.; Okajima, T.; Ohsaka, T., Electrochemical reduction of oxygen on gold nanoparticle-electrodeposited glassy carbon electrodes. *J. Electrochem. Soc.* **2003**, *150*, A851-A857.

15. Assiongbon, K. A.; Roy, D., Electro-oxidation of methanol on gold in alkaline media: Adsorption characteristics of reaction intermediates studied using time resolved electro-chemical impedance and surface plasmon resonance techniques. *Surf. Sci.* **2005**, *594*, 99-119.

16. Kim, J.; Lee, S. W.; Hammond, P. T.; Shao-Horn, Y., Electrostatic Layer-by-Layer Assembled Au Nanoparticle/MWNT Thin Films: Microstructure, Optical Property, and Electrocatalytic Activity for Methanol Oxidation. *Chem. Mater.* **2009**, *21*, 2993-3001.

This page is intentionally blank

Chapter Five

Applications of Flexible Electronics

In this chapter, the electrical applications of copper nanowire-based aerogels from "bottom-up" assembly were demonstrated.

5.1 Chemicals and Materials

Table 5.1 The Chemicals Used for Electrical Characterizations

Chemical Names and/or molecular formula	Purity	Supplier
(Heptadecafluoro-1,1,2,2-tetradecyl)trimethoxysilane (FAS)	≥ 98%	Sigma-Aldrich
Oil Blue	96%	Sigma-Aldrich
Ethanol (C_2H_5OH)	96%	Merck
Chloroform ($CHCl_3$)	99.0-99.1%	Merck
Toluene	≥ 99%	Merck
Hexane	≥ 98%	Merck

All chemicals listed in Table 5.1 are used as received. Ultrapure water (18.2 MΩ·cm), purified using a Barnstead NANOpure Water Purification System (received from K. I. Scientific Pty. Ltd., North Ryde, NSW, Australia), was used for all experiments. Unleaded #91 gasoline was obtained from Shell fuel station in Australia. PELCO®

colloidal silver was purchased from Ted Pella, Inc (Redding, USA).

5.2 Instrumentals

5.2.1. Scanning Electron Microscopy (SEM)

SEM images were taken using an FEI Nova NanoSEM 430 field emission gun scanning electron microscope, located at MCN. The Nova NanoSEM 430 operates with a Schottky-type field emission gun (FEG) with a maximum electron probe of > 200 nA. Samples without metal sputter coating were directly adhered onto the sample holder using conductive carbon tape from ProSciTech. All SEM images were taken with 5 kV acceleration voltage in a vacuum less than 2×10^{-4} Pa, a working distance of 5 mm and the probe current set to the arbitrary number 8 (medium sized probe).

5.2.2. Wide Angle X-Ray Diffraction (WXRD)

WXRD patterns were obtained at room temperature on a Philips PW1140/90 diffractometer with a CuKα radiation source (40 kV, 25 mA, λ = 1.54 Å). For liquid samples, the measurement was completed by dropping highly concentrated copper nanowire (CuNW) solution on a cell of a sample holder normally made by silicon or quartz and followed by drying. For solid samples, the CuNW monolith aerogels were directly left on the sample holders. Generally, the scan rate is 2Theta = $1^{o} \cdot min^{-1}$ and the scan region was between 2Theta = 30º and 110º.

5.2.3. Electrochemical System

Current variations were measured and recorded by using a PARSTAT 2273 advanced electrochemical system (Princeton Applied Research). A thin layer of liquid silver colloid was employed to optimize the electrical contact between CuNW monoliths or CuNW based composites and the conducting wires (aluminum foils).

5.2.4. Electrical Conductivity Measurements

Conductivity of CuNW monoliths was checked through a two-probe technique. A thin layer of liquid silver colloid was employed to optimize the electrical contact between CuNW monoliths and aluminum foils, and the resistance was measured by a multi-meter or a PARSTAT 2273 advanced electrochemical system (Princeton Applied Research).

5.2.5. Mechanical Property Measurement

Mechanical properties of cylindrical shaped CuNW aerogel monoliths and CuNW based composites were measured by a Micro Tester Instron (5848) using a 10 N load cell and strain control mode with a strain rate of 100% min^{-1}. Normally, the diameters of the aerogels were around 1 cm and the heights of them were 1 to 2 cm.

5.3 Ultralow-Density Copper Nanowire Aerogel Monoliths with Tunable Mechanical and Electrical Properties

In this section, we introduce a freeze-casting method, under mild conditions, to produce ultralow-density copper aerogel monoliths with well-defined shapes from one-dimensional (1D) building blocks – copper nanowires (CuNWs). By using freeze-casting method, a centimeter-scale CuNW aerogel monolith with well-defined shapes are produced; the aerogel density could be adjusted over a wide range and a density of as low as 4.6 mg·cm^{-3} was achieved. As a result, both conductivity and mechanical strengths could be systematically measured and tuned from 0.90 to 1.76 S·cm^{-1} and from 1.74 to 12.96 Pa, respectively.

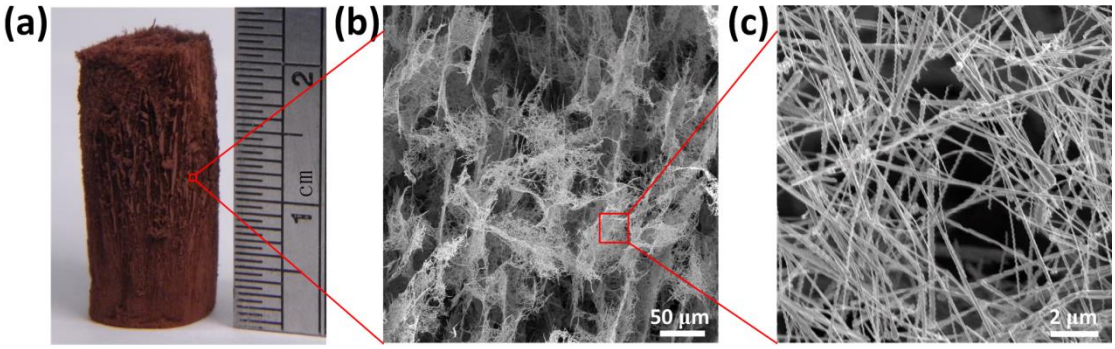

Figure 5.1 Characterizations of typical CuNW aerogel monoliths. (a) Photographic image; (b and c) SEM images at different magnifications. Note that CuNWs formed tube-like porous structures.

5.3.1 Morphology Characterizations

A photographic image of a typical CuNW aerogel monolith with a density of ~ 9.2 mg·cm^{-3} is shown in Figure 5.1 (a). Although the density accounts for only about 1‰ of that of bulk copper, a well-defined cylinder shape with the length of 2.25 cm and the diameter of 0.95 cm is clearly maintained during the entire freeze-casting process.

Further characterizations by SEM (Figure 5.1 (b)) show that this CuNW aerogel monolith possesses a tube-like microstructure, reflecting the shapes of ice crystal rods. Note that the "tube" walls are composed of primary CuNWs, and there are no observable damages to the NWs during the freeze-drying process (Figure 5.1 (c)). The densities of CuNW aerogel monoliths could be simply controlled by adjusting the concentration of CuNW aqueous solutions. The lowest density achieved in this study is about 4.6 $mg \cdot cm^{-3}$. The internal structures for CuNW aerogel monoliths with densities of 4.6, 8.3 and 13.5 $mg \cdot cm^{-3}$ are characterized by SEM (Figure 5.2), showing that CuNWs are uniformly distributed throughout the aerogel matrix. Meanwhile, we also calculated the porosity of the CuNW aerogel monoliths from their densities, the results indicated that the aerogels are highly porous, within the porosity ranging from 98.25% to 99.91%.

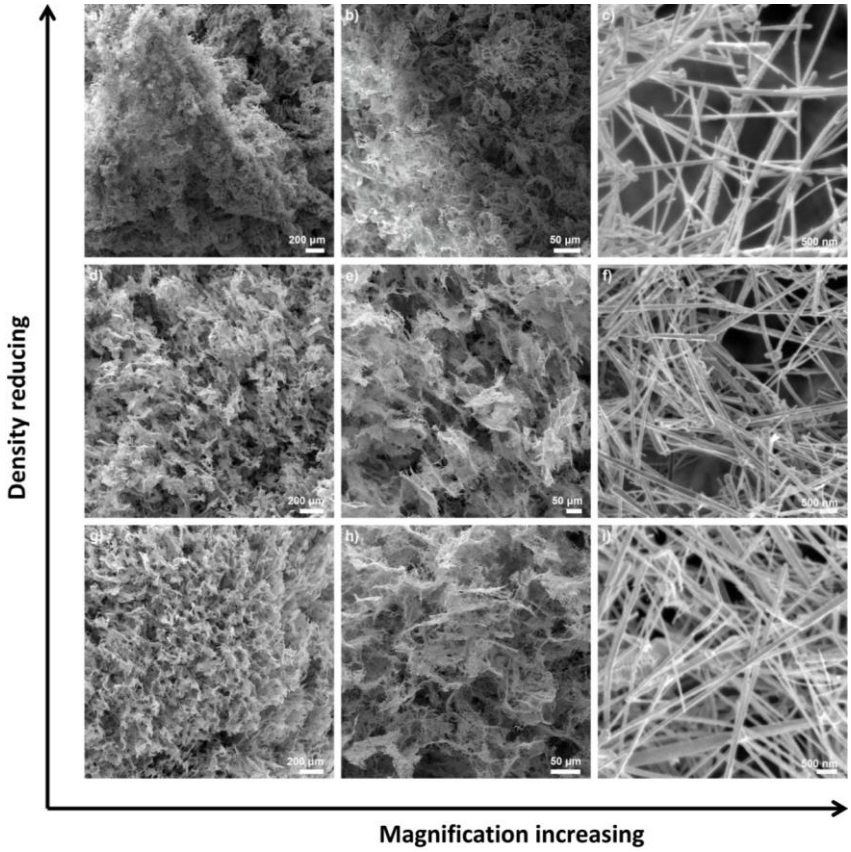

Figure 5.2 SEM images of CuNW aerogel monoliths with different densities: (a-c) 4.6 mg cm^{-3}, (d-f) 8.3 mg cm^{-3}, and (g-i) 13.5 mg cm^{-3} under various magnifications.

5.3.2 Electrical Properties

We systematically investigate the effects of aerogel density on the electrical conductivity. To measure conductivity, cylindrical CuNW aerogel monoliths are sandwiched between aluminum foils and a thin layer of silver paste is applied to establish conformal contact between aerogels and aluminum foils. A set of NW aerogel monoliths with different densities are fabricated and their conductivities are measured. Figure 5.3 shows a normalized plot by plotting the relative electrical conductivity (defined as the measured electrical conductivity of aerogel, σ, divided by the electrical conductivity of the corresponding bulk solid, σ_s) against relative density (defined as the measured density of aerogel, ρ, divided by the density of the corresponding bulk solid, ρ_s). As predicted by percolation theory,[1] a power-law scaling described well the relationship between relative conductivity and density (or porosity). A characteristic exponent of 0.81 is obtained for our CuNW aerogel monoliths. This value is smaller than that of copper foams fabricated by the lost carbonate sintering method,[2] The reason for this may be due to the higher porosity. Our CuNW aerogels have a porosity of 98.25% to 99.91%; whereas, the copper foams by the sintering approach have a porosity of 75% to 85%. According to the percolation theory, defect is one of primary factors influencing the characteristic exponents.[3] As for our ultralow-density CuNW aerogel monoliths, there may be high possibility of defects. In addition, CuNWs are one-dimensional building blocks and their contacts within aerogels appeared to be loose in some domains (Figures. 5.1 (c) and 5.2). This could be another preventing factor in electron flows within the aerogel matrix.

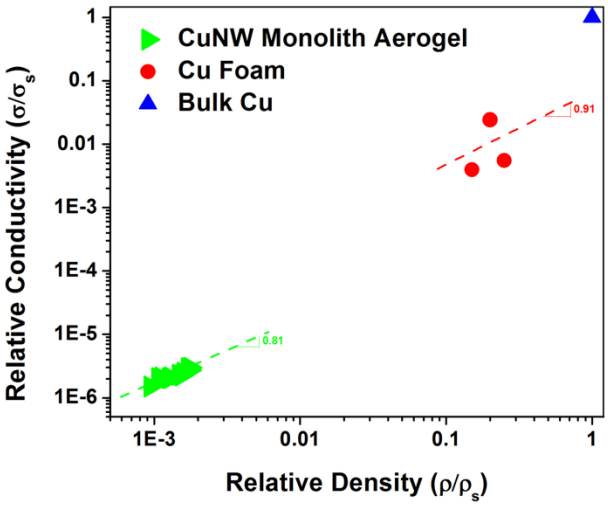

Figure 5.3 The plot of relative electrical conductivity (σ/σ_s) as a function of relative density (ρ/ρ_s) of CuNW aerogel monoliths (green triangle). The data of Cu Foam and bulk cooper are added for comparison. Note that our CuNWs-based approach leads to lower-density copper monoliths.

5.3.3 Mechanical Properties

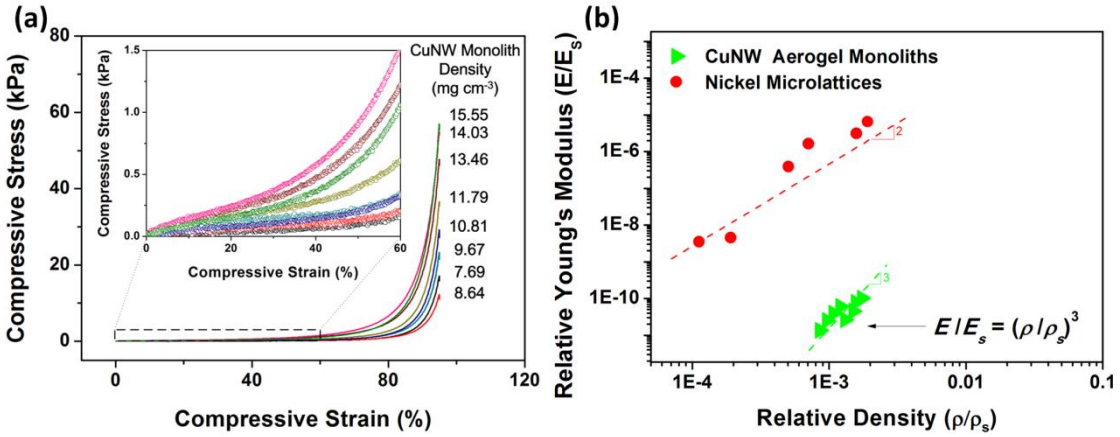

Figure 5.4 Mechanical properties of CuNW aerogel monoliths. (a) Compressive stress-strain curves of CuNW aerogel monoliths with various densities (The inset curves show the compressive stress under up to 60% compressive strain.). (b) The plot of relative Young's modulus (E/E_s) as a function of relative density (ρ/ρ_s) of CuNW aerogel monoliths. The data of nickel microlattices (red dots) was added into the same graph for comparison. Note that CuNW aerogel monoliths exhibited a steeper scaling property than nickel microlattices.

In addition, we investigate mechanical properties of our CuNW aerogel monoliths.

Typical compressive stress-strain plots of CuNW aerogel monoliths with various densities are shown in Figures. 5.4 (a), which exhibit the typical behaviors of porous aerogel materials, namely elastic deformation followed by densification.[4] Notice the elastic region is controllable through the densities of CuNW monoliths (Figures. 5.4 (a) inset); CuNW aerogels are even elastic with the strain up to 50% with the density of 7.69 $mg \cdot cm^{-3}$. The slope of stress-strain curves in elastic regions was used to derive Young's modulus.[5] By adjusting aerogel density from ~ 7.69 $mg \cdot cm^{-3}$ to 15.55 $mg \cdot cm^{-3}$, the Young's modulus could be tuned between 1.74 Pa and 12.96 Pa. Under larger stains, the stress increased dramatically indicating the collapsing of the materials, indicating considerable stiffening as a result of densification.

Furthermore, we investigate the relationship between relative Young's modulus (defined as the measured Young's modulus, E, divided by the Young's modulus of the constituent solid, E_s) and relative density of CuNW aerogel monoliths and compare the results with other low-density, self-supported, and porous materials as shown in Figures. 5.4 (b). The relative Young's modulus is found to scale with $(\rho/\rho_s)^3$, consistent with that observed in other low-density materials constructed by 1D nanostructures, such as carbon nanotube (CNT) foams.[6] In contrast, the Young's modulus for nickel microlattices scaled with $(\rho/\rho_s)^2$.[7] The steeper scaling in our CuNW aerogel monoliths indicates the load transfer among CuNWs is not as efficient as that throughout the nickel microlattices. This may be due to the fact that CuNWs were loosely connected in some domains (Figures 5.1 (c) and 5.2), which may cause low efficiency in load transfer.

5.3.4 Wetting Properties

The surface wetting properties of CuNW aerogel monoliths can be easily engineered. In

a typical example, a uniform layer of (Heptadecafluoro-1,1,2,2-tetradecyl)trimethoxysilane (FAS) could cover CuNW surfaces throughout the aerogels by vapor deposition.[8] This turns the monoliths from superhydrophilic to superhydrophobic: the contact angle of pristine monoliths is 0º; whereas the contact angel of FAS-modified monoliths is 158.7 ± 2.3º (Figure 5.5 (a)). Consequently, the pristine CuNW monoliths submerge into water; whereas FAS-modified monoliths float on top of water surface (Figure 5.5 (b)).

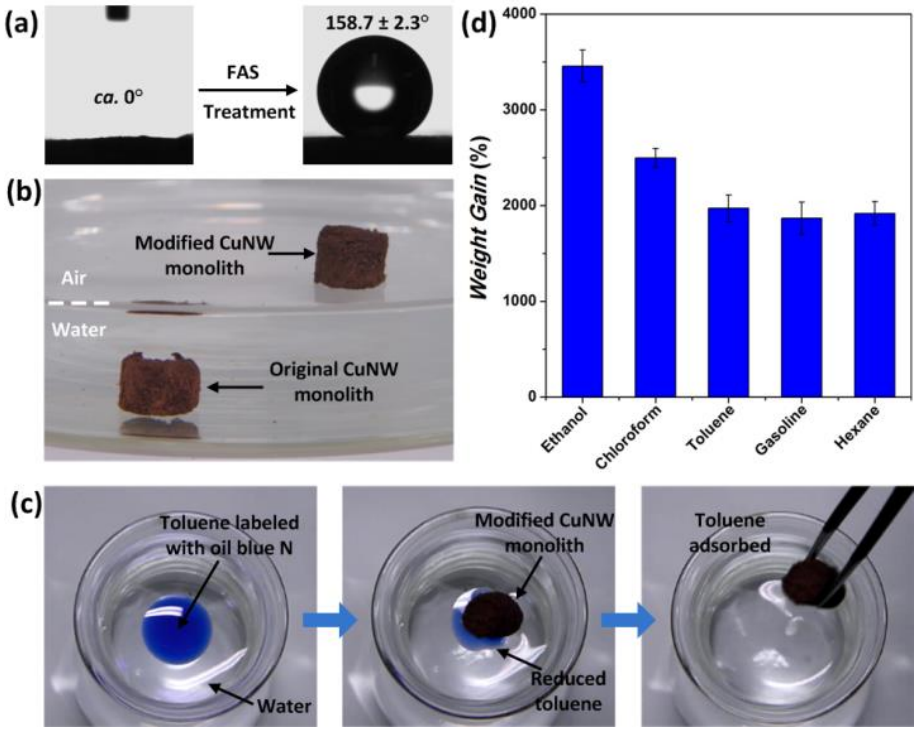

Figure 5.5 Engineering wetting properties of CuNW aerogel monoliths and their use as selective absorbents for a range of organic solvents. (a) Water contact angle the as-prepared CuNW aerogel monolith changed from superhydrophilic to superhydrophobic after FAS coating; (b) Photographic image showing that original CuNW aerogel monolith submerged into water but FAS-coated CuNW aerogel floated on water surface; (c) Autonomous absorbing process of a droplet of oil blue N-labeled toluene by FAS-coated CuNW aerogel monolith. The whole process took only 3 seconds; (d) Absorption capacities of CuNW aerogel monoliths towards a range of organic solvents and oils in terms of weight gain.

FAS-modified CuNW aerogel monoliths could be potentially used as selective adsorbents for oil-spill cleanup by a combined superhydrophobicity and capillary

action (Figure 5.5 (c and d)). As shown in Figure 5.5 (c), when a piece of CuNW aerogel monolith is brought to contact with a droplet of oil blue N labeled toluene, it automatically absorbs all the organic solvent without human intervention. The entire process takes less than 3 seconds. In addition, FAS-coated monoliths could absorb a collection of other organic solvents including gasoline. The maximum weight gain could be as high as ~34 times of the original aerogel weight (Figure 5.5 (d)). The value is higher than that for manganese oxide nanowire membranes,[9] perhaps due to the higher porosity of our CuNW aerogel monoliths.

5.4 Manufacturable Conducting Rubber Ambers and Flexible Conductors from Copper Nanowire Aerogel Monoliths

Foldable and stretchable conductors are a new class of advanced materials which can maintain high conductivity under various deformations, including bending,[10] stretching,[11] compressing,[12] and twisting.[13] Such type of conductors have implications in a wide spectrum of technological fields,[14] including electronic paper,[15] flexible displays,[16] touch screens,[17] artificial skins,[18-20] and implantable medical devices.[21] Over the past several years, substantial progress has been made in designing flexible conductors with diverse materials, such as carbon nanotubes,[22] graphene,[23] conductive polymers,[24] semiconducting nanostructures,[25, 26] metal oxides,[27] metallic nanoparticles,[28-30] and metal nanowires.[10, 31, 32]

Despite the exiting progress, some of the afore-mentioned materials will unavoidably face cost or low-abundance issues in terms of downstream practical real-world applications. For example, the success in metal nanomaterials-based flexible conductors was predominantly limited to precious gold or silver. [10, 28, 29] Note that

copper is approximately 100 times cheaper and 1000 times more abundant than silver, yet possesses comparable bulk conductivity to silver. Hence, copper is potentially of great value for commercial applications of flexible conductors.[33] However, copper nanomaterials are largely under-explored in fabrication of flexible conductors due to their high-tendency to oxidation and low solvent dispersion.[34]

In the previous section, we have successfully fabricated ultra-lightweight aerogel monoliths from CuNWs, which could exhibit high conductivities even when their densities were about 1/1,000 of bulk copper.[35] However, the poor mechanical stability prevented CuNWs aerogel monoliths from being used as the foldable and stretchable conductors. Herein, we show a trace amount of additive – polyvinyl alcohol (PVA) could substantially improve the mechanical strength of CuNWs aerogels while maintaining high conductivity (~ 0.83 S cm^{-1}) and ultra-low density (~10 mg cm^{-3}). The CuNW-PVA composite aerogels exhibited high durability at cyclic loads, enabling their applications as the elastic piezo-resistivity switch. More importantly, the CuNW-PVA aerogels could be embedded into PDMS matrix, leading to electrically conductive rubber ambers without the need of pre-wiring which was required in the previous aerogel-based conductors.[10, 22, 36] The rubber ambers could be further manufactured into various 1D, 2D and 3D objects that were all conductive after shaping. We believe that our fabrication strategy represents a new low-cost route to manufacture under mild conditions flexible conductors with versatile shapes for versatile applications in flexible electronics.

5.4.1 Morphology Characterizations

Figure 5.6 (a) shows the photographic image of a typical cylindrical CuNW-PVA (10) composite aerogel monolith which has a density of only 9.6 mg cm^{-3}. Further

characterizations by scanning electron microscopy demonstrated highly-porous, interconnected tubular structures (Figures 5.6 (b and c)). In contrast, broken tube-like structures were observed in the CuNW aerogel monoliths (Figure 5.2). Unlike previously reported polymer-silver composite aerogels where individual metallic nanowires are wrapped by polymers,[37] it appears that the PVA polymers existed throughout the entire 3D scaffolds of CuNWs (Figures 5.6 (c)). Despite this, the entire aerogel remained highly conductive with a conductivity of 0.83 S cm^{-1}, only about 26% lower than the conductivity for the corresponding CuNW aerogel monoliths without PVA. The conductivity for our composite aerogel can compete with the values for highly conductive aerogels composed of metallic nanostructures or carbon materials.[23, 38]

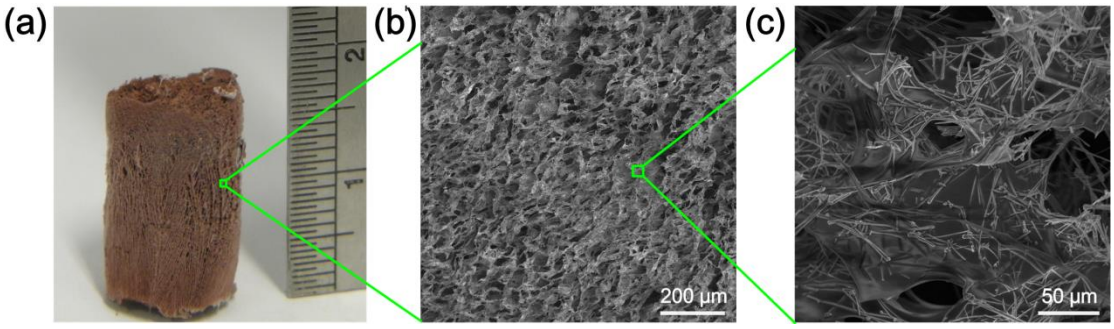

Figure 5.6 (a) Photographic image. (b and c) SEM images at different magnifications. Note that CuNW-PVA mixtures formed tube-like porous structures.

5.4.2 Mechanical Properties

PVA substantially improved the mechanical robustness and flexibility of CuNW aerogels, allowing for large deformations without fracturing. The CuNW-PVA (10) composite aerogel could almost return to its original height (Figure 5.7 (a)). The force curves for CuNW-PVA (10) and CuNW-PVA (20) (Figures 5.7 (c and d)) composite

aerogels under various compressive strains further confirmed the elasticity. All the stress-strain curves featured plateau regions followed by steep regions. In the plateau regions, compressive stress gradually increased with the strain, indicating elastic deformation; in the steep regions, the stress increased rapidly with the strain owing to the densification of porous structures.[12] In addition, Young's modulus for CuNW-PVA (10) composite aerogels was increased to 27 times of that of CuNW aerogel monoliths (Figure 5.7 (d)).

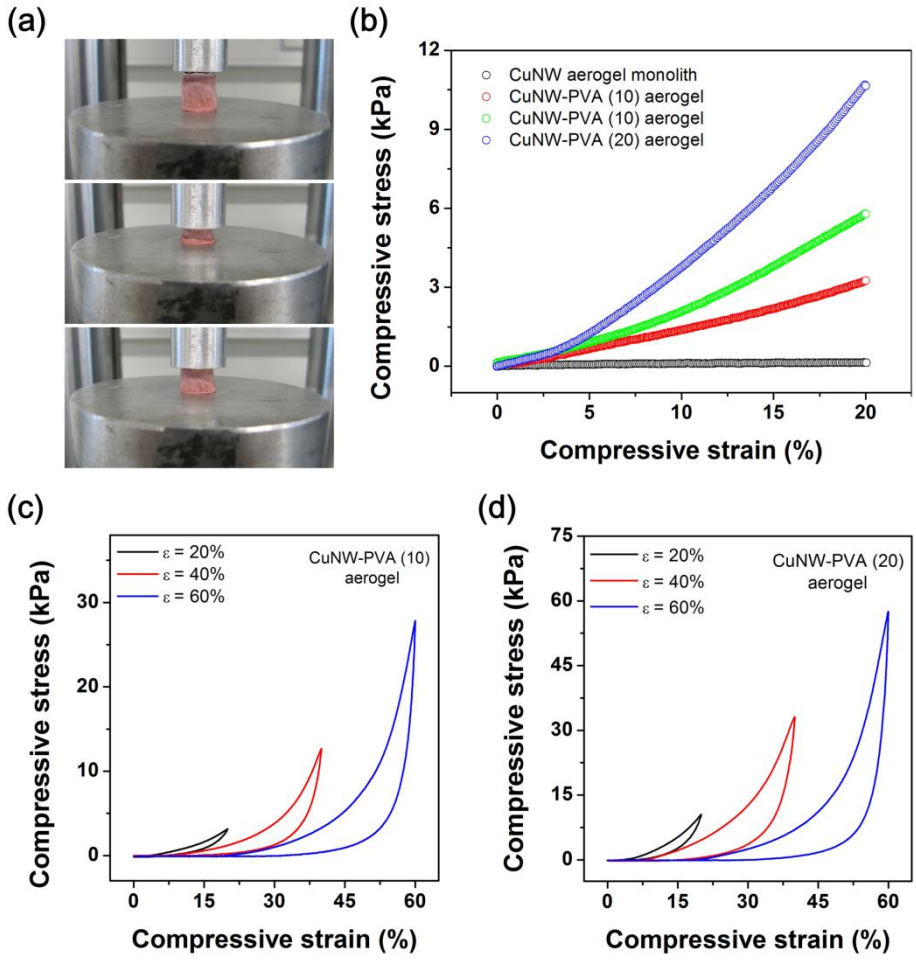

Figure 5.7 Mechanical properties of CuNW-PVA composite aerogels. (a) Photos of CuNW-PVA (10) composite aerogels during compressing process. (b) Compressive stress–strain curves of CuNW aerogel monoliths and CuNW-PVA composite aerogels with various contents of PVA. (c and d) Compressive stress–strain curves of (c) CuNW-PVA (10) and CuNW-PVA (20) composite aerogels at different set strains Ɛ of 20, 40, and 60%.

5.4.3 Effects of PVA Concentrations

We systematically investigated the effect of PVA concentration, *x* on density, Young's modulus, electrical conductivity of CuNW-PVA composite aerogels as summarized in Table 5.2. By varying concentration, *x* from 0 to 20 mg l^{-1}, the density of the aerogel only increased slightly up to a maximum of ~ 7% from ~ 9.4 mg cm^{-3} to ~ 10.1 mg cm^{-3}; the electrical conductivity decreased by about 4 times from ~1.13 $S.cm^{-1}$ to 0.29 $S.cm^{-1}$; however, the Young's modulus of the composite aerogel increased up to 93 times from 5.88 Pa to 545.69 Pa.

Table 5.2 Summary of density, electrical conductivity, Young's modulus, and elasticity of CuNW aerogel monolith and CuNW-PVA composite aerogels with different contents of PVA

Samples	**CuNW Monolith Aerogels**	**CuNW-PVA (10) Composite Aerogels**	**CuNW-PVA (15) Composite Aerogels**	**CuNW-PVA (20) Composite Aerogels**
Density ($mg \cdot cm^{-3}$)	9.4 ± 0.9	9.6 ± 0.2	9.9 ± 0.3	10.1 ± 0.5
Young's Modulus (Pa)	5.88	159.87	286.90	545.69
Electrical Conductivity ($S \cdot cm^{-1}$)	1.13	0.83	0.39	0.29
Elasticity	×	√	√	√

The outstanding mechanical and electrical properties of the CuNW-PVA aerogel monoliths originate from their unique internal structures. Loosely-bound CuNWs couldn't sufficiently maintain the porous frameworks during freeze-drying process, especially in the case of aerogels from low concentrations of CuNWs, leading to broken tubular structures observed (Figure 5.2). This led to low elasticity due to the low efficiency in load transfer among broken tubular structures. In contrast, in the presence of PVA, highly-porous CuNWs frameworks were largely maintained (Figures 5.6 (b and c)). PVA served as "nanoglue", effectively fixing the CuNWs structures and promoting the load transfer throughout the networks. This explains the dramatic enhancement in mechanical properties observed in this work (Table 5.2). Interestingly, it appears that PVA didn't break the ohm contacts between CuNWs but wrapped their junction points. Therefore, the conductivity of the aerogel didn't decrease much after introducing PVA (Table 5.2). Note that the role of PVA (i.e. nano-gluing effects) in our aerogel were fundamentally different from that in the previous composite aerogels,[4, 37] in which PVA conformably coated individual nanowires to exhibit nano-cabling effects in electrical properties.

5.4.4 Electrical Applications as Piezo-Resistivity Switches

The excellent conductivity in conjunction with high mechanical compliance exhibited by our CuNW-PVA composite aerogels indicated their potential applications in flexible electronics. Figure 5.8 (a) shows the changes of electrical resistance under compressive stress for CuNW-PVA (20). Note that the electronic resistance decreased rapidly in the initial stage of compression, and then reached a plateau after a strain of about 30%. This may be originated from pressure-driven percolation conductivity.[39] The overall conductivity of the composite aerogel, σ depends on the effective volume fraction of CuNWs (the ratio of total volume of CuNWs to the total volume of the deformed aerogel). Consider an initially non-conductive homogeneous insulator matrix uniformly

doped with conductive materials.

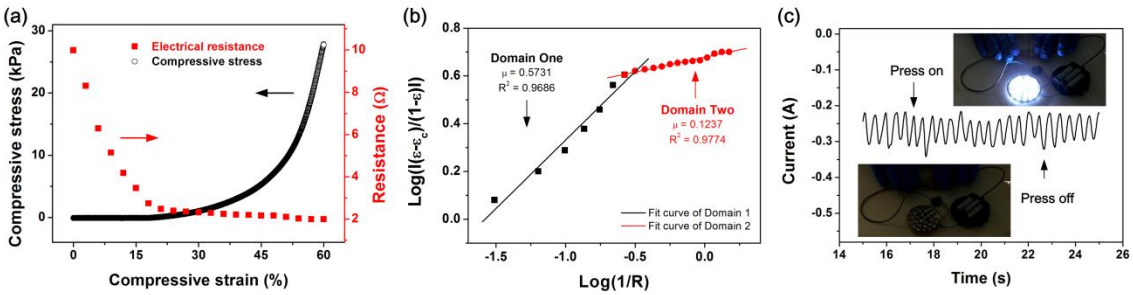

Figure 5.8 Electrical properties of CuNW-PVA composite aerogels under compressive strains. (a) Plots of electrical resistance and compressive stress as a functional compressive strains for the CuNW-PVA (20) composite aerogel monolith. (b) Plots of $|(\varepsilon-\varepsilon_c)/(1-\varepsilon))|$ versus 1/R in logarithmic scale. The black curve represents the linear fitting of data points (black) in the Domain one, and the red curve is the fitting of the data points (red) in the Domain two. Note that (1/R) is proportional to σ and ($1/R_c$) is proportional to σ_c. (c) Variation of electrical resistance and compressive stress with compression deformation of a CuNW-PVA (20) composite aerogel.

The pressure-controlled percolation conductivity in terms of strain can be written as a power law function:[39]

$$\sigma(\varepsilon)_{\varepsilon>\varepsilon_C} \propto \sigma_C \left|\frac{\varepsilon-\varepsilon_C}{1-\varepsilon}\right|^{\mu}$$

where, $\sigma(\varepsilon)$ is the conductivity at the stress ε; σ_c is the conductivity percolation threshold at the stress ε_c; μ is the conductivity exponent. Now we assume our CuNW-PVA aerogel monolith obeys this theory and assume $\varepsilon_c = 0$ since all our CuNW-PVA aerogels were conductive without any compressive stress. The results presented in Figure 5.8 (b) manifest two evident domains with different exponents of the power law – 0.57 and 0.12. The excellent linear relationships validate the percolation theory. However, the values of the exponents are much less than the predicted $\mu = 2.0$ for 3D systems. The apparent discrepancy in conductivity exponents could be understood since our systems were far beyond the conductivity percolation threshold. Interestingly, clear sharp transitions in Figure 5.8 demonstrated the presence of another "conductivity threshold". This may be attributed to the percolation of porous structures under compressive stress: the conductivity in the domain one may be due to the deformation

of pores accompanying squeezing air out the matrix; the conductivity in the domain two may be due to the densification of CuNWs like the normal homogenous insulator matrix far beyond the conductivity percolation threshold.

The unique piezo-resistivity properties enabled our CuNW-PVA composite aerogels to directly serve as elastomeric resistor switches. To illustrate the capability, a CuNW-PVA (20) composite aerogel was sandwiched between two conducting silver paste-coated glass slides to form a resistor. The resistor was then connected to light emitting diodes (LED) and batteries in series. As shown in Figure 5.8 (c), upon pressing the aerogel LED lamps became brighter and upon de-pressing the lamps returned to dim. This is due to the piezo-resistive effects described above. Under compressive stress, the resistance of the aerogel decrease, leaving more partial voltage to LED lamps to make them brighter; upon de-pressing, the elastic aerogel returned to the original shape and recovered to large resistance, leaving less partial voltage to LED lamps to make them dim again.

5.4.5 Electrical Applications as Manufacturable Conductive Rubber Ambers

Another unique attribute is that our CuNW-PVA aerogels could be embedded into PDMS matrix to form conducting rubber ambers without the need of pre-wiring (Figure 5.9 (a)). The aerogels were mechanically robust and no deformation was observed during the PDMS embedding (Figures 5.9 (b and c)). More importantly, the aerogel rubber ambers could be easily cut into arbitrary 1D, 2D, and 3D shapes (Figures 5.9 (d-f)), and all the shaped rubbers were directly conductive without the need of pre-wiring. Similar conducting aerogel rubber was reported earlier but the pre-wiring was required.[10, 22, 36] Moreover, the shaped rubber ambers could be further manufactured

into various complex structures such as plaited and twisted structures. PDMS embedding substantially enhanced the compressive strength by 200-fold, up to a Young's modulus of 37.5 kPa (Figure 5.9 (g)). Despite this, the conducting rubber ambers remained electrically responsive to compressive stress. A prototype of elastic piezo-resistivity device could be obtained (Figure 5.9 (i)).

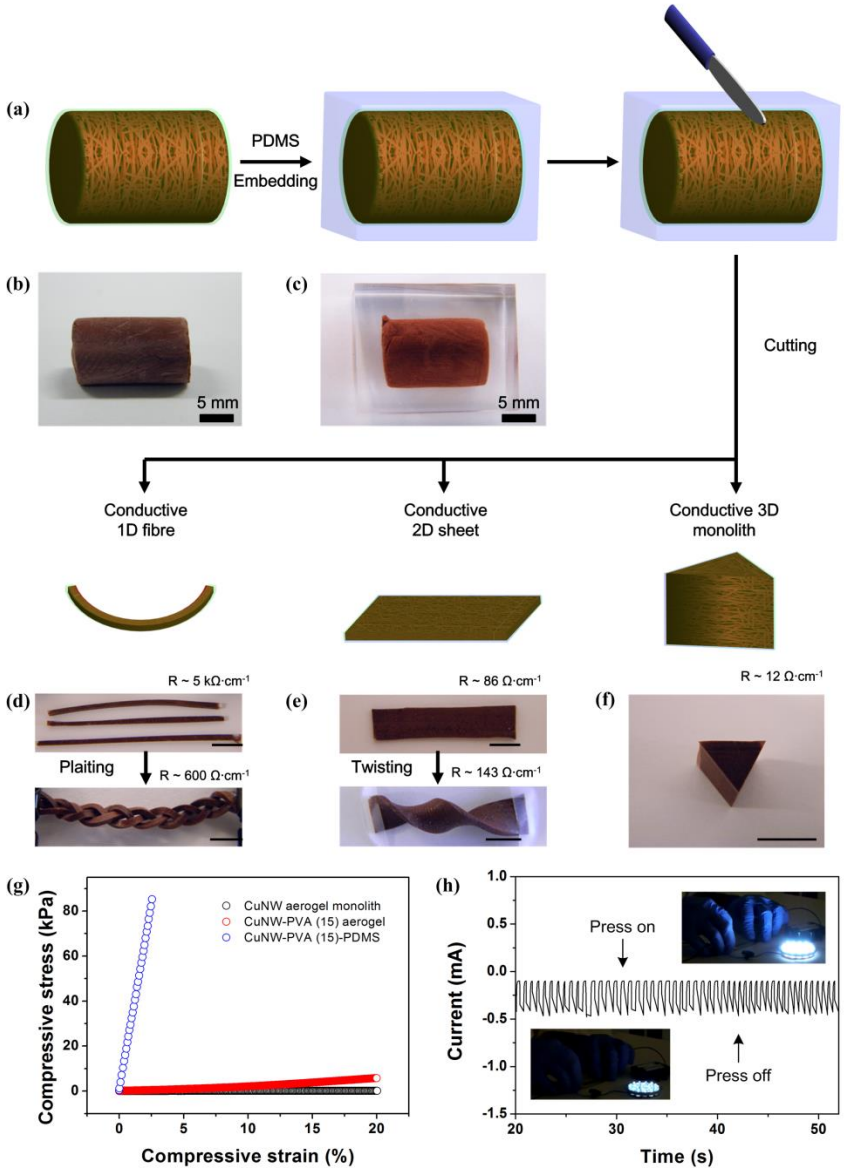

Figure 5.9 Manufacturability of the conducting rubber ambers by simple cutting. (a) Schematic of the amber-fabrication process and the follow-up cut-shaping process. (b and c) Photographic images of CuNW-PVA aerogel monoliths before (b) and after (c) after PDMS embedding. (d-f) cut-shaped 1D, 2D, and 3D structures. All the structures were condutive. (g) Compressive stress–strain curves of CuNW aerogel monoliths, CuNW-PVA composite aerogel monoliths, and CuNW-PVA-PDMS rubber ambers. (h) a prototype of rubber amber-based piezo-resistivity switch.

5.5 Summary

In this chapter, mechanical and electrical properties of CuNW based composites were investigated. Moreover, the electrical applications of the composites were demonstrated.

In this first part, ultra-light and highly porous CuNW monolith aerogels were fabricated and their mechanical and electrical properties were systematically investigated. The density of the monolith aerogels are below 10 $mg \cdot ml^{-1}$, which is less than 1‰ of the density of bulk copper. Moreover, since the shape, size, and density are controllable according to the amount of CuNWs in the aqueous solution before freeze-drying, we studied the relation between Young's modulus and density. The normalized Young's modulus obeys a scaling function, $E/E_s \sim (\rho/\rho_s)^3$. Furthermore, we also obtained a scaling function from normalized electrical conductivity, which follows $\sigma/\sigma_s \sim (\rho/\rho_s)^{0.81}$. Interestingly, the wetting properties of the CuNW monolith aerogels could be easily engineered through FAS modification, which demonstrated the application as selective adsorbents.

In the second part, a tiny amount of PVA was utilized to improve the mechanical properties of CuNW monolith aerogels. The CuNW-PVA composite aerogels exhibited elasticity, which could almost recover to its original height even after 60% compressive strain. Meanwhile, in comparison with the electrical conductivity of monolith aerogels, that of composite aerogels was hardly influenced by the addition of PVA. Therefore, benefited from the combined mechanical and electrical properties, we demonstrated their applications as pressure sensors. Moreover, we also developed CuNW-PVA composite aerogels as manufacturable electrical conductive rubbers by enbedding them into PDMS.

5.6 References

1. D Stauffer Stauffer, A. A., *Introduction To Percolation Theory, 2nd Edition*. Taylor & Francis: London, 1992.

2. Ma, X.; Peyton, A. J.; Zhao, Y. Y., Eddy current measurements of electrical conductivity and magnetic permeability of porous metals. *NDT & E International* **2006**, *39*, 562-568.

3. Kováčik, J.; Simančík, F., Aluminium foam—modulus of elasticity and electrical conductivity according to percolation theory. *Scripta Materialia* **1998**, *39*, 239-246.

4. Estevez, L.; Kelarakis, A.; Gong, Q.; Da'as, E. H.; Giannelis, E. P., Multifunctional Graphene/Platinum/Nafion Hybrids via Ice Templating. *J. Am. Chem. Soc.* **2011**, *133*, 6122-6125.

5. Lorna J. Gibson, M. F. A., *Cellular Solids: Structure and Properties*. Cambridge University Press: 1999.

6. Worsley, M. A.; Kucheyev, S. O.; Satcher, J. J. H.; Hamza, A. V.; Baumann, T. F., Mechanically robust and electrically conductive carbon nanotube foams. *Appl. Phys. Lett.* **2009**, *94*, 073115-3.

7. Schaedler, T. A.; Jacobsen, A. J.; Torrents, A.; Sorensen, A. E.; Lian, J.; Greer, J. R.; Valdevit, L.; Carter, W. B., Ultralight Metallic Microlattices. *Science* **2011**, *334*, 962-965.

8. Su, B.; Wang, S.; Song, Y.; Jiang, L., A heatable and evaporation-free miniature reactor upon superhydrophobic pedestals. *Soft Matter* **2012**, *8*, 631-635.

9. Yuan, J.; Liu, X.; Akbulut, O.; Hu, J.; Suib, S. L.; Kong, J.; Stellacci, F., Superwetting nanowire membranes for selective absorption. *Nat. Nanotechnol.* **2008**, *3*, 332-336.

10. Ge, J.; Yao, H.-B.; Wang, X.; Ye, Y.-D.; Wang, J.-L.; Wu, Z.-Y.; Liu, J.-W.; Fan, F.-J.; Gao, H.-L.; Zhang, C.-L.*, et al.*, Stretchable Conductors Based on Silver Nanowires: Improved Performance through a Binary Network Design. *Angew. Chem. Int. Ed.* **2013**, *125*, 1698-1703.

11. Xu, F.; Zhu, Y., Highly conductive and stretchable silver nanowire conductors. *Adv. Mater.* **2012**, *24*, 5117-5122.

12. Liang, H.-W.; Guan, Q.-F.; Chen, L.-F.; Zhu, Z.; Zhang, W.-J.; Yu, S.-H., Macroscopic-Scale Template Synthesis of Robust Carbonaceous Nanofiber Hydrogels and Aerogels and Their Applications. *Angew. Chem. Int. Ed.* **2012**, *51*, 5101-5105.

13. Rogers, J.; Someya, T.; Huang, Y., Materials and mechanics for stretchable electronics. *Science* **2010**, *327*, 1603-1607.

14. Sekitani, T.; Noguchi, Y.; Hata, K.; Fukushima, T.; Aida, T.; Someya, T., A Rubberlike Stretchable Active Matrix Using Elastic Conductors. *Science* **2008**, *321*, 1468-1472.

15. Rogers, J. A.; Bao, Z.; Baldwin, K.; Dodabalapur, A.; Crone, B.; Raju, V. R.; Kuck, V.; Katz, H.; Amundson, K.; Ewing, J.*, et al.*, Paper-like electronic displays: Large-area rubber-stamped plastic sheets of electronics and microencapsulated electrophoretic inks. *Proc. Natl. Acad. Sci. U.S.A.* **2001**, *98*, 4835-4840.

16. Gelinck, G. H.; Huitema, H. E. A.; van Veenendaal, E.; Cantatore, E.; Schrijnemakers, L.; van der Putten, J. B. P. H.; Geuns, T. C. T.; Beenhakkers, M.; Giesbers, J. B.; Huisman, B.-H.*, et al.*, Flexible active-matrix displays and shift registers based on solution-processed organic transistors. *Nature Mater.* **2004**, *3*, 106-110.

17. Bae, S.; Kim, H.; Lee, Y.; Xu, X.; Park, J.-S.; Zheng, Y.; Balakrishnan, J.; Lei, T.; Ri Kim, H.; Song, Y. I.*, et al.*, Roll-to-roll production of 30-inch graphene films for transparent electrodes. *Nat. Nanotechnol.* **2010**, *5*, 574-578.

18. Someya, T.; Kato, Y.; Sekitani, T.; Iba, S.; Noguchi, Y.; Murase, Y.; Kawaguchi, H.; Sakurai, T., Conformable, flexible, large-area networks of pressure and thermal

sensors with organic transistor active matrixes. *Proc. Natl. Acad. Sci. U.S.A.* **2005**, *102*, 12321-12325.

19. Wang, C.; Hwang, D.; Yu, Z.; Takei, K.; Park, J.; Chen, T.; Ma, B.; Javey, A., User-interactive electronic skin for instantaneous pressure visualization. *Nature Mater.* **2013**, *12*, 899-904.

20. Webb, R.; Bonifas, A.; Behnaz, A.; Zhang, Y.; Yu, K.; Cheng, H.; Shi, M.; Bian, Z.; Liu, Z.; Kim, Y.-S.*, et al.*, Ultrathin conformal devices for precise and continuous thermal characterization of human skin. *Nature Mater.* **2013**, *12*, 938-944.

21. Kim, D.-H.; Viventi, J.; Amsden, J. J.; Xiao, J.; Vigeland, L.; Kim, Y.-S.; Blanco, J. A.; Panilaitis, B.; Frechette, E. S.; Contreras, D.*, et al.*, Dissolvable films of silk fibroin for ultrathin conformal bio-integrated electronics. *Nature Mater.* **2010**, *9*, 511-517.

22. Chen, Z.; Ren, W.; Gao, L.; Liu, B.; Pei, S.; Cheng, H.-M., Three-dimensional flexible and conductive interconnected graphene networks grown by chemical vapour deposition. *Nature Mater.* **2011**, *10*, 424-428.

23. Qiu, L.; Liu, J. Z.; Chang, S. L. Y.; Wu, Y.; Li, D., Biomimetic superelastic graphene-based cellular monoliths. *Nat. Commun.* **2012**, *3*, 1241.

24. Garnier, F.; Yassar, A.; Hajlaoui, R.; Horowitz, G.; Deloffre, F.; Servet, B.; Ries, S.; Alnot, P., Molecular engineering of organic semiconductors: design of self-assembly properties in conjugated thiophene oligomers. *J. Am. Chem. Soc.* **1993**, *115*, 8716-8721.

25. Kim, D.-H.; Lu, N.; Ma, R.; Kim, Y.-S.; Kim, R.-H.; Wang, S.; Wu, J.; Won, S. M.; Tao, H.; Islam, A.*, et al.*, Epidermal Electronics. *Science* **2011**, *333*, 838-843.

26. Fan, Z.; Ho, J. C.; Jacobson, Z. A.; Yerushalmi, R.; Alley, R. L.; Razavi, H.; Javey, A., Wafer-Scale Assembly of Highly Ordered Semiconductor Nanowire Arrays by Contact Printing. *Nano Lett.* **2007**, *8*, 20-25.

27. Sun, Y.; Rogers, J. A., Inorganic Semiconductors for Flexible Electronics. *Adv. Mater.* **2007**, *19*, 1897-1916.

28. Kim, Y.; Zhu, J.; Yeom, B.; Di Prima, M.; Su, X.; Kim, J.-G.; Yoo, S. J.; Uher, C.; Kotov, N. A., Stretchable nanoparticle conductors with self-organized conductive pathways. *Nature* **2013**, *500*, 59-63.

29. Hu, L.; Kim, H. S.; Lee, J.-Y.; Peumans, P.; Cui, Y., Scalable Coating and Properties of Transparent, Flexible, Silver Nanowire Electrodes. *ACS Nano* **2010**, *4*, 2955-2963.

30. Chen, Y.; Ng, K. C.; Yan, W.; Tang, Y.; Cheng, W., Ultraflexible plasmonic nanocomposite aerogel. *R. Soc. Chem. Adv.* **2011**, *1*, 1265-1270.

31. Chen, Y.; Ouyang, Z.; Gu, M.; Cheng, W., Mechanically Strong, Optically Transparent, Giant Metal Superlattice Nanomembranes From Ultrathin Gold Nanowires. *Adv. Mater.* **2013**, *25*, 80-85.

32. Gong, S.; Schwalb, W.; Wang, Y.; Chen, Y.; Tang, Y.; Si, J.; Shirinzadeh, B.; Cheng, W., A wearable and highly sensitive pressure sensorwith ultrathin gold nanowires. *Nat. Commun.* **2014**, *4*. DOI: 10.1002/adma.201202241.

33. Yu, Y.; Zeng, J.; Chen, C.; Xie, Z.; Guo, R.; Liu, Z.; Zhou, X.; Yang, Y.; Zheng, Z., Three-Dimensional Compressible and Stretchable Conductive Composites. *Adv. Mater.* **2013**, DOI: 10.1002/adma.201303662.

34. Rathmell, A. R.; Wiley, B. J., The Synthesis and Coating of Long, Thin Copper Nanowires to Make Flexible, Transparent Conducting Films on Plastic Substrates. *Adv. Mater.* **2011**, *23*, 4798-4803.

35. Tang, Y.; Yeo, K. L.; Chen, Y.; Yap, L. W.; Xiong, W.; Cheng, W., Ultralow-density copper nanowire aerogel monoliths with tunable mechanical and electrical properties. *J. Mater. Chem. A* **2013**, *1*, 6723.

36. Kim, K.; Vural, M.; Islam, M., Single-walled carbon nanotube aerogel-based elastic conductors. *Adv. Mater.* **2011**, *23*, 2865-2869.

37. Yao, H.-B.; Huang, G.; Cui, C.-H.; Wang, X.-H.; Yu, S.-H., Macroscale Elastomeric Conductors Generated from Hydrothermally Synthesized Metal-Polymer Hybrid Nanocable Sponges. *Adv. Mater.* **2011**, *23*, 3643-3647.

38. Tappan, B. C.; Steiner, S. A.; Luther, E. P., Nanoporous Metal Foams. *Angew. Chem. Int. Ed.* **2010**, *49*, 4544-4565.

39. Chelidze, T.; Gueguen, Y., Pressure-induced percolation transitions in composites. *J. Phys. D: Appl. Phys.* **1998**, *31*, 2877.

Chapter Six

Conclusions and Outlook

1. Nanoparticle-Modified Electrode with Size- and Shape-Dependent Electrocatalytic Activities

We presented a robust chemical approach to tether CTAB-capped nanoparticles onto ITO electrode surfaces in order to systematically investigate particle size and shape effects on electrocatalytic performances in MOR and ORR under aggregation-free and desorption-free conditions. In particular, gold nanospheres with the diameters of 20 nm (AuNS20s) and 45 nm (AuNS45s), and gold nanorods (AuNRs) with narrow size distribution were successfully synthesized and immobilized onto ITO substrates. The order of the mass electrocatalytic activity towards MOR is AuNS20s > AuNS45s > AuNRs; whereas the order for ORR is AuNS20s > AuNRs > AuNS45s. These results clearly show that smaller sizes led to greater mass catalytic current densities if shapes or crystalline structures are the same; whereas shapes or crystalline structures determine catalytic selectivities towards specific electrocatalytic reactions; overall mass current density is a combined effects of size and shapes. Since a rich family of recipes were available for precisely controlling over fractions of crystalline facets on particle surfaces, our chemical modification strategy may serve as a general route to fabricate highly-stable, customizable electrocatalytic electrodes for a wide spectrum of applications in sensors and fuel cells.

2. Lightweight, Flexible, Nanoparticle Electrode with High Electrocatalytic Activity

We immobilized AuNP assembly on tissue paper via a simple drop-cast and dry method. With only a small loading amount of AuNPs, the paper slides were conductive enough as a light-weight and flexible electrode. Owing to the hierarchical porous fiber structures of paper substrate as well as the high surface-to-volume ratio of AuNPs, the flexible electrode exhibited an EASA which was 60 times larger than the geometric scanning area. Moreover, the electrodes showed excellent stability towards ORR and MOR; no obvious morphology variation was observed after hundreds cycles of potential scanning. We also confirmed the universality of the modification procedures by exploring commercially available sponge as substrate and AuNS45s as the conductive assemblies. Since substantial progress in wet chemistry synthesis have provided a rich family of recipes to precisely control over fractions of crystalline facets on particle surfaces, our chemical modification strategy potentially provides a rational route to fabricate highly-stable, economical, and customizable electrocatalytic electrodes for a wide spectrum of applications in sensors and fuel cells.

3. Ultralow-Density Copper Nanowire Aerogel Monoliths with Tunable Mechanical and Electrical Properties

Ultralow-density copper nanowire (CuNW) aerogel monoliths with well-defined shapes were successfully produced by the freeze-casting method. Unlike other metal aerogels which were usually made under harsh or special experimental conditions, the entire process for fabricating CuNW aerogel monoliths was under mild conditions without requirement of expensive equipment. In addition, the density of our CuNW aerogel

monolith could be adjusted over a fairly wide range and a density of as low as 4.6 mg cm^{-3} was achieved. Consequently, both conductivity and mechanical strengths could be systematically tuned: the normalized conductivity followed a scaling function, $\sigma/\sigma_s \sim (\rho/\rho_s)^{0.81}$; the normalized Young's modulus obeyed a scaling function, $E/E_s \sim (\rho/\rho_s)^3$. Furthermore, we showed the wetting properties of our CuNW aerogel monoliths could be easily engineered. FAS-modified aerogel monoliths were superhydrophobic, allowing for their uses as selective adsorbents in oil-spill cleanup. We believe that CuNW-based freeze-casting described here may be extended to other metal materials as well, which may serve be a general approach to fabricate low-density metal aerogel monoliths with tunable properties for a wide range of practical applications including sensors and supercapacitors.

4. Manufacturable Conducting Rubber Ambers and Stretchable Conductors from Copper Nanowire Aerogel Monoliths

We developed a cost-effective approach to fabricate CuNW-aerogel-based flexible conductor under mild conditions. The critical role of PVA was two-fold: stabilizing CuNW scaffolds and substantially enhancing the mechanical robustness and flexibility of the aerogels. The CuNW-PVA aerogels could be further embedded into PDMS without noticeable deformation. Importantly, resulting rubber ambers were conductive without the need of pre-wiring, and they could be manufactured into arbitrary complex 1D, 2D, 3D shapes simply by cutting. All the shaped rubber ambers remained conductive. The outstanding electrical properties and mechanical compliance of both CuNW-PVA aerogel and rubber ambers enabled the prototypes of piezo-resistive switches. We believe that our methodology represent a new low-cost approach to flexible conductors and switches with a broad spectrum of applications such as in flexible touch-on displays, human-machine interfacing devices and prosthetic skins.

5. Outlook

The thesis work indicates exciting future directions along the path. A vast majority of other building blocks in the "artificial periodic table" (Figure 1.3) and other new building blocks reported in the past two years or so may be used to design multifunctional metal electrodes for a wide spectrum of technical applications.

It is expected that nanoparticle-based ITO electrodes or paper electrodes will have potential uses in fuel cells. The thesis work demonstrated the possibility of tuning selectivity and activity simply by adjusting the sizes and shapes of gold nanoparticles. A vast majority of other building blocks from the "artificial periodic table" (Figure 1.3) and other new building blocks developed in the past two years may be used for designing such types of electrodes with any desired electrocatalytic properties for other important reactions. Further down the road, the porous paper electrodes from gold nanoparticles may be used in real fuel cell reactions due to their high permeability.

It is expected that CuNW-based electrodes will have more exciting applications such as (1) elastic switches, (2) wearable electronics, and (3) touch screens for portable devices. The embedding or encapsulation of CuNW aerogel by PVA and PDMS substantially improved their mechanical strength and prevented them from oxidation – a notorious problem in copper nanostructured electrodes. Despite these encouraging positive attributes, the downstream real-world applications remain requiring to address the long-term durability, sensitivity in various real-world environments, such in aqueous solutions or under high temperatures, etc. Once these challenges were overcome, real-world products from CuNWs may be seen in the near future.

Appendix

Publications and Presentations

Publications

1. **Tang, Y.**; Chen, Y.; Yap, L. W.; Cheng, W., Manufacturable Conducting Rubber Ambers and Stretchable Conductors from Copper Nanowire Aerogel Monoliths. Submitted to ***ACS Nano.***
2. **Tang, Y.**; Yeo, K. L.; Chen, Y.; Yap, L. W.; Xiong, W.; Cheng, W., Ultralow-density copper nanowire aerogel monoliths with tunable mechanical and electrical properties. ***J. Mater. Chem. A*** 2013, 1, 6723-6726.
3. **Tang, Y.**; Cheng, W., Nanoparticle-Modified Electrode with Size- and Shape-Dependent Electrocatalytic Activities. ***Langmuir*** 2013, 29, 3125-3132.
4. **Tang, Y.**; Ng, K. C.; Chen, Y.; Cheng, W., Lightweight, flexible, nanorod electrode with high electrocatalytic activity. ***Electrochem. Commun.*** 2013, 27, 120-123.
5. **Tang, Y.**; Cheng, W., Metallic Nanoparticles as Advanced Electrocatalysts. ***Sci. Adv. Mater.*** 2012, 4, 784-797.
6. Gong, S.; Schwalb, W.; Wang, Y.; Chen, Y.; **Tang, Y.**; Si, J.; Shirinzadeh, B.; Cheng, W., A wearable and highly sensitive pressure sensorwith ultrathin gold nanowires. ***Nat. Commun.*** 4, DOI: 10.1038/ncomms4132 (2014)
7. Xiong, W.; Sikdar, D.; Walsh, M.; Si, K. J.; **Tang, Y.**; Chen, Y.; Mazid, R.; Weyland, M.; Rukhlenko, I. D.; Etheridge, J.; Premaratne, M.; Lia, X.; Cheng, W., Single-crystal caged gold nanorods with tunable broadband plasmon resonances. ***Chem. Commun.*** 2013, 49, 9630-9632.

8. Su, B.; Wu, Y.; **Tang, Y.**; Chen, Y.; Cheng, W.; Jiang, L., Free-Standing 1D Assemblies of Plasmonic Nanoparticles. ***Adv. Mater.*** 2013, 25, 3968-3972.
9. Chen, Y.; Fu, J.; Ng, K. C.; **Tang, Y.**; Cheng, W. L., Free-Standing Polymer-Nanoparticle Superlattice Sheets Self-Assembled at the Air Liquid Interface. ***Cryst. Growth Des.*** 2011, 11, 4742-4746.
10. Chen, Y.; Ng, K. C.; Yan, W.; **Tang, Y.**; Cheng, W. L., Ultraflexible plasmonic nanocomposite aerogel. ***RSC Adv.*** 2011, 1, 1265-1270.
11. Ng, K. C.; Udagedara, I. B.; Rukhlenko, I. D.; Chen, Y.; **Tang, Y.**; Premaratne, M.; Cheng, W. L., Free-Standing Plasmonic-Nanorod Superlattice Sheets. ***ACS Nano*** 2011, 6, 925-934.

Presentations

Tang, Y.; Cheng, W., "Nanoparticle-based Electrode With Shape- and Size-dependent Electrocatalysis", (Oral presentation) The Fourteenth International Symposium on Electroanalytical Chemistry, Changchun, China, 17-20 Aug. 2013